MASTER THESIS

Ballbot-Inspired Orbital Refueling Depot and Fluid-Slosh Effects on Spacecraft Attitude Dynamics

Maher Kuzbari Mora

SUPERVISED BY

Sebastian Andreas Altmeyer

Universitat Politècnica de Catalunya
Master’s in Aerospace Science & Technology
June 2022

This Page Intentionally Left Blank

Ballbot-Inspired Orbital Refueling Depot and Fluid-Slosh Effects on Spacecraft Attitude Dynamics

BY

Maher Kuzbari Mora

DIPLOMA THESIS FOR DEGREE

Master’s in Aerospace Science and Technology

AT

Universitat Politècnica de Catalunya

SUPERVISED BY:

Sebastian Andreas Altmeyer

Escola d'Enginyeria de Telecomunicació i Aeroespacial de Castelldefels (EETAC)

This Page Intentionally Left Blank

ABSTRACT

Orbital refueling has become a subject of increasing interest as longer, deep space missions and manned missions to the Moon and Mars are being contemplated once again. For fueling depots to become part of the infrastructure in space capable of enhancing deployment and service operations, there remains a slew of technical, operational, and engineering challenges which must be overcome. In this thesis, focus is placed mainly on the issue of fluid slosh and its effects on the spacecraft dynamics and the design of an attitude control system.

In pursuit of overcoming the attitude tracking errors and instability from the fluid slosh, a novel satellite design is presented based on an omnidirectional ball-balanced robot (ball-bot) which aims at minimizing the control effort required to stabilize the satellite while also maximizing the amount of fuel it can carry. The satellite is comprised of two primary elements: a spherical tank, containing the fuel payload and a cuboid bus, containing the attitude control system (ACS) and other subsystems. The satellite bus is mobile and can displace itself over the surface of the sphere and has a sunshield which is deployed in orbit which shields the spherical tank from solar radiation. The cube is mobile and can displace itself on the surface of the sphere to point to the sun ensuring the protection of the fuel payload.

A presentation of the state-of-the-art of orbital fuel depots is first presented, and subsequently, a contextualization of orbital dynamics, along with the mathematical modeling of the satellite, is carried out, complemented by a discussion about the limitations of the work and the assumptions of the model. A simulation of the satellite's dynamics with the fluid slosh is conducted using Simulink and the sun-tracking of the cuboid-bus with Mathematica. Finally, a set of conclusions are presented and recommendations for future research and improvements, based on the conclusions, are made.

This Page Intentionally Left Blank

Table of Contents

This Page Intentionally Left Blank

Table of Figures

This Page Intentionally Left Blank

List of tables

Abbreviations & Symbols

Engineering Abbreviations	
ACS	Attitude Control System
GEO	Geostationary Orbit
LEO	Low Earth Orbit
LQR	Linear Quadratic Regulator
PID	Proportional Integral Differential controller
ECI	Earth-Centric Frame
LVLH	Local-vertical Local-Horizontal frame
Physics & Mathematical Abbreviations and Symbols	
t	Time
d	Incremental change
dt	Time-step
m	Mass
r	Radius
k	Spring constant
F	Force
g	Acceleration due to gravity

This Page Intentionally Left Blank

1. Introduction

1.1. Motivation

Broadly speaking, the success of the past thirty years of space exploration has been heavily reliant on the concept of on-orbit servicing and have demonstrated that it is not only feasible, but that it is key for the realization of the most ambitious missions, such as the Hubble Space Telescope and the International Space Station (ISS). If anything, mankind has placed a much greater ambitions on the next thirty years, considering the growing public enthusiasm as well as an increased investment due to the commercialization of space, owing to technological advancement which have made space infrastructure essential for providing valuable services and the reduction in cost of launching and deploying satellites into space. Continuous improvement beyond the launch-cost reduction and development on the ground imply fully exploiting the flight systems already launched and construction of space infrastructure in-situ promoting new scientific undertakings. Another reason to in-orbit servicing is fundamental to the next generation space infrastructure development is the need to act with regards to the unregulated proliferation of abandoned satellites which are posing an increased risk to the development of infrastructure in space.

As mentioned, it is expected that during the next decades, the most ambitious missions, particularly to the Moon and Mars, will take place. Deep-space missions and particularly manned missions are exceedingly complex and thus require higher payload masses to ensure the completion of mission objectives leading to larger, costlier, and more complex launch vehicles such as the Space X Starship or NASA’s Space Launch System (SLS), both designed for manned missions to the Moon and Mars. These massive launch systems demonstrate the exponential relationship between the payload mass and the launch vehicle size and performance which may not be sustainable. An approach to solving the problem of keeping launch payload mass high whist keeping launch vehicle mass reasonable, is to optimize the payload mass with respect to its constituents considering their participation as a fraction of the total. As the payload gets larger, fuel takes a larger and larger proportion of the payload mass, especially for deep space missions as well as manned missions. Hence the proposed solution to use an orbital fuel depot, if the payload could be launched with a smaller mass of fuel, it could be launched using less energy in to space.

1.2. Context

The project is presented in partial fulfillment of the graduation requisites for the master’s degree in aerospace science and technology (MAST) in the Polytechnical University of Catalunya. It was conceived, developed, and written by Maher Kuzbari, and supervised by Sebastian Andreas Altemeyer at l’Escola d'Enginyeria de

Telecomunicació i Aeroespacial de Castelldefels (EETAC) over the period of the spring semester of 2022.
The goal of the thesis project is to assess the consequences fluid slosh on the attitude dynamics of the satellite as well as present a novel design concept for the development of a satellite whose primary function is to act as a fuel depot.

1.3. Goals

The goal of this master thesis is two-fold: first to present a new concept of a fuel depot satellite and second, to analyze the consequences of fluid slosh on the attitude dynamics of the satellite. Enumerated, the goals set forth and realized in this project are (in no particular order):

1. Present the feasibility and importance of orbital refueling satellites.
2. Present a new concept for the design of an orbital refueling satellite inspired by a ballbot robot.
3. A brief study on the orbital and attitude dynamics of a satellite in LEO accompanied by a corresponding simulation.
4. A brief study on the fluid slosh dynamics in spacecraft accompanied by a simulation.
5. The design and implementation of an adequate controller to stabilize the spacecraft attitude in orbit without slosh as well as with slosh.
6. A simulation of sun tracking motion under slosh perturbations of the ballbot-inspired satellite.

1.4. State of the Art

Mid-1960s proposals for the Space Transportation System included propellant depots and nuclear "tugs" to transport payloads from LEO to other locations [1]. In October 2009, the Air Force and United Launch Alliance (ULA) conducted an experimental on-orbit demonstration on a modified Centaur upper stage during the DMSP-18 launch to better "understand propellant settling and slosh, pressure control, RL10 chill down, and RL10 two-phase shutdown operations." For the on-orbit demonstrations, the modest weight of DMSP-18 allowed for the use of 5,400 kilograms of residual liquid oxygen $\mathrm{LO_2}$ and liquid hydrogen $\mathrm{LH_2}$ fuel, or 28 percent of Centaur's capability. Prior to initiating the deorbit burn, the post-spacecraft mission extension lasted 2.4 hour [2].

NASA's Launch Services Program is collaborating with CRYOTE partners on continuing fluid dynamics experiments. After the removal of the primary payload from the Centaur upper stage in 2010, ULA is also planning additional in-space laboratory tests to further enhance cryogenic fluid management technologies using the Centaur upper stage. Known as CRYOTE, or Cryogenic Orbital Testbed, it will serve as a testbed for proving a variety of technologies required for cryogenic propellant depots, with numerous small-scale tests scheduled between 2012 and 2014. If funded, ULA estimates this mission might launch as early as 2012 as of August 2011. The ULA CRYOTE small-scale experiments are designed to pave the way for a 2015 ULA flagship cryo-sat technology demonstration [3].

The Future In-Space Operations (FISO) Working Group, a consortium of NASA, industry, and academic participants, met multiple times in 2010 to discuss propellant depot concepts and plans, including discussions of effective depot locations for human spaceflight beyond low Earth orbit, a suggested simpler (single vehicle) first-generation propellant depot, as well as six major propellant-depot-related technologies for refillable cislunar travel [4] [5].

In the "CRYOGENIC Propellant Storage and Transfer (CRYOSTAT) Mission," NASA intends to develop ways for enabling and upgrading space flights that utilize propellant depots. The CRYOSTAT spacecraft was anticipated to enter LEO in 2015 [5]. NASA proposed the "Simple Depot" mission in 2011 as a potential initial PTSD mission, with an Atlas V 551 that would launch no earlier than 2015. Simple Depot would employ the "used" (almost empty) Centaur upper stage LH2 tank for long-term storage of LO2, while LH2 would be stored in the Simple Depot LH2 module, which is launched with only gaseous Helium at room temperature [6].

At the AIAA Space 2010 conference in September 2010, ULA proposed propellant depots that might be used as waystations for other spacecraft to stop and refuel, either in low Earth orbit (LEO) for beyond-LEO missions or at Lagrangian point L for interplanetary journeys. The concept argues that waste gaseous hydrogen, an inevitable result of long-term storage of liquid hydrogen in the radiative heat environment of space, might be used as a monopropellant in a solar-thermal propulsion system. The waste hydrogen would be productively employed for orbital station-keeping and attitude control, as well as supplying limited propellant and thrust for orbital maneuvers to improve rendezvous with spacecraft on route to the depot to obtain fuel. ULA has suggested the Advanced Common Evolved Stage (ACES) upper stage rocket as part of the Depot-Based Space Transportation Architecture. ACES hardware is conceived from the beginning as an in-space propellant depot that may be utilized as waystations for other rockets to stop and refuel on their route to beyond-LEO or interplanetary missions, as well as to provide the high-energy technical capacity for the removal of space trash [7].

NASA made a substantial contractual commitment to the development of propellant depot technology in August 2011 by funding four aerospace companies to "define demonstration missions that would validate the concept of storing cryogenic propellants in space in order to reduce the need for large launch vehicles for deep-space exploration."

With Analytical Mechanics Associates, Boeing, Lockheed Martin, and Ball Aerospace, these contracts for the storage/transfer of cryogenic propellants and cryogenic depots were inked. Under the pact, each company will receive $600,000 each [8]. NASA chose the SpaceX Lunar Starship with in-orbit refueling as their initial lunar human landing system in April 2021. For Lunar Starship HLS, a bigger propellant-depot Starship was envisioned for 2022 [9].

China's space agency CNSA performed a demonstration satellite-to-satellite refueling operation in June 2016 [10].

2. Satellite Attitude Dynamics & Control

2.1. Introduction

The attitude of a spacecraft is its orientation in space with respect to a predefined absolute reference frame. Attitude dynamics consider how the orientation is determined, how it is controlled and how future motion is predicted. In this thesis, a brief technical overview of these topics is provided.

The motion of a rigid spacecraft is specified by its position, velocity, attitude, and attitude motion (rate). The first two quantities describe the translational motion of the center of mass of the spacecraft and are the subject of celestial mechanics, orbit determination and space navigation. The latter two quantities describe the rotational motion of the body of the spacecraft about the center of mass. Knowledge of the orbit is relevant to performing attitude determination and control operations, but they are independent functions. For example, a spacecraft in LEO will experience drag which is a function of the magnitude of the surface area that is orthogonal to the velocity vector. If the orientation of the spacecraft changes, unless it is perfectly symmetrical, the surface area will change and therefore the force of drag experienced by the spacecraft will be different, and this in turn will affect the spacecraft's velocity and therefore orbit. This coupling of the spacecraft's attitude dynamics and aerodynamic forces is typically ignored in favor and externally provided time-history of the spacecraft's altitude profile.

There are two types of attitudes, single-axis attitude, and three-axis attitude. Single axis is the specification of the orientation of the spacecraft around a single axis in inertial space. Ordinarily, this single axis is the spin axis of a spin-stabilized spacecraft. For a spin stabilized spacecraft, the orientation is not completely fixed in space since its rotation about the axis of rotation is still undetermined. The description of the attitude of a spin-stabilized spacecraft can be attained using only two parameters, α, the ascension and δ, the declination of the spin stabilized axis within the unit celestial sphere centered on the spacecraft.

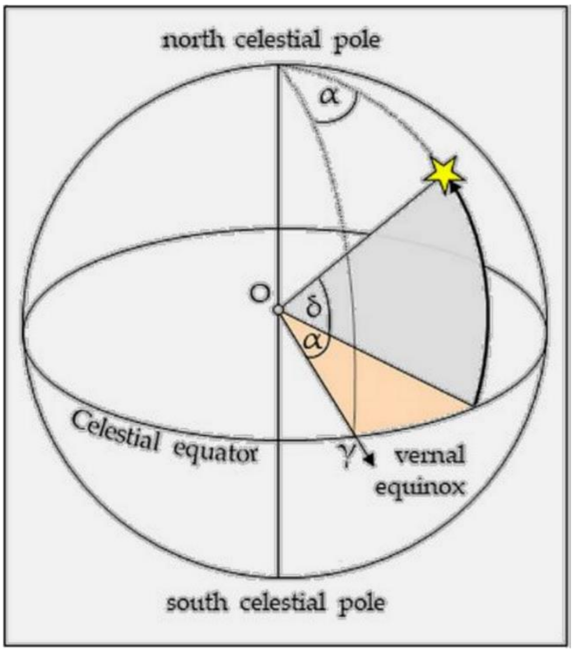

Figure 1 the celestial sphere (cs) with the ascension and declination angles for an observer on earth. The references for the ascension and declination for a cs centered on a satellite are different. [25]

Adding an additional independent component to the ascension and declination, the azimuth, allows for the complete determination of the spacecraft's dynamics about all three axes, which is the second attitude type called three-axis stabilization. Three-axis stabilization is more difficult to attain than single axis stabilization as it requires the tracking and measurement of three parameters instead of two.

Since the spacecraft now must determine three angles with respect to a fixed coordinate system, as opposed to two in for the single axis stabilized satellite, the fundamental equations for rotational dynamics introduced by Leonhard Euler can be applied to obtain the Euler angles. These angles define how the spacecraft-fixed coordinates are related to inertial coordinates.

$$\dot{\vec{\mathrm{H}}} = \vec{\mathrm{T}} - \vec{\omega} \times \vec{\mathrm{H}} \tag{1}$$

Equation (1) is in vector form and represents the conservation of angular momentum denoted by H. Angular momentum is, as is the case with linear momentum, a quantity that will remain constant unless an external force acts on it and changes it. In the case of linear momentum, the force is in Newtons, while in the case of angular momentum the force is a torque. On the other hand, while linear momentum is calculated as the mass times velocity, the angular momentum is calculated as the moment of inertia times the angular velocity. This is because the object cannot be considered a point mass when it is rotating, as different parts of the object will rotate at different velocities depending on their distance from the axis of rotation and therefore the distribution of mass of the object must be considered, hence the use of the moment of inertia, a 3-by-3 matrix of values that describes the distribution of mass along the principal axes.

$$\mathrm{I} = \begin{pmatrix} I_{xx} & 0 & 0 \\ 0 & I_{yy} & 0 \\ 0 & 0 & I_{zz} \end{pmatrix}$$

From the equation (1) it is apparent that the angular momentum's magnitude cannot be changed unless the torque T is applied, because a change in the term $\omega \times \mathrm{H}$ will only affect the direction of H. This is somewhat counter intuitive since it indicates that angular momentum is conserved within a rotating body even if it's different parts are rotating at different rates such as how a gyroscope spins within its housing, but conversely, one can consider that the housing is spinning around the gyroscope in both cases, if they are spinning in the absence of external torques, one must spin in the opposite direction from the other in order to conserve the angular momentum. Therefore, we can express H, the angular momentum now as:

$$\vec{\mathrm{H}} = \mathrm{I}\omega + \vec{\mathrm{h}} \quad (2)$$

Where h is the angular momentum stored by rotating objects that are part of the spacecraft, such as momentum wheels or gyroscopes. By applying the product rule to equation (1) and substituting from equation (2) we have:

$$\dot{\mathrm{I}}\omega + \mathrm{I}\dot{\omega} + \dot{\mathrm{h}} = \vec{\mathrm{T}} - \vec{\omega} \times \vec{\mathrm{H}} \quad (3)$$

Solving for the $\mathrm{I}\dot{\omega}$ term:

$$\mathrm{I}\dot{\vec{\omega}} = \vec{\mathrm{T}} - \dot{\vec{\mathrm{h}}} - \dot{\mathrm{I}}\vec{\omega} - \vec{\omega} \times \vec{\mathrm{H}} \quad (4)$$

The resulting equation (4) allows for the understanding of how the attitude of a spacecraft can change for a variety of causes.

- T represents the external torque's contribution to the attitude dynamics such as actuators and thrusters as well as any exogenous forces.
- $\dot{\mathrm{h}}$ this term represents the contribution of rotating objects inside the spacecraft since changes in their rotational velocity will lead to changes in the spacecraft's rotational velocity to preserve angular momentum.
- $\dot{\mathrm{I}}\omega$ here, the changing variable is the moment of inertia and therefore this term represents the contribution of the changing the spacecraft's distribution of mass on the attitude dynamics, such as the deployment of solar panels or the ejection of mass. If no such events or changes happen this term goes to zero.
- $\omega \times \mathrm{H}$ this term is referred to as the gyroscopic term and is an indicator of how the angular momentum changes direction but not magnitude in the spacecraft's frame of reference.

All these terms combine to give an angular acceleration as a result, indicating how much the rate of rotation will change. Keeping the spacecraft stable requires management of all the terms on the right-hand-side of the equation. The attitude response of the three-axis stabilized spacecraft can be largely uncoupled for small angular velocities by the following approximation:

$$\begin{aligned} I_{xx}\dot{\omega}_x &= T_x \\ I_{yy}\dot{\omega}_y &= T_y \\ I_{zz}\dot{\omega}_z &= T_z \end{aligned} \tag{4}$$

The equations for the spin-axis stabilized spacecraft are coupled, as shown:

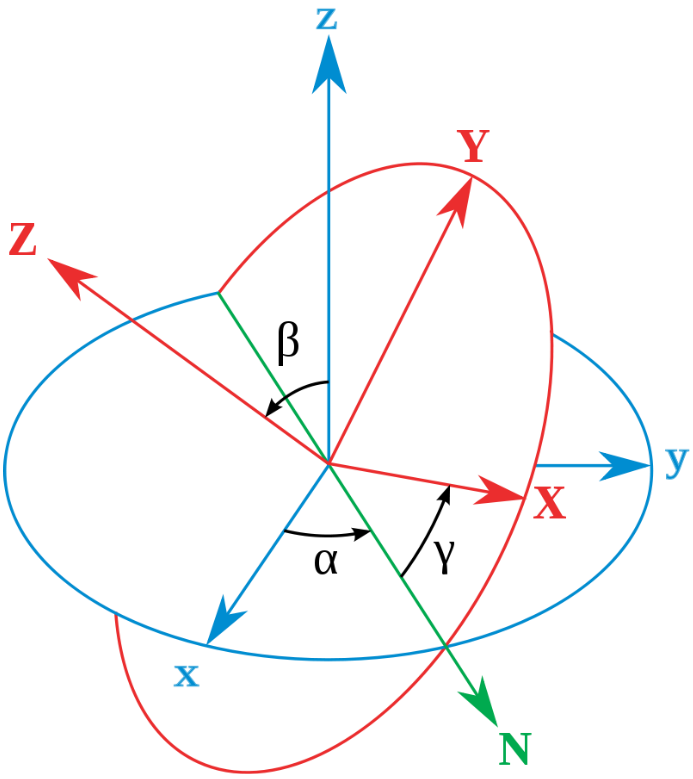

Figure 2 the Euler angles for a rigid body with respect to a fixed reference frame x,y,z. [26]

$$\begin{aligned} I_{xx}\dot{\omega}_x + S\omega_y(I_{zz} - I_{xx}) &= T_x \\ I_{xx}\dot{\omega}_y + S\omega_x(I_{zz} - I_{xx}) &= T_y \\ I_{zz}\dot{S} &= T_z \end{aligned} \tag{5}$$

Solving for ω_x and ω_y results in a system of two equations in which the torques are coupled:

$$\begin{aligned} I_{xx}(\ddot{\omega}_x + \omega_{\text{nut}}^2\omega_x) &= \dot{T}_x - \omega_{\text{nut}}T_y \\ I_{xx}\left(\ddot{\omega}_y + \omega_{\text{nut}}^2\omega_y\right) &= \dot{T}_y - \omega_{\text{nut}}T_x \end{aligned} \tag{6}$$

Where $\omega_{\text{nut}} = S[(I_{zz}/I_{zz}) - 1]$ is the nutation mode frequency. For the proper stabilization of the spacecraft, this mode must be damped.

In this thesis, the stabilization method used is the three-axis stabilization, this is down to two reasons, the first is that because the satellite to be controlled is a fuel depot which contains a large amount of fluid, spin-stabilization is not feasible, since only rigid objects can spin at a fixed rate whilst conserving angular momentum. The

fluid inside the satellite will affect the $\dot{I}\omega$ term, since the fluid will be displaced internal due to centripetal forces and the angular momentum will be dissipated causing the satellite's attitude to become unstable.
The second reason is that docking with another satellite will be more difficult if one of them is spin-stabilized, as they both must match each other's rates of rotation.

2.2. Attitude Control

The process of attitude control is the process which combines the prediction and reaction of the spacecraft to its rotational dynamics. Depending on the mission and design of the spacecraft, the disturbances it may be subject to would be small and highly predictable and therefore it may be passively controlled. This means that the spacecraft's design is such that the disturbances acting on it's rotational dynamics would stabilize it in an orientation that would meet the mission requirements. Often however, that is not possible, as the spacecraft may require to perform changes in its attitude, or the design does not allow for passive control. In this case, active control is used. Active control is a type of control that is reliant on actuators. A spacecraft may also have passive and active control systems simultaneously.

2.2.1. Attitude Response

If we consider the spacecraft the plant of feedback system, the attitude control system (ACS) would constitute the closed-loop system in which torques are the control signals which affect the attitude of the spacecraft, the output of the system.

Torques typically affect oscillatory modes in spacecraft, which in space environments, have very little damping. To successfully control the spacecraft's orientation, the ACS must avoid undue excitation of these modes as well as include a means of damping oscillatory modes. Damping can be attained via energy dissipation (passive control), or by actuation (active control). Since oscillatory modes are characterized by the exchange of potential and kinetic energy during each cycle, for a constant amount of energy exchanged, it would follow that the amplitude of oscillation is also constant that is proportional to the square root of the energy. The application of the control torque therefore must have an appropriate phase and amplitude. Considering the set of equations (4), the effect of each torque component will affect a principal axis, in a largely decoupled fashion for small angular rates. It is useful, as it will later be shown in this thesis, to record and consider the responses of the block to each torque component on each axis as the principal (basis) for the space of the block's possible responses.

A spacecraft's responses to torque can be classified into one of two categories: precessional and non-precessional. The non-processional response can be shown as:

$$I_{xx}\dot{\omega}_x = T_x \tag{7}$$

The rotational response is an angular acceleration around the principal axis for which the torque is applied, where $\dot{\omega}_x = \ddot{\phi}$. This is the case when momentum bias is not present, but also for the cases where momentum bias is present. If momentum bias is present, then it is only to the axis where the bias is present.

We can consider the non-precessional response to be analogous to the transient response, therefore, the precessional response is the steady state, or forced response. The simplified (without the nutational modes) equations for a planar model of a spacecraft's precessional response are:

$$\Omega_y = \dot{\theta} = T_x/H_z \tag{8}$$
$$\Omega_x = \dot{\phi} = -T_y/H_z$$

Where H_z is a momentum bias along the z-axis. The system of ordinary differential equations can be expressed as a state-space:

$$\frac{\mathrm{d}}{\mathrm{d}t}\begin{bmatrix}\Omega_x\\ \Omega_y\\ \phi\\ \theta\end{bmatrix} = \begin{bmatrix}0 & -H_z/I_{xx} & 0 & 0\\ H_z/I_{yy} & 0 & 0 & 0\\ 1 & 0 & 0 & 0\\ 0 & 1 & 0 & 0\end{bmatrix}\begin{bmatrix}\Omega_x\\ \Omega_y\\ \phi\\ \theta\end{bmatrix} + \begin{bmatrix}1/I_{xx} & 0\\ 0 & 1/I_{yy}\\ 0 & 0\\ 0 & 0\end{bmatrix}\begin{bmatrix}T_x\\ T_y\end{bmatrix} \tag{9}$$

2.2.2. Torques, Disturbance Torques and Torquers

It is important to distinguish between external torques, which affect the total angular momentum of the spacecraft, and internal torques which exchange momentum between different parts of the spacecraft. Actuators such as reaction wheels or control moment gyroscopes create internal torques, thus allowing for a change in the pointing of the spacecraft without changing the total angular momentum. Environment disturbances on the other hand are external torques which increase or decrease the total angular momentum and therefore these external torques must either be stored or removed by the attitude control system. Small disturbances which have a mean value of zero can be managed by storage, but secular torques, those which do not have a mean value of zero, such as the solar radiation pressure, will build up over time and must therefore be removed by the attitude control system by actuator that create external torques such magnetic torquers or solar trim tabs.

2.2.3. Disturbance Torques

The external torques to which a spacecraft is subject varies with the altitude at which it is situated. In the following table are some external torques and the altitudes at which they are typically encountered.

Table 1 External Disturbance Torques

External Torque Source	Altitude at which it is encountered
Aerodynamic drag	$< 500\ \mathrm{km}$
Magnetic	$500 - 35{,}000\ \mathrm{km}$
Gravity gradient	$500 - 35{,}000\ \mathrm{km}$
Solar radiation pressure	$< 700\ \mathrm{km}$
Thrust misalignment	All heights

Internal disturbance torques on the other hand, are not dependent on the altitude of the spacecraft but on its design and mission. The following is a list of some sources of internal torques:

- Motion of internal mechanical parts
- Liquid slosh, such as fuel
- Astronaut movement
- Flexible appendages such as solar panels or antennae
- Displacement of payload mass

2.2.4. Types of Torquers

The case can be made that while internal, storage-type torque solutions for attitude control are optional, it is *necessary* to have controllable external torquers. The following subsections various types of torquers are listed and discussed with their advantages and disadvantages.

2.2.4.1. Thrusters

Generally, thrusters are the largest source of force on a spacecraft, and therefore, potentially the largest source of torque. Since thrusters are external, they affect the total angular momentum of the spacecraft. In an ideal case the thruster vector passes through the center of mass, but in reality, there are always small deviations which cause disturbances.

In order to counter this disturbance, either the vehicle is spun in the intended direction and hence spin-stabilization is used or controlling the thrust direction by mounting the thrusters on gimbals is used. For launchers, the latter is used predominantly. In the case of orbit transfer maneuvers, spinning is more commonly used to average out thrust misalignment disturbance.

Low powered thrusters are commonly used for attitude control by providing a form of controllable external. This is achieved by mounting the thrusters pointing in different directions such that they are providing the three components of torque necessary to completely control the attitude of the spacecraft.

There are several advantages and disadvantages to thrusters, as opposed to their main rival the magnetic torquer, their torque magnitude is unaffected by the altitude, but it cannot be controlled once the thruster is installed, only the firing duration can be controlled.

Typically, ACS thrusters have a thrust level between $10^{-4}\mathrm{N}$ and $10^{-2}\mathrm{N}$. The fact that thrusters are powered by fuel is both an advantage and a disadvantage. It is an advantage in the sense that fuels are common and replaceable, but it is not necessarily possible to replace as some missions such as deep space missions are turn out to be typically restricted by fuel depletion as well as disadvantage of carrying the fuel mass itself and the slosh caused by its motion onboard the spacecraft.

2.2.4.2. Magnetic Torquers

Similar to how a compass needle aligns itself with the magnetic field of the earth, the magnetic field generated by the spacecraft interacts with the magnetic field of the earth thereby exerting an external couple.
We can represent the magnetic field of the spacecraft as a dipole with a magnetic moment m which reacts with a magnetic field with a local flux of B producing a torque T as expressed by the following equation:

$$\vec{\mathrm{T}} = \vec{\mathrm{m}} \times \vec{\mathrm{B}} \tag{10}$$

The torque T can be controllable using electromagnets via a current I. Replacing the magnetic moment in equation (10) with an electromagnet we obtain the following couple:

$$\mathrm{T} = n \cdot I \cdot A \left(\hat{c} \times \vec{B}\right) \tag{11}$$

Where n is the number of windings around the electromagnet core, A is the cross-sectional area of the magnet core, $\hat{c}$ is the unit vector along the coil winding axis. Typically, rod-like electromagnets in an orthogonal trio configuration. They can be used proportionally or discretely in an on-off manner for attitude control or momentum dumping.
Magnetic torquers have several advantages foremost of which is the fact that they do not require fuel to operate, their operation however decreases in effectiveness as the altitude of the satellite increases although they are used from LEO orbit all the way to GEO orbits.

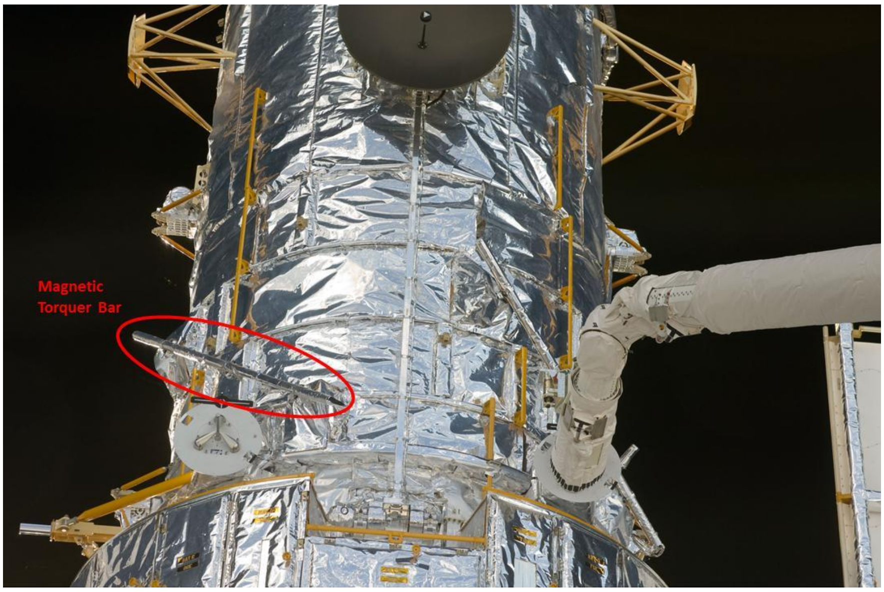

Figure 3 magnetic torquer on the Hubble Space Telescope [29]

2.2.4.3. Gravity Gradient

The equation dictating the change in the magnitude of the gravitational force on an increment of mass m is:

$$\mathrm{d}F = \frac{\mu\,\mathrm{d}m}{r^2} \tag{12}$$

Where:

- $\mu = 0.3986 \times 10^{15}\ \mathrm{m}^3/s^2$ is the gravitational constant of the Earth.
- r is the distance from the satellite's center of mass to the Earth's center of mass.

Using equation (12) the moments around the center-of-mass reveal the torque components to be:

$$\begin{aligned} T_x &= (3\mu/2r^3)\left(I_{zz} - I_{yy}\right)\sin 2\phi \cos^2\theta \\ T_y &= (3\mu/2r^3)(I_{zz} - I_{xx})\sin 2\theta \cos^2\phi \\ T_z &= (3\mu/2r^3)\left(I_{xx} - I_{yy}\right)\sin 2\theta \sin\phi \end{aligned} \tag{13}$$

Where θ and ϕ refer to the roll and pitch rotations respectively. The torques result in a disturbance torque that will cause the satellite to oscillate like a conical pendulum around its equilibrium state. In case the spacecraft's axis are very asymmetric or in the case of tethered satellites, this torque must be damped.
The frequency of oscillation "libration" is given by:

$$\omega_{\mathrm{lib}} = \sqrt{[(3\mu/2r^3)(1 - I_{zz}/I_{xx})]} \tag{14}$$

2.2.4.4. Aerodynamic Drag

The aerodynamic drag is the force caused by the collision of air particles with the surface of the satellite. The resulting torques around the center of mass can be computed by considering the area swept by the frontal cross-section in the direction of travel. Let a spacecraft's frontal area A constitute of small increments $\mathrm{d}A$, the resulting aerodynamic drag is given by:

$$\mathrm{dF_{aero}} = \frac{1}{2}\rho\, V_a^2 C_D\left(\hat{n}\cdot\hat{\mathrm{V}}_a\right)\left(-\hat{\mathrm{V}}_a\right)\mathrm{d}A \tag{15}$$

Where:

- ρ is the atmospheric density.
- V_a is the relative velocity of the spacecraft with respect to the air.
- C_D is the drag coefficient of the spacecraft.
- $\hat{n}$ is the unit normal vector of the incremental areas.

The resulting torque is the integral of the product of the aerodynamic force and the distance of the area increments:

$$\mathrm{T_{aero}} = \int \vec{\mathrm{r}} \times \mathrm{d}\vec{\mathrm{F}}_{\mathbf{aero}} \tag{16}$$

From equation (15) the term ρ is altitude dependent, since atmospheric density drops with respect to altitude, it is evident that the force, and therefore the resulting torque, are also dependent on the altitude of the spacecraft. The effects of the aerodynamic torques are negligible above $700\ \mathrm{km}$ for most satellite designs.

2.2.4.5. Solar Radiation Pressure

The photoelectric effect posits that light carries momentum. While small, if the moment arm around the center of mass is sufficiently large and the radiation large enough, the resulting torque will be significant. This change in angular momentum is caused by photons reflected off the surface exposed to the electromagnetic radiation, hence this type of radiation which in space is predominantly sourced from the sun is not to be confused by another source of disturbance torque also from the sun, which is the solar wind. Solar wind is a stream of charged, high velocity particles emanating from the sun which result from the nuclear reactions in its core.
The force exerted on a surface area exposed to sunlight is referred to as solar radiation pressure (SRP). Solar radiation pressure can be calculated as the vector difference between incoming and outgoing fluxes of photons.

As with the calculation of aerodynamic force, let $\hat{n}$ be the unit normal vector of an incremental area of a spacecraft exposed to sunlight, A, and the unit vector from the sun to the spacecraft be $\hat{s}$, the solar radiation pressure force is hence:

$$\mathrm{dF_{SRP}} = -\cos\theta\,\mathrm{d}A\left[(1-f_s)\,\hat{s} + \left(f_s\cos\theta + \frac{1}{3}f_d\right)\,\hat{n}\right] \tag{17}$$
$$\hat{s}\cdot\hat{n} \geq 0$$

Where:

- $P \sim 4.67 \times 10^{-6}\mathrm{Nm^{-2}}$ is the mean momentum flux at the Earth.
- f_s, f_d are the coefficients of specular and diffuse reflection, respectively.

Most satellites are designed such that SRP and aerodynamic torques cancel each other out, however, SRP can be used to counteract momentum buildup.

2.2.4.6. Momentum Storage Torquers

In contrast with the other torque sources discussed in the preceding sections, momentum storage torquers are internal torquers as opposed to external torquers such as thrusters. Momentum storage torquers take the form of reaction wheels (RW) or momentum wheels (MW). These devices are precision-built wheels that rotate about a fixed axis and have a built-in torque motor. The use cases and range of characteristics vary considerably depending on the satellite and mission. Early use for reaction wheels was restricted to larger satellites with a mass of one or more tons. A typical reaction wheel with a diameter of ~ 20 to $\sim 40\ \mathrm{cm}$ with a mass of ~ 3 to $10\ \mathrm{kg}$ has a momentum storage capacity of ~ 5 to $70\ \mathrm{kg\ m^2/s}$. More recent use of momentum wheels has found its way into much smaller satellites of $50\ \mathrm{kg}$ or less which has been facilitated by the downsizing of electronics and advances in material technology.

The difference between momentum wheels and reaction wheels are in their operation state. Reaction wheels have an angular rate of zero unless the ACS calls for a control torque. Momentum wheels' functions are to provide a momentum bias and are therefore always spinning at a constant rate with respect to a principal axis typically between 5000 rpm and $10{,}000 \text{ rpm}$.

Figure 4 momentum / reaction wheel with its protective cover removed [28]

Table 2 Summary of Torquers

Type	**Advantages**	**Disadvantages**
	External	
Thrusters	- Not dependent on altitude - Adequate for any orbit - Torque can be applied to all axes	Fuel is required Magnitude of torque is not controllable
Magnetic	- Does not require fuel - Magnitude of torque is controllable	Cannot torque about the local field direction
Gravity Gradient	Conservative force, no energy is required.	- No torque about the vertical axis - Oscillatory modes may require damping
Solar Radiation Pressure	No fuel requirements	- Torque magnitude is very small - No torque during eclipse

Internal		
Reaction and momentum wheels	- Require no fuel - Capable of storing momentum - Controllable torque magnitude - High precision, continuous adjustment and pointing - Can create momentum bias	Friction forces are nonlinear when wheels are stationary.
Control moment gyroscope (CMG)	- Suitable for three-axis control - Can create momentum bias	- Highly complex - Reliability issues

2.3. Attitude Determination

Providing a unique solution for the attitude state as a function of time is a process which involves combining sensor inputs with the knowledge of the spacecraft dynamics [11]. This solution can be obtained either after post-processing on the ground or onboard for immediate use. The increased power and downsizing of microprocessors have made onboard processing the more ubiquitous method for performing attitude determination-related calculations.

There are many ways to describe the attitude of a spacecraft, such as the Euler angles discussed in chapter 1, direction cosines and quaternions to be discussed in a following section. The essence of the problem lies in defining a reference frame, usually the right-handed set of axes, a datum set can then be defined as the departure from the reference frame. Euler angle notation used for aircraft has been used in practice for spacecraft as well, where ψ is the roll angle, θ the pitch, ϕ the roll which describe rotations around the z, y and x-axes, respectively. For spacecraft, the z-axis is typically, as is the case for aircraft, the axis along the vertical and the x-axis the axis along the direction of travel which in the case of an orbit would always be tangent to the orbital path. It is important to note that there is no universal standard for setting the reference coordinates as they are dependent on the satellite design and its mission. Another important note, when using Euler angles is that the coordinate system contains a singularity when $\theta = 90°$, this means that the there is no unique solution for attitude determination calculation and therefore the yaw and pitch angles cannot be specified by the ACS. This can happen during launch as the spacecraft is situated vertically and can be overcome by changing the coordinate system references as was the case with the space shuttle.

It is also important to keep in mind that the quantities describing the attitude (ψ, θ, ϕ) are not vector quantities, but their derivatives, $(\dot{\psi}, \dot{\theta}, \dot{\phi})$ are vector quantities whose rotational rates have directions along the orthogonal axes. The rates along the axes can be resolved from the following equations:

$$\omega_x = \dot{\phi} - \dot{\psi}\sin\theta \tag{18}$$
$$\omega_y = \dot{\theta}\cos\phi + \dot{\psi}\cos\theta\sin\phi$$
$$\omega_z = \dot{\psi}\cos\theta\cos\phi - \dot{\theta}\sin\phi$$

Inverting the equations such that we obtain expressions for $(\dot{\psi}, \dot{\theta}, \dot{\phi})$ we obtain:

$$\dot{\psi} = (\omega_y \sin\phi + \omega_z \cos\phi)/\cos\theta \tag{19}$$
$$\dot{\theta} = \omega_y \cos\phi - \omega_z \sin\phi$$
$$\dot{\phi} = \omega_x + (\omega_y \sin\phi + \omega_z \cos\phi)\tan\theta$$

2.3.1. Frequently Used Frames

Following from the previous discussion where a generalized notion of orientation was introduced for objects in orbit, this section will go over, briefly, on some of the most frequently used frames of reference for the design and deployment of space systems which coincide with the ones used in the thesis project.

2.3.1.1. Body Fixed Frame

In this coordinate system the origin is located at the body center-of-mass. It is carried by the body and directly defined on it.
The axes are defined on the principal axes of rotation of the rigid body constituting the system. Let $\mathcal{J}$ be the moment of inertia matrix which is 3×3 and symmetrical. $\mathcal{J}$ will have three mutually orthogonal eigenvectors associated with its eigenvalues. For the index $i = 1,2,3$ we obtain the compact expression:

$$\mathcal{J}\mathrm{x}_i = \lambda_i \mathrm{x}_i \tag{20}$$

Where:

- x_1 defines the axis X_b (b for *body*), points in the direction of the spacecraft velocity.
- x_2 defines the axis Z_b, points to the orbital plane.

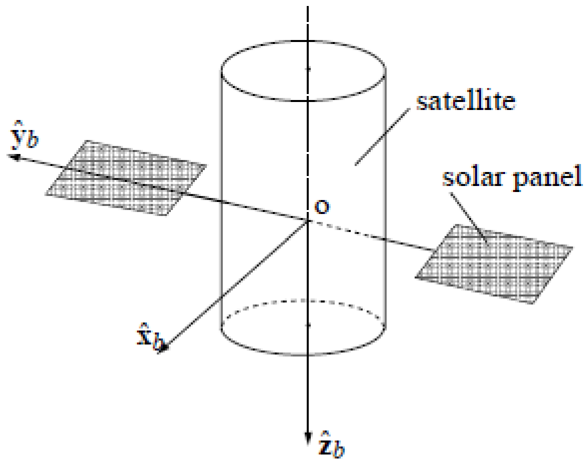

Figure 5 Body Frame of Reference [27]

- x_3 defines the axis Y_b, complies with the right-hand rule.

2.3.1.2. Earth Centered Inertial Frame (ECI)

There are two main reasons for using the Earth centered frame, the first is because the classical laws of motion and gravity, defined by Newton, apply to the spacecraft in this frame and the second reason is that since this frame is defined in terms of the earth's axis of rotation and the orbital plane (the ecliptic plane) which is convenient for inertial pointing satellites. The ecliptic plane and the equatorial plane are perpendicular to the rotation axis, but because of the precession of the rotation axis the vernal equinox (March 21) was defined as an ECI frame reference point. The axes are as follows:

- X_I is in the direction from the Earth center to the vernal equinox.
- Z_I is the Earth rotational axis.
- Y_I follows the right-hand rule.

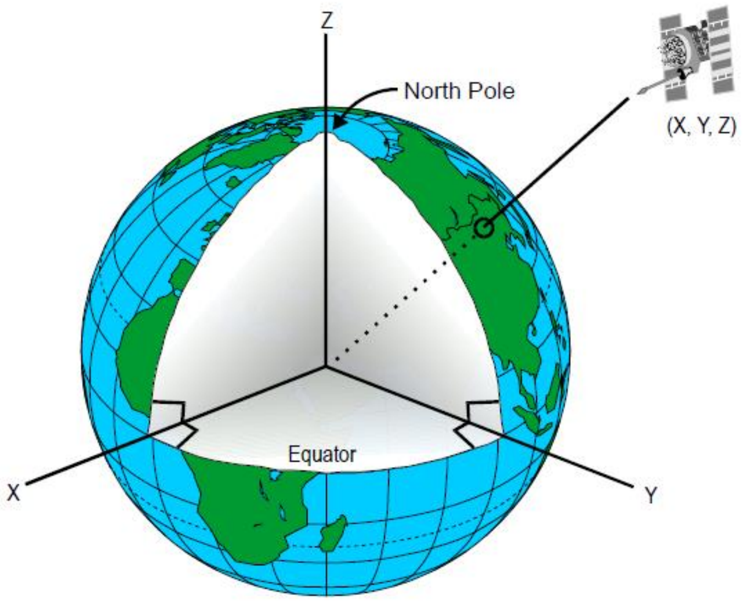

Figure 6 ECI Frame of Reference [12]

2.3.1.3. Local Vertical Local Horizontal Frame (LVLH)

Arguably the most practical frame of frame of reference due to the sheer number of satellites that are designed to be nadir-pointing. The origin in this frame of reference is the center-of-mass of the satellite. There axes are defined as follows:

- X_{lvlh} is along the direction of the spacecraft's velocity vector.
- Z_{lvlh} is perpendicular to X_{lvlh} and always pointing at the earth's center.
- Y_{lvlh} is perpendicular to the orbit plane and follows the right-hand rule.

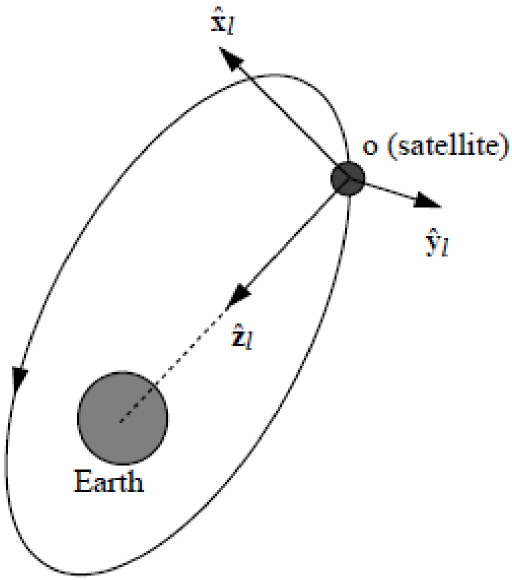

Figure 7 LVLH Frame of Reference [27]

2.3.2. Measuring Attitude

Providing an attitude *estimate* or attitude *solution* can be regarded as the goal of the attitude determination process. As previously discussed, it is imperative that *three* pieces of information are provided to the attitude control system which relate the spacecraft axes to the datum set and this is the case regardless of the form that the information takes, be that Euler angles or other forms. Therefore, the attitude control system must contain sufficient sensors to extract that information with a reasonable accuracy and simplicity during all phases of the mission via sensors that track the orientation of the spacecraft with respect to specific celestial references. In orbit around the Earth, the earth itself, the Sun as well as some stars are taken as references, and each is tracked using a specific sensor. The Sun is tracked with a sun-tracker, the stars with a star-tracker. It is common for a spacecraft to use a multitude of sensors as noise from one sensor or other drawbacks may hinder the attitude determination and result in a faulty attitude estimate or solution.

Note that because most, if not all sensors use the spacecraft's own frame of reference as a basis for attitude determination and control, the angular moment must be measured in the same frame of reference, hence the spacecraft-referenced nature of the Euler equations.

The sensors of an attitude measurements system can by placed into two distinct categories that complement each other. The first is the *reference sensor*, which measures the direction of a reference object such as the sun in the case of a sun sensor or a star in the case of a star sensor. In the second category are the *inertial sensors*, these sensors are continuously measuring the attitude such that they only measure changes in the attitude of the spacecraft. Usually consisting of gyroscopes, they require calibration as drift will cause their mechanisms to produce larger errors over time. Since many sensors are used for the same task, combining the measurements obtained from them is a complex field of study also known as *sensor fusion*. There are many methods for sensor fusion ranging from a simple logical combination of the sensor hardware to advanced information filtering methods such as Kalman filtering.

2.3.2.1. Sun Sensors

The intensity of the sun's radiation provides an unambiguous, well-defined vector which subtends 30 arc minutes at the Earth's position. Because of this, there are several types of sensors from merely presence detection which communicate whether the sun is in the satellite's field of vision (FOV), to position detection with a degree of accuracy with slit-type sensors.

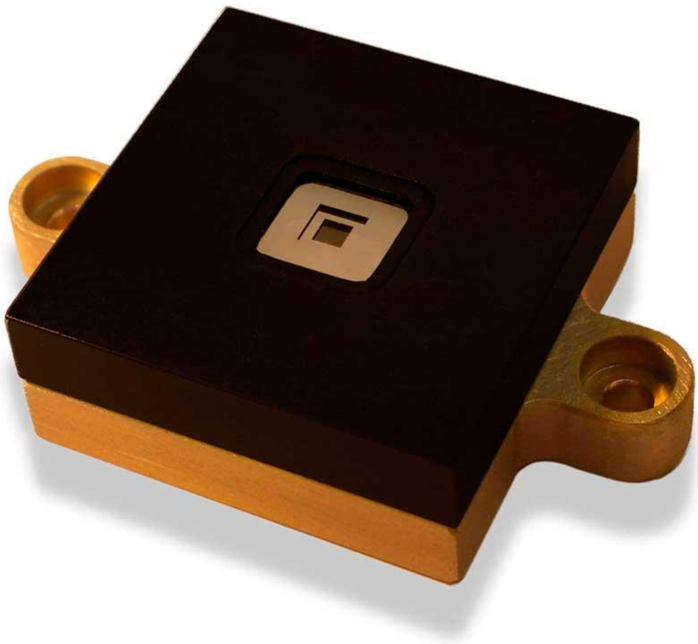

Figure 8 Sun Sensor for Small Satellites [32]

2.3.2.2. Earth Sensors

From the perspective of a spacecraft, the apparent radius of the Earth R_e subtends an angle of:

$$\alpha = 2\sin^{-1}[R_e/(R_e + h)] \quad (20)$$

Solving for a spacecraft at a height of $500\,\mathrm{km}$ we have that the angle $\alpha = 135°$ which means that the Earth is almost always in the spacecraft's field of vision. This is reduced to around $17.5°$ for a spacecraft at GEO. Therefore, it is evident that the uses for LEO orbiting satellites and GEO orbiting satellites must be completely different. The *nadir vector* is a vector that points toward the Earth's center from the satellite. It is computed by bisecting the diameter of the earth's apparent disk. *Nadir-pointing* satellites make use of earth sensing satellites to perform this calculation. In order to avoid large variations in radiance as well as the terminator line the $15\,\mu\mathrm{m}\ \mathrm{CO_2}$ absorption band is used.

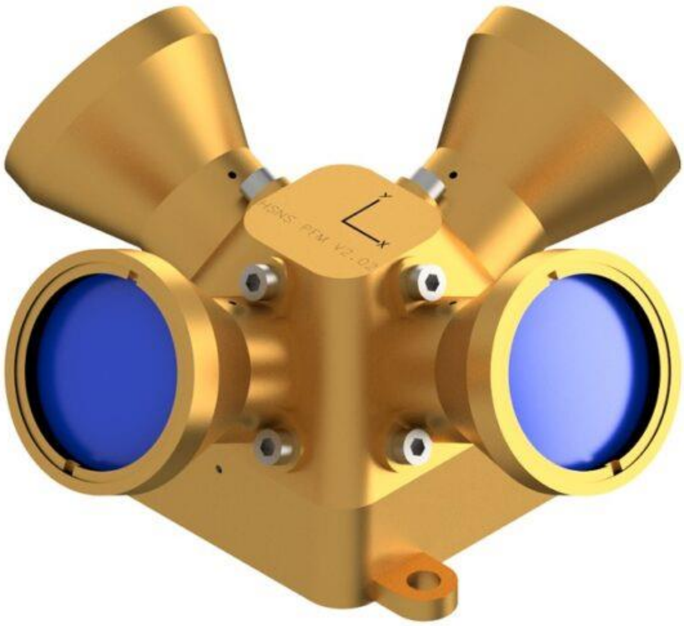

Figure 9 Earth Sensor With 4 IR Camaras [32]

2.3.2.3. Star Sensors

By far the most accurate and reliable sensors for measuring attitude in use today are star sensors. Advances CCD and solid-state technology has made star sensors smaller and more affordable as well as more efficient thus expanding their use into smaller satellites.

Star scanners are mounted on spinning spacecraft, and work by scanning the stars passing through the satellite's FOV, Star trackers and mappers are mounted on three-axis stabilized spacecraft. Trackers track one stellar image in their FOV and therefore more than one may be needed in order to obtain sufficient information about the spacecraft's attitude. Mappers have a large field of vision and can track several stars allowing for more information to be gathered about the spacecraft's orientation in a given axis. Many star trackers now employ image processing technology which allows for the determination of spacecraft's angular velocity, making way for "gyro-less" spacecraft, saving weight and energy due to carrying less instruments.

Figure 10 Star Sensor for Satellites [13]

2.3.2.4. Radio Frequency Beacons

Radio frequency sensors onboard the spacecraft, particularly spin-stabilized spacecraft extract information from a regularly pulsed radio signal from a beacon. The spacecraft's motion around it's axes will modulate the frequency and phase thereby providing the spacecraft with information about its attitude.

2.3.2.5. Magnetometers

Magnetometers measure the strength of the local magnetic field in order to obtain information about the spacecraft's attitude. Their accuracy is limited to about $0.5°$ and are therefore somewhat unreliable compared to the other methods described. A main disadvantage is that the magnetic field of the Earth is highly irregular when at high degree of resolution required for attitude control as well as full of anomalies that must be taken into account such as the south-Atlantic anomaly. It is common practice to include a reference model of the Earth's magnetic field internally for the sensor.

Figure 11 Small Satellite Magnetometer [14]

2.3.2.6. Inertial Sensors

Also known as gyroscopes, until recently have comprised of complex mechanical instruments which measure the torque and angular rate (ω) about a sensitive axis, therefore, three orthogonal gyros will provide all the full information required about the satellite's angular rates $(\omega_x, \omega_y, \omega_z)$. Rate integrating gyros output the integral of the velocity component $\int \omega \, \mathrm{d}t$.

An accuracy of $0.001°/\mathrm{h}$ can be expected from a high-quality sensor. Even higher accuracies can be obtained from ring-laser type gyroscopes (RLG). These gyroscopes do away with mechanical parts in favor of small rectangular prism through which two laser lights are reflected around its vertices, on return to the source a diffraction pattern is form. If the RLG is rotating around the sensitive axis, one of the paths is shorter and therefore the diffraction pattern is different. The fiber optic gyroscope provides similar if not higher degrees of accuracy whilst being more compact than an RLG. The FOG does away with the prism in favor of coils of fiber optic cable wound around the sensitive axis. Through this cable two distinct laser beams are fired simultaneously if the spacecraft spins around the sensitive axis, there will be a phase shift in the laser beams within the sensor.

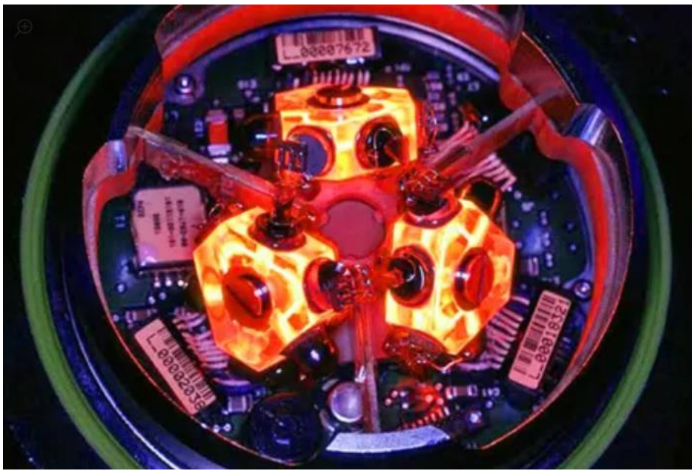

Figure 12 Ring Laser Gyroscope for Aircraft [15]

Table 3 Accuracy of different sensor types

Reference	Accuracy of Sensor
Stars	1 arc second
Sun	1 arc minute
Earth horizon	6 arc minutes
Radio Frequency (RF) Beacon	1 arc minute
Magnetometer	30 arc minutes
Global Positioning System (GPS)	6 arc minutes

2.4. Attitude Control System Computation

The increased autonomy and sophistication of the control techniques, many of which their applications where confined to ground based systems exclusively, is owed to recent advances in semiconductor technology have allowed for an increased amount of downsizing and efficiency gains of onboard computers (OBCs) which because of the stringent power and reliability requirements along with the high radiation environment of space have made space rated electronics vastly different from other types of electronics in terms of capacity, speed and efficiency.

A key requirement for ACS technique used is robustness, this is because the conditions in space are difficult to simulate on Earth and spacecraft are subject to unexpected conditions during their operation lifetime which are difficult to foresee. For example, spacecraft with large flexible appendages such as radiators or solar panels will have natural frequencies which are difficult to establish before launch. Therefore, it is common practice for the control system architecture to be reprogrammable, either from Earth or to use an adaptive control technique such as a model predictive controller (MPC). Uploading control software is routinely conducted to enhance performance, adapt to a failure, or change in mission requirements.

2.4.1. PID Active Control

In this thesis, the control technique for stabilizing the satellite used is the *proportional, integral, and differential* (PID) technique. This simple technique employs a feedback architecture that takes attitude sensor measurement data and comparing it to a reference set which results in an *error signal*. The error signal is used by the OBC to compute the adequate response to the satellite's current attitude. Typically, the Euler angles ϕ, θ, ψ are used as measures of error along with direction cosines and quaternions.

Once the error signal for attitude is sufficiently large the OBC will deem it necessary to compensate by applying a torque on one or several of the principal axes of rotation. The torque acting on the spacecraft may cause an acceleration or if momentum bias is used an angular velocity. In this case, the satellite contains no momentum bias and therefore this case will not be considered in this discussion.
The applied torque will cause an angular acceleration of the spacecraft toward its reference attitude minimizing the error signal. The behavior of the error signal will obey the following differential equation's form:

$$\ddot{\epsilon} + 2\zeta\omega_n\dot{\epsilon} + \omega_n^2\epsilon = 0 \tag{21}$$

Here the speed of the speed of the response is governed by the natural frequency ω_n to an input and the damping ζ reveals how quickly to oscillations in the response will fade out.

2.4.1.1. Implementation Case for Roll Error

For an axis symmetrical spacecraft, the equations for controlling the attitude of the three principal axes are identical, therefore let's consider the roll angle ϕ to have a disturbance such that:

$$\begin{gathered} T_x = T_{xd} + T_{xc} \\ \therefore I_{xx}\ddot{\phi} = T_{xd} + T_{xc} \end{gathered} \tag{22}$$

Where T_{xd} is the disturbance torque and T_{xc} is the control torque. The control torque is determined using the difference between the reference angle and the actual roll angle, this reading can be obtained from a start tracker or Sun tracker and the rate of change of the roll angle which is obtained from a gyro. The expression for the control torque as described is now:

$$T_{xc} = -K_{xp}\phi - K_{xd}\dot{\phi} \tag{23}$$

Replacing T_{xc} in equation (22) with the right-hand-side in equation (23) and solving for T_{xd} we obtain the following expression:

$$\ddot{\phi} + (K_{xd}/I_{xx})\dot{\phi} + \left(K_{xp}/I_{xx}\right)\phi = T_{xd}/I_{xx} \tag{24}$$

The expression has a non-zero right-hand-side, the response to an initial error will have an error of T_{xd}/I_{xx} called the *steady-state error.* Including an integral term in the equation will reduce this error to zero. The torque expression with the integral term:

$$T_{xc} = -K_{xp}\phi - K_{xd}\dot{\phi} - K_{xi}\int \phi \, \mathrm{d}t \tag{25}$$

Evidently, the successful implementation of a PID controller is dependent on determining the parameters K_{xp}, K_{xd} and K_{xi} that result in a satisfactory performance of the closed-loop system, the system with output feedback in a process called *tuning*. There are many methods for tuning a PID controller, such as Cohen-Coon and Ziegler-Nichols, however due to the complexity of satellite structures and their operating environment, trial and error is the most common method used.

For an ACS reliant on PID to work several practical issues need to be addressed. The first is actuator saturation. Aside from the requirement of controllability, there actuator such as a torque wheel or magnetic torquer have a predetermined capacity if the OBC calls for higher torques than the torquers can provide then the ACS might fail to control the spacecraft. Another consideration is that no spacecraft is perfectly rigid, especially if large appendages are attached or if a significant amount of fuel is contained within the structure. This will lead to sensor noise which that model the excitation modes of the spacecraft structure. For large spacecraft there will be several excitation modes and, as discussed previously, these modes cannot be reliably experimentally calculated prior to launch, hence necessitating on-orbit calibration of the control algorithm parameters so that these modes do not lead to destabilizing the spacecraft. Finally, during large repointing maneuvers, cross-coupling between the roll, pitch and yaw motions becomes significant and detrimental. To avoid this, the maneuvers are carried out in sequence along each axis separately.

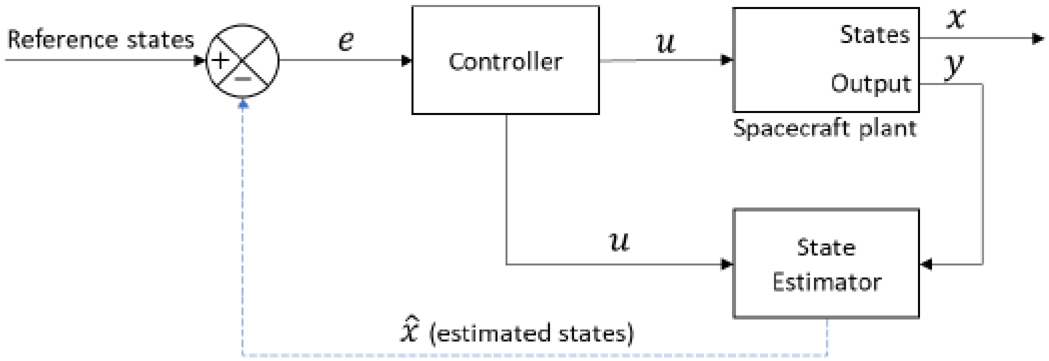

Figure 13 A generic control system architecture [16]

2.4.1.2. Notch Filtering

It is not uncommon for a closed-loop system to have unstable dynamics due to the excitation of certain modes at certain frequencies. This is caused by one or more pairs of complex-conjugate poles which are situated in close proximity to the imaginary axis in the *s-plane.* A solution for controlling the system is to implement a controller that has zeros near the lightly damped poles of the plant such that they attenuate their oscillatory effects on the output response. This type of controller is what is known as a notch filter, its design takes into account the frequencies at which certain modes become unstable.

2.4.1.3. Notch Filtering Example

Here, a marginally stable transfer function is taken, and a notch filter is implemented using Mathematica software. Let $G(s)$ be the transfer function:

$$G(s) = \frac{1}{(s+3)(s^2+s+10)}$$

It's pole zero plot is reveals there are two lightly damped poles:

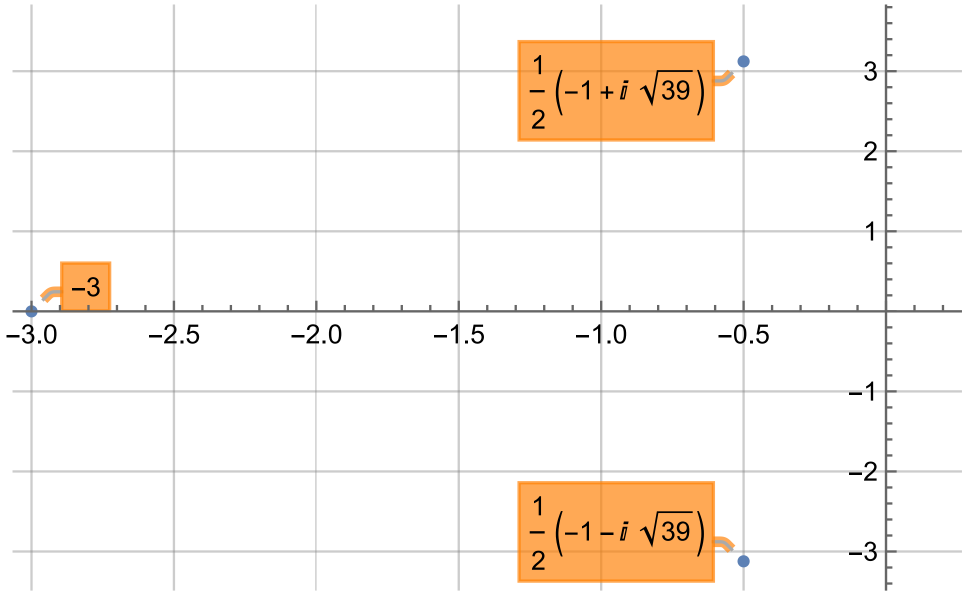

Figure 14 The pole zero plot of G(s)

The unit step response is highly oscillatory and has a large overshoot:

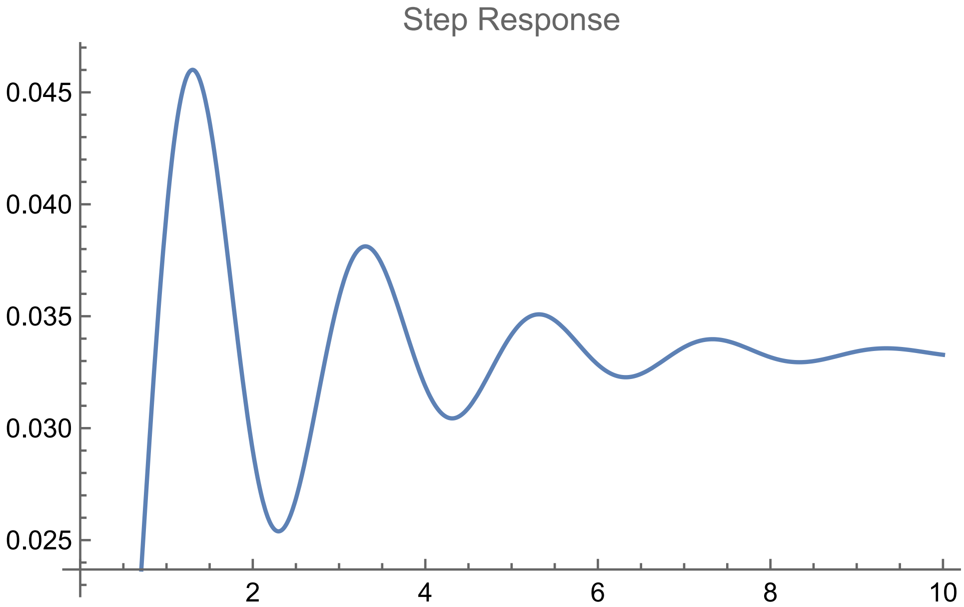

Figure 15 The unit-step response of G(s)

This indicates that for higher gains, $G(s)$ would be totally unstable, meaning that with only a proportional controller, the oscillations cannot be damped.

The frequency response peaks at a relatively low frequency:

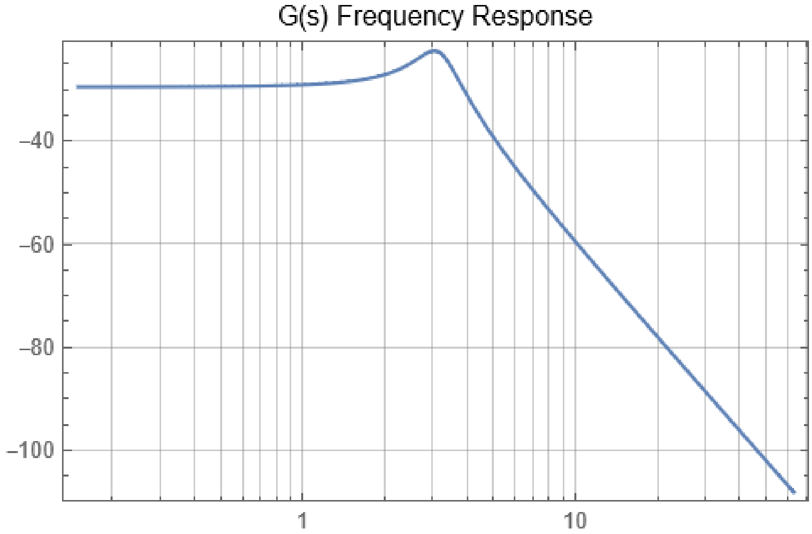

Figure 16 The gain Bode plot for G(s)

Let $C(s)$ be a notch filter controller with zeros slightly to the left of $G(s)$'s poles:

$$C(s) = \frac{s^2 + 1.5s + 10}{s^2 + 20s + 100}$$

The resulting transfer function for the compensated system is $C(s) * G(s)$:

$$\frac{s^2 + 1.5 + 10}{(s^2 + 20s + 100)(s^2 + s + 10)(s + 3)}$$

We can assess the compensated system's stability by looking at its root locus plot:

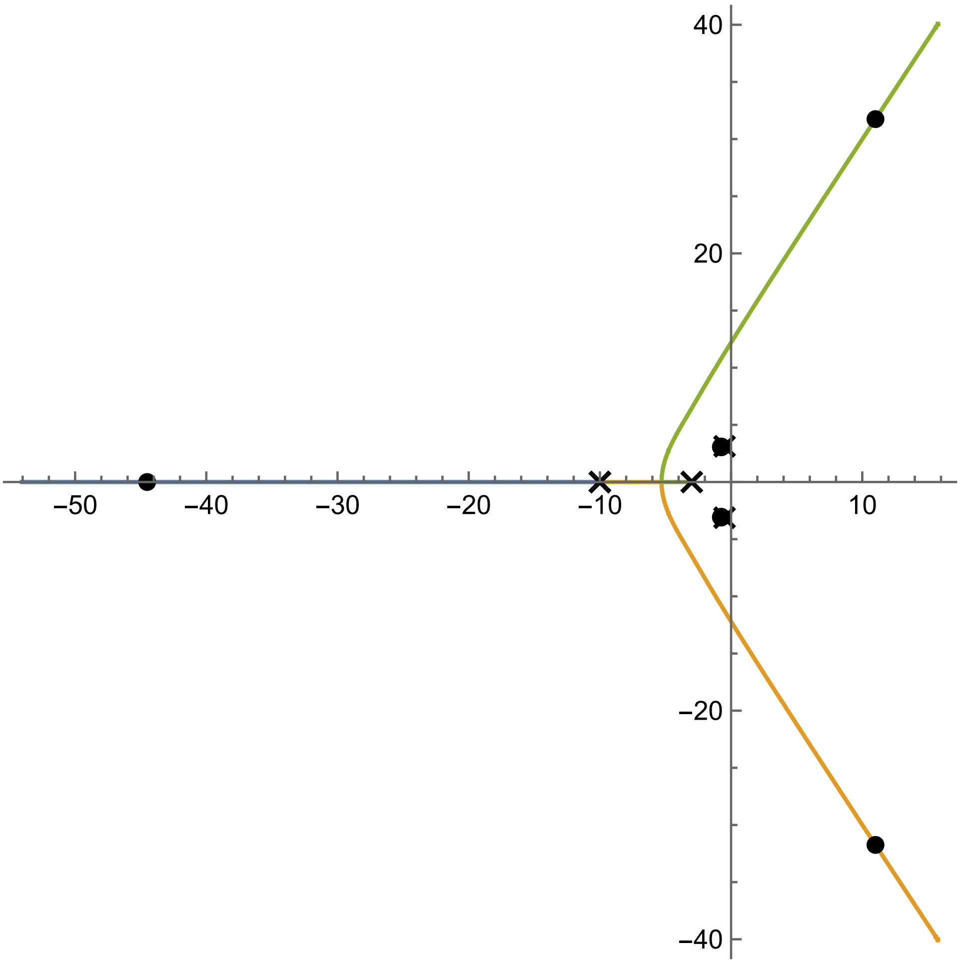

Figure 17 The root-locus plot of the compensated system where x are zeros, and the dots are poles

The root-locus reveals that the system is now stable for very high gains. Additionally, we can see the notch filter's effect on the frequency response in the Bode plot:

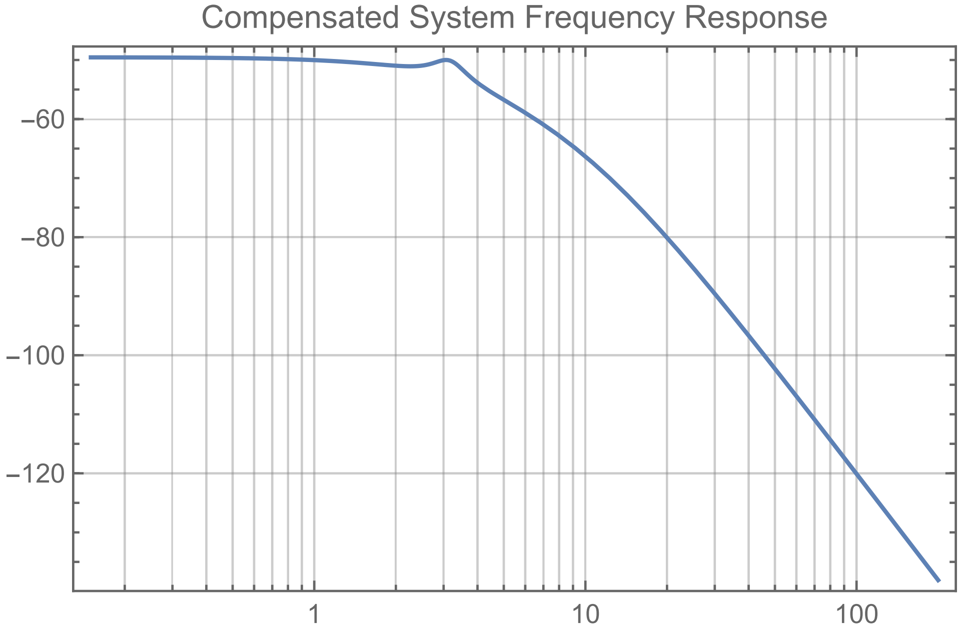

Figure 18 Gain Bode plot of compensated system

It appears that the peak has been smoothed by the compensator.

2.5. Spacecraft Modeling Using Quaternions

Since their introduction by the Irish mathematician William Hamilton in 1843, quaternions have transformed many scientific fields due to their unique properties which stem from the extension of the field of complex numbers $\mathbb{C}$ with applications in applied mechanics to computer graphics and, specifically relevant to this thesis, modeling of aerospace systems. Quaternion-based models have several advantages over Euler-based models, that so far in this thesis, have been discussed. The adoption of quaternion-based models is almost ubiquitous in the aerospace industry and has helped overcome several limitations that have plagued other models. First, a quaternion-based model does not depend on a rotation sequence as it is uniquely defined in contrast to Euler-angle-based models which can vary for different rotation sequences. This makes group design challenging and error prone if the same rotation sequence is not adopted by everyone working on the design. Another crucial advantage is that quaternion-based models do not contain singular points in any rotational sequence allowing for a globally stable solution to be achieved using optimal control techniques directly on the nonlinear model.

2.5.1. Quaternion Algebra and Operators

A set of Euler angles describes a rotation as a series of rotations that rotate around the principal axes of a system defined by the axes X, Y, Z. A quaternion on the other hand, describes a rotation by a rotational angle around a rotational axis that is proper to the rotational angle that is not necessarily the axes X, Y, Z. A key characteristic of quaternions is that they are non-commutative. This means that the product of two quaternions is different depending on the order and sign of the factors involved. Let $\vec{\mathbf{i}}$, $\vec{\mathbf{j}}, \vec{\mathbf{k}}$ be a standard basis in $\mathbb{R}^3$ which satisfies the condition:

$$\mathbf{i}^2 = \mathbf{j}^2 = \mathbf{k}^2 = \mathbf{ijk} = -1 \quad (26)$$

Let $\bar{q}$ be the 4-touple of real numbers:

$$\bar{q} = (q_0, q_1, q_2, q_3) \quad (27)$$

$\bar{q}$ is a quaternion when defined as the sum of a scalar and a vector in the following way:

$$\bar{q} = q_0 + \mathbf{i}\, q_1 + \mathbf{k}\, q_2 + \ \mathbf{j}\, q_3 \quad (28)$$

Where $q = \mathbf{i}\, q_1 + \mathbf{k}\, q_2\, \mathbf{j}\, q_3$ is the vector part and q_0 is the scalar part. In aerospace engineering, the normalized quaternion is used. This is a special type of quaternion where:

- $q_0 = \cos\frac{\alpha}{2}$
- $q = \hat{\mathrm{e}}\ \sin\frac{\alpha}{2}$

Where α is the rotational angle and ê is unit length of the rotational axis.

2.5.1.1. Equality and Addition Operators

For the quaternions:

$$\bar{p} = p_0 + \mathbf{i}\, p_1 + \mathbf{k}\, p_2 + \ \mathbf{j}\, p_3$$

$$\bar{q} = q_0 + \mathbf{i}\, q_1 + \mathbf{k}\, q_2 + \ \mathbf{j}\, q_3$$

We can say that $\bar{p} = \bar{q}$ if and only if:

$$p_0 = q_0, \qquad p_1 = q_1, \qquad p_2 = q_2, \qquad p_3 = q_3$$

In the context of aerospace engineering, two equal quaternions will represent the same rotation angle and the same rotational axis. The sum of two quaternions follows from the equality definition:

$$\bar{p} + \bar{q} = (p_0 + q_0) + \mathbf{i}\,(p_1 + q_1) + \mathbf{j}\,(p_2 + p_2) + \mathbf{k}\,(p_3 + q_3)$$

Note: The zero quaternion has a scalar and vector part of zero.

2.5.1.2. Identity and Multiplication

The basis definition results in the following relations:

$$\mathbf{i\,j} \ = \mathbf{k} = -\mathbf{j\,i}$$

$$\mathbf{j\,k} = \mathbf{i} = -\mathbf{k\,j}$$

$$\mathbf{k\,i} \ = \mathbf{j} = -\mathbf{i\,k}$$

The multiplication of two quaternions is the tensor product:

$$\bar{p} \otimes \bar{q} = p_1 q_1 - p_0 q + q_0 p + p \times q$$

Where p and q are the vector parts of the quaternions $\bar{p}$ and $\bar{q}$ respectively. The geometrical interpretation of the product of two quaternions is a composed rotation of two successive rotations conducted in the order of the factors. For the products:

$$\bar{r}_1 = \bar{p} \otimes \bar{q}$$

$$\bar{r}_2 = \bar{q} \otimes \bar{p}$$

Then:

$$\bar{r}_1 \neq \bar{r}_2$$

However:

$$\bar{r}_1 \otimes \bar{r}_2 = 1$$

2.5.1.3. Complex Conjugate, Inverse & Norm

The complex conjugate of a quaternion $\bar{q}$ is defined as:

$$\bar{q}^* = q_0 - q$$

$$\therefore \bar{q}^* = q_0 - \mathbf{i}\, q_1 - \mathbf{k}\, q_2 - \mathbf{j}\, q_3$$

It follows that:

$$\bar{q} + \bar{q}^* = (q_0 + q) + (q_0 - q)$$

$$\therefore \bar{q} + \bar{q}^* = 2q_0$$

Also:

$$(\bar{p} \otimes \bar{q})^* = \bar{p}^* \otimes \bar{q}^*$$

The norm of a quaternion is defined as:

$$\|\bar{q}\| = \sqrt{\bar{q}^* \otimes \bar{q}}$$

$$\therefore \|\bar{q}\| = \sqrt{q_0^2 + q_1^2 + q_2^2 + q_3^2}$$

The inverse of the quaternion is defined as:

$$\bar{q}^{-1} \otimes \bar{q} = \bar{q} \otimes \bar{q}^{-1} = 1$$

Post multiplying the left-hand-side and pre-multiplying the right-hand-side by $\bar{q}^*$:

$$\bar{q}^{-1} \otimes \bar{q} \otimes \bar{q}^* = \bar{q}^* \otimes \bar{q} \otimes \bar{q}^{-1} = \bar{q}^*$$

From () we have that:

$$\|\bar{q}\|^2 = \bar{q}^* \otimes \bar{q} = \bar{q} \otimes \bar{q}^*$$

$$\therefore \bar{q}^{-1} = \frac{\bar{q}^*}{\|\bar{q}\|^2}$$

The normalized quaternion satisfies the relationship:

$$\|\bar{q}\| = \sqrt{q_0^2 + q_1^2 + q_2^2 + q_3^2} = 1$$

Also satisfies:

$$\bar{q}^{-1} = \bar{q}^*$$

The norm of the product of two quaternions is the product of the individual norms:

$$\|\bar{p} \otimes \bar{q}\|^2 = \|p\|^2 \|q\|^2$$

2.5.1.4. Derivative of a Quaternion

The following the derivation of the expression for the derivative of a quaternion. For a quaternion $\bar{q}(t)$ in a reference frame a time t and $\bar{q}(t + \Delta t)$ be the same quaternion at time $t + \Delta t$. Let:

$$\bar{p}(t) = \cos\left(\frac{\Delta\alpha}{2}\right) + \hat{e}(t)\sin\left(\frac{\Delta\alpha}{2}\right) \tag{29}$$

Be the quaternion that brings $\bar{q}(t) \to \bar{q}(t + \Delta t)$. This means that $\bar{p}(t)$ is an incremental quaternion with a rotational axis $\hat{e}(t)$ and a rotational angle $\Delta\alpha$. For an infinitesimal variation we have $\Delta t \to 0$, $\sin\left(\frac{\Delta\alpha}{2}\right) \to \frac{\Delta\alpha}{2}$ and $\cos\left(\frac{\Delta\alpha}{2}\right) \to 1$. Therefore:

$$\bar{p}(t) \approx 1 + \hat{e}(t)\frac{\Delta\alpha}{2}$$

Since the product of two quaternions is the composition of the rotations that they represent, the product of $\bar{q}(t)$ and $\bar{p}(t)$ will bring $\bar{q}(t)$ to $\bar{q}(t + \Delta t)$:

$$\bar{q}(t + \Delta t) = \bar{q}(t) \otimes \left(1 + \hat{e}(t)\frac{\Delta\alpha}{2}\right)$$

Dividing by both sides, and letting $\Delta t \to 0$, we obtain the expression:

$$\frac{\mathrm{d}\bar{q}}{\mathrm{d}t} = \bar{q}(t) \otimes \big(1 + \hat{e}(t)\Omega(t)\big)$$

Where:

$$\Omega(t) = \lim_{\Delta t \to 0} \frac{\Delta\alpha}{\Delta t}$$

2.5.2. Spacecraft Dynamics Modeling with Quaternions:

A derivation of a the inertial and nadir pointing spacecraft models as well as the demonstration of their controllability is carried out in this section using the same notation as before.

A spacecraft that has the angular velocity vector $\omega_I = (\omega_x, \omega_y, \omega_z)$ with respect to the inertial frame, will have an angular momentum vector h_I about its center of mass. In the body frame the angular momentum vector will have the expression:

$$\mathrm{h} = \mathcal{J}\omega_I$$

T will be the external torque acting on the mass of the spacecraft where:

$$\mathrm{T} = \left(\frac{\mathrm{dh}_I}{\mathrm{d}t}\right)_b$$

Replacing h_I with h we obtain:

$$\mathrm{T} = \left(\frac{\mathrm{dh}}{\mathrm{d}t}\right) + \omega_I \times \mathrm{h}$$

Let the external torque acting on the spacecraft in the body frame be expressed by:

$$t_d = [t_{d1}, t_{d2}, t_{d3}]^T$$

The aggregation of the actuator control torques is expressed by:

$$\mathrm{u} = [u_1, u_2, u_3]^T$$

Combining actuator and disturbance torques results in the complete expression for the angular acceleration vector of the spacecraft in the body frame:

$$\begin{aligned} \mathcal{J}\dot{\omega}_I &= -\omega_I \times (\mathcal{J}\omega_I) + t_d + \mathrm{u} \\ &= -\mathrm{S}(\omega_I)(\mathcal{J}\omega_I) + t_d + \mathrm{u} \end{aligned} \tag{30}$$

Since we are describing the spacecraft dynamics using quaternions, we can make use of the notation presented previously to formulate the kinematics equations. Let $\hat{e}$ denote the rotational axis unit vector of the spacecraft in a body frame. It then follows from the previous discussion that the rotation of the body frame relative to the reference frame is described by the quaternion:

$$\bar{q} = \left[\cos\left(\frac{\alpha}{2}\right), \hat{e}^T \sin\left(\frac{\alpha}{2}\right)\right]^T$$

The spacecraft *body rate* with respect to the reference frame can be expressed as the state space:

$$\omega = \begin{bmatrix} \dot{q_0} \\ \dot{q_1} \\ \dot{q_2} \\ \dot{q_3} \end{bmatrix} = \frac{1}{2}\begin{bmatrix} 0 & -\omega_1 & -\omega_2 & -\omega_3 \\ \omega_1 & 0 & \omega_3 & -\omega_2 \\ \omega_2 & -\omega_3 & 0 & \omega_1 \\ \omega_3 & \omega_2 & -\omega_1 & 0 \end{bmatrix}\begin{bmatrix} q_0 \\ q_1 \\ q_2 \\ q_3 \end{bmatrix}$$

$$\omega = \frac{1}{2}\begin{bmatrix} q_0 & -q_1 & -q_2 & -q_3 \\ q_1 & q_0 & -q_3 & q_2 \\ q_2 & q_3 & q_0 & -q_1 \\ q_3 & -q_2 & q_1 & q_0 \end{bmatrix}\begin{bmatrix} 0 \\ \omega_1 \\ \omega_2 \\ \omega_3 \end{bmatrix} \tag{31}$$

The nonlinear model of the spacecraft can be assembled using the scalar and vector parts of the quaternion in the following way:

$$\begin{cases} \dot{q} = -\frac{1}{2}\omega \times q + \frac{1}{2}q_0\omega \\ \dot{q}_0 = -\frac{1}{2}\omega^T q \end{cases}$$

But the scalar part of the quaternion is nothing but:

$$q_0 = \sqrt{1 - q_1^2 + q_2^2 + q_3^2}$$

Therefore, we can reduce the expression (31) to:

$$\omega = \begin{bmatrix} \dot{q_1} \\ \dot{q_2} \\ \dot{q_3} \end{bmatrix} = \begin{bmatrix} \sqrt{1 - q_1^2 + q_2^2 + q_3^2} & -q_3 & q_2 \\ q_3 & \sqrt{1 - q_1^2 + q_2^2 + q_3^2} & -q_1 \\ -q_2 & q_1 & \sqrt{1 - q_1^2 + q_2^2 + q_3^2} \end{bmatrix} \begin{bmatrix} \omega_1 \\ \omega_2 \\ \omega_3 \end{bmatrix}$$

We can easily verify that:

$$\det \begin{bmatrix} \sqrt{1 - q_1^2 + q_2^2 + q_3^2} & -q_3 & q_2 \\ q_3 & \sqrt{1 - q_1^2 + q_2^2 + q_3^2} & -q_1 \\ -q_2 & q_1 & \sqrt{1 - q_1^2 + q_2^2 + q_3^2} \end{bmatrix} = \frac{1}{\sqrt{1 - q_1^2 + q_2^2 + q_3^2}}$$

For convenience, we can call the matrix on the left-hand-side $\mathrm{Q}(q_1, q_2, q_3)$. Unless α is $\pm\pi$ then Q is full rank.

Note: To further simplify, we can call $\begin{bmatrix} \dot{q_1} \\ \dot{q_2} \\ \dot{q_3} \end{bmatrix}$, $\mathrm{g}(q_1, q_2, q_3, \omega)$

2.5.2.1. Inertial Pointing Spacecraft Model

The simplest of the spacecraft models, the inertial pointing spacecraft model has several applications. Here, it is assumed that the spacecraft has no inertial bias, also to further simplify the equations, we assume that the disturbance torques are negligible. Therefore, the equation (30) can be simplified to:

$$\mathcal{J}\dot{\omega}_I = -\omega_I \times (\mathcal{J}\omega_I) + \mathrm{u}$$

The reduced kinematics expression will be the same as the expression (). We can linearize the model by using a Taylor expansion around the point $q_1 = q_2 = q_3 = 0$ and $\omega_I = 0$. Using:

$$\dot{\omega}_I \approx \mathcal{J}^{-1}\mathrm{u}$$

The Taylor linearization yields:

$$\frac{\partial \mathrm{g}}{\partial \omega_I} \approx \frac{1}{2} I_3$$

$$\frac{\partial \mathrm{g}}{\partial q} \approx \frac{1}{2} 0_3$$

The resulting linearized model in the state space form $\dot{\mathrm{x}} = \mathrm{Ax} + \mathrm{Bu}$:

$$\begin{bmatrix} \dot{\omega}_I \\ \dot{q} \end{bmatrix} = \begin{bmatrix} 0_3 & 0_3 \\ \frac{1}{2} I_3 & 0_3 \end{bmatrix} \begin{bmatrix} \omega_l \\ q \end{bmatrix} + \begin{bmatrix} \mathcal{J}^{-1} \\ 0_3 \end{bmatrix} \mathrm{u}$$

Where I_3 is a 3×3 dimensional identity matrix and 0_3 is a 3×3 zero matrix.
As shown, the proof that the linearized inertial spacecraft model is controllable is trivial.

2.5.2.2. Nadir Pointing Spacecraft Model

For this model we can assume a momentum bias on one of the axes hence obtaining the vector:

$$\mathrm{h} = [h_1, h_2, h_3]^T = [0, h_2, 0]^T$$

Therefore, that the kinematics expression is identical to equation (). For a nadir-pointing spacecraft, it is convenient to use the LVLH frame of reference. This means that the quaternion and spacecraft body rate will be represented in terms relative to the LVLH frame. In the body frame the rate ω was defined as the vector $(\omega_x, \omega_y, \omega_z)$. In the LVLH frame the rate is the *orbital rate* and is defined as:

$$\omega_{LVLH} = [0, -\omega_0, 0]^T$$

Also let us define v as the speed of the spacecraft and r the distance of the spacecraft to the center of the earth and p to be the orbital period, the time that the spacecraft takes to make one full rotation around the earth. For a circular orbit eccentricity $e = 0$, we have that the mean rate is given by:

$$\omega_0 = \frac{v}{r} = \frac{2\pi}{p}$$

For a rate ω_I in the body frame we can obtain the corresponding rate in the LVLH frame by using a transformation matrix A_I^b:

$$\omega_I = \omega + A_I^b \omega_{LVLH}$$

The term $A_I^b \omega_{LVLH}$ can be designated as ω_{LVLH}^b, the LVLH frame with respect to the inertial frame. Using the chain rule, we can obtain an expression for $\dot{\omega}_I$:

$$\dot{\omega}_I = \dot{\omega} + \dot{A}_I^b \omega_{LVLH} + A_I^b \dot{\omega}_{LVLH} \tag{32}$$

Replacing $\dot{A}_I^b$ with $-\omega \times A_I^b$ we obtain the expression:

$$\dot{\omega}_I = \dot{\omega} - \omega \times \omega_{LVLH} \tag{33}$$

Note that the term $\dot{\omega}_{LVLH}$ is very small for small eccentricities such as for circular orbits and can therefore be ignored.
We can now rewrite equation () using equations () and () as:

$$\mathcal{J}\dot{\omega}_I = \mathcal{J}\left(\omega \times \omega_{LVLH}^b\right) - \omega \times (\mathcal{J}\omega) - \omega \times \left(\mathcal{J}\omega_{LVLH}^b\right) - \omega_{LVLH}^b \times (\mathcal{J}\omega) - \omega_{LVLH}^b \times \left(\mathcal{J}\omega_{LVLH}^b\right) - \omega \times \mathrm{h} - \omega_{LVLH}^b \times \mathrm{h} + t_d + \mathrm{u} \tag{34}$$

Using the quaternion formulation described in (), we can write the transformation matrix A_I^b as:

$$A_I^b = \begin{bmatrix} 2q_0^2 - 1 + q_1^2 & 2q_1q_2 + 2q_0q_3 & 2q_1q_1 + 2q_0q_2 \\ 2q_1q_2 + 2q_0q_3 & 2q_0^2 - 1 + q_2^2 & 2q_2q_3 + 2q_0q_1 \\ 2q_1q_3 + 2q_0q_2 & 2q_2q_3 + 2q_0q_1 & 2q_0^2 - 1 + q_3^2 \end{bmatrix}$$

For convenience, we can designate the terms $\mathcal{J}\left(\omega \times \omega_{LVLH}^b\right) - \omega \times (\mathcal{J}\omega) - \omega \times \left(\mathcal{J}\omega_{LVLH}^b\right) - \omega_{LVLH}^b \times (\mathcal{J}\omega) - \omega_{LVLH}^b \times \left(\mathcal{J}\omega_{LVLH}^b\right) - \omega \times \mathrm{h} - \omega_{LVLH}^b \times \mathrm{h}$ as $\mathrm{f}\left(\omega, \omega_{LVLH}^b, \mathrm{h}\right)$. Designing a control system with the equation (34) is very difficult specially if there are design requirements and constraints. It is therefore common practice to design the controller for a linearized model of the spacecraft and later simulate the response to determine whether it is adequate or not. As with the inertial satellite model, the linearized model linearizes around the values $q_1 = q_2 = q_3 = 0$ and $\omega = 0$. The expression for the linearized system is:

$$\mathcal{J}\dot{\omega}_I \approx \frac{\partial \mathrm{f}}{\partial \omega}\omega + \frac{\partial \mathrm{f}}{\partial q} q + t_d + \mathrm{u} \tag{35}$$

The derivation for this equation can be found in [16].

2.5.3. Control of Spacecraft Using Quaternions

As discussed, in a closed-loop control system information regarding the system's state must be fed back to the controller in such a way that the controller, in this case an ACS, can perform an adequate task depending on the orientation of the spacecraft. If the command-and-control law is formulated using Euler-angles, then the ACS must compute the smallest rotation in terms of angles so that the aircraft is aligned with the target. If it is formulated using directional cosine matrices, then the control laws are given in terms of the elements in the matrix. Similarly, if the dynamics are formulated using quaternions, then there exists a *quaternion error vector* that provides between the error in the satellites attitude direction in space and the target direction. Let the following quaternions be:

- q_E, the error quaternion.
- q_T the target quaternion.
- q_S the spacecraft quaternion.

According to [17], the quaternion error vector is computed using the expression:

$$[\mathrm{A}(q_E)] = [\mathrm{A}(q_T)][\mathrm{A}(q_s)]^{-1} \tag{36}$$

For the transformation matrix $[\mathrm{A}]$. q_E in quaternion notation is thus:

$$q_E = \begin{bmatrix} q_{T4} & q_{T3} & -q_{T2} & q_{T1} \\ -q_{T3} & q_{T4} & q_{T1} & q_{T2} \\ q_{T2} & -q_{T1} & q_{T4} & q_{T3} \\ -q_{T1} & -q_{T2} & -q_{T3} & q_{T4} \end{bmatrix} \begin{bmatrix} -q_{S1} \\ -q_{S2} \\ -q_{S3} \\ q_{S4} \end{bmatrix} \tag{37}$$

The resulting control law can be developed from expression (25) which for each of the axes turns out to be:

$$\begin{aligned} T_{cx} &= 2K_x q_{1E} q_{4E} + K_{xd} p \\ T_{cy} &= 2K_x q_{1E} q_{4E} + K_{xd} q \\ T_{cz} &= 2K_x q_{1E} q_{4E} + K_{xd} r \end{aligned} \tag{38}$$

2.6. Design Process of an Attitude Control System

The design of an attitude control system is an iterative process which seeks to find the most appropriate solution for the orientation of the spacecraft which is dictated by its mission. The following table illustrates a design process for the ACS for a satellite, with the expected requirements for each step and expected outcomes of each step which have been designated as *inputs* and *outputs*, respectively.

Table 4 ACS design steps

Step	Input	Output
Specify control modes Derive system-level requirements by control mode	Mission requirements and profile as well as type of orbit insertion and launch vehicle.	Requirements and constraints, control modes for mission.
Description of disturbance environment	Structure geometry of spacecraft, orbit, solar and magnetic models & mission profile.	The type of stabilization control: 3-axis, spinning, gravity gradient, etc.
Specification of ACS hardware	Spacecraft mass and constraints, required accuracy, orbit geometry, mission length and expected lifetime, space environment, pointing direction.	Sensor suite & control actuator selection.

Selection of control algorithms	Stabilization method and required accuracy optimized with respect to system-level limitations such as power and thermal limitations and processor speed.	Apt parameters and control laws for each control mode.
Iteration and documentation	All the above	Refined description of system-level requirements and complete ACS design with subsystem and component specifications.

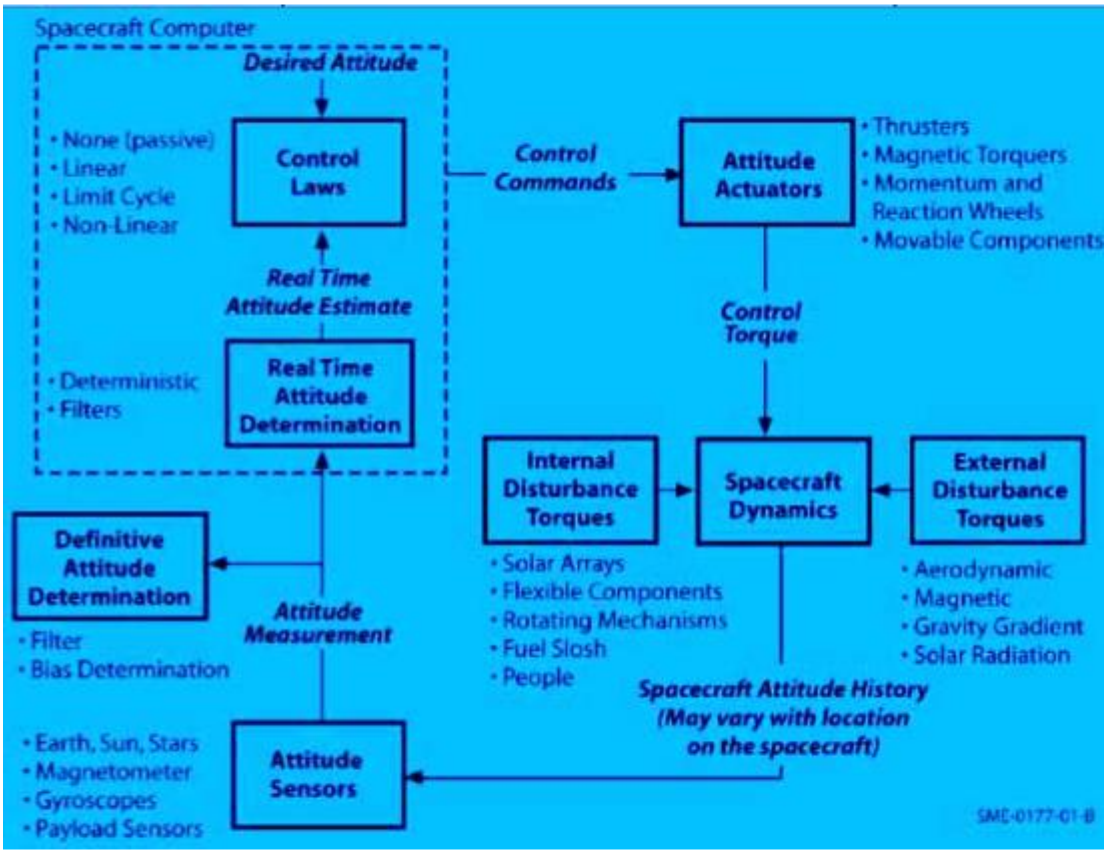

Figure 19 Diagram of ACS system [11]

The most important step in the conception of the ACS system is the specification of the control modes. These are the operating modes in which the spacecraft will find itself during different phases of the mission. The ACS will be expected to meet the goals of the mission at every step and therefore the best possible understanding of each mode must be reached before any further steps are taken in the design process. Engineers must also have sufficient information about the subsystems which the ACS

is dependent on such as the power and thermal control subsystems in order for the interactions between to be conductive to mission success.
The following table is a short description of some of the typical control modes for a satellite mission.

Table 5 Typical ACS modes

Control Mode	**Description**
Orbit insertion	Phase during which the spacecraft is being boosted to space or right after and before it has reached final orbit. ACS control may take the form of spin-stabilization or possibly complete stabilization using thruster control.
Acquisition	This mode involves the initialization of the attitude determination system and the stabilization of the spacecraft for communication with ground stations as well as for power generation. This mode can be invoked after upsets or emergencies.
On-station	This mode is used for the largest portion of the spacecraft's service-life and should drive the system design.
Slew	Triggered when reorientation is necessary.
Contingency mode or Safe mode	If a system or mode fails, safe mode is triggered. Generally, meets designed to meet minimal power and thermal requirements.
Special modes	During special mission conditions, an alternative mode to the normal "on-station" mode may be triggered by design. This may include periods such as passing through a celestial body's shadow or *umbra,* for example.

Dividing the spacecraft's mission operational conditions into control modes is convenient from a system design standpoint and it follows that the successful execution of the mission will depend on the performance of the spacecraft in each of the modes. The determination of the spacecraft's performance, whether it is adequate or not to meet mission requirements, can be done by specifying the *control performance requirements.* As expected, each mode must have a unique set of performance requirements from the ACS. The following table lists and defines the most frequently specified performance parameters:

Table 6 ACS design parameters

Parameter	Definition	Examples & observations
Accuracy	Knowledge and control of the spacecraft's attitude relative to an absolute reference.	$0.15°$ Or 2σ. Often includes errors and tolerances. Each axis might have different parameters.
Range	The range of angular motion the ACS must successfully operate in.	Rates in $\mathrm{rad/s}$ or degrees from nadir.
Jitter	High-frequency angular motion.	Key in maintaining sensor data quality. $0.01°/\mathrm{min}$ for example.
Drift	Low-frequency angular motion	Some disturbances or command inputs may trigger drift. $0.05°/\mathrm{hour}$ for example.
Transient Response	Specified settling time or overshoot when attitude adjustments are made whether acquiring targets or rejecting disturbances	For example, 10% maximum overshoot.

3. Modeling Fluid Slosh

3.1. Fluid Sloshing Problem

Fluid slosh, particularly propellant fluid slosh has been a problem ever since the launch of the earliest high-efficiency rockets such as the Jupiter intermediate range ballistic missile which in April of 1957 suffered an early termination, 90 seconds after launch, due to excessive propellant slosh which rendered it uncontrollable.

The problem persists today and is the subject of extensive research and development as today's increasingly complex spacecraft have a substantial proportion of their mass occupied by propellant. For example, a typical satellite in GEO will have roughly 40% of its mass as propellant fluid. Fluids which are contained in tanks which are only partially filled have a free-surface boundary which when interfacing with the tank boundaries will result in internal translational and rotational accelerations which perturb the spacecraft's attitude.

The earliest solutions devised to address slosh dynamics' effects on spacecraft consisted in the introduction of physical barriers known as *baffles* within the tanks as well as compartmentalization which turned high amplitude low frequency slosh into low amplitude high frequency slosh. Another solution based on physical boundaries introduced subsequently have been bladders.

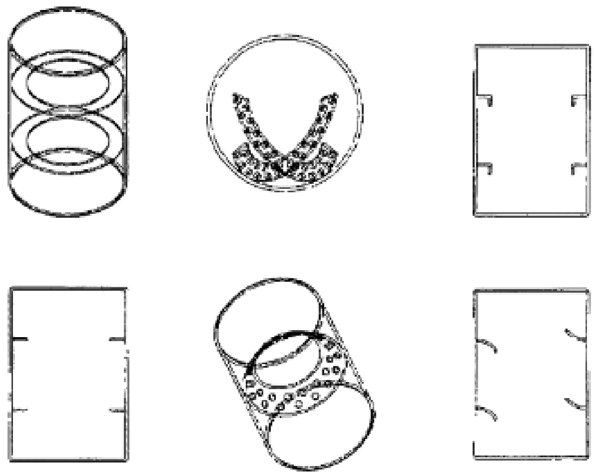

Figure 20 common baffle types [19]

Baffle increased in complexity and sophistication as a deeper and more detailed understanding of fluid slosh dynamics, mission modes as well as computational tools were developed to aid in solving the fluid slosh problem.

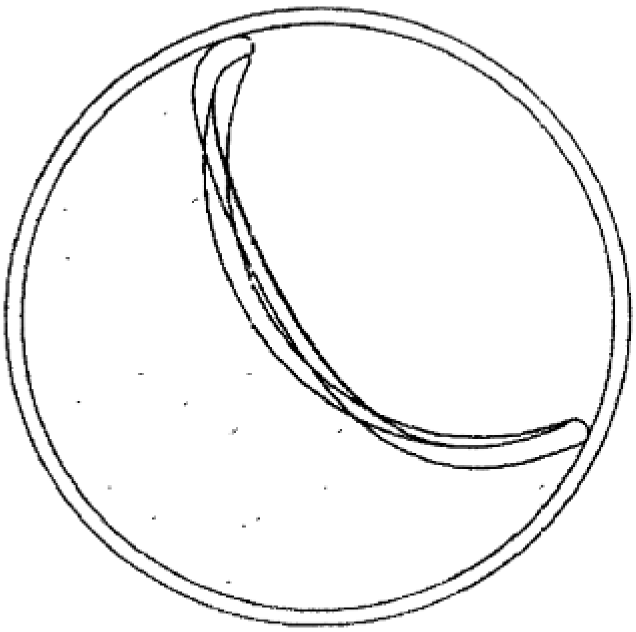

Figure 21 Fuel bladder [17]

Biswal et al. developed mathematical models for studying fuel slosh in tanks containing baffles by solving the velocity potential function using finite element analysis which led to the development of models for the simulation of control systems for rejecting slosh torque. Typically, nonlinearities in the model such as compressibility, viscosity and vorticity are not taken into account in order to reduce complexity and computational effort required to simulate the fluid dynamics. Despite the development of complex mathematical and computational tools, precisely modeling the fluid slosh a spacecraft will experience during its mission remains an extremely difficult task. It is therefore common practice to obtain the slosh torque frequencies experimentally prior to launch, if possible.

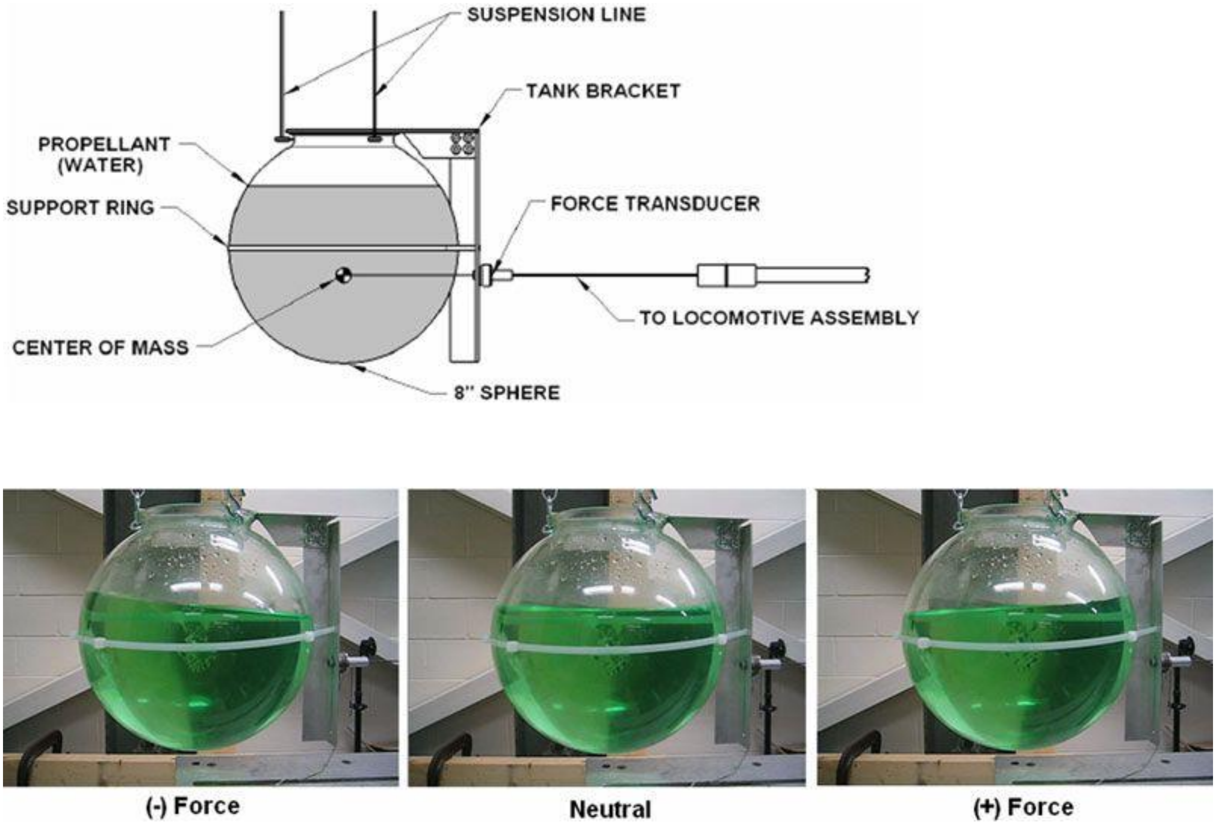

Figure 22 Fluid slosh test assembly [37]

Peterson et al. have demonstrated that the fluid slosh dynamics can be approximated to the dynamics of simpler, more understood models such as the mass-spring model and the pendulum model. For accelerating spacecraft these models have been used extensively to counter the effects of fluid slosh with thrust vectoring using a linear model control design. In the following, the mathematical formulation for a planar spacecraft with liquid slosh will be presented using both the pendulum analogy and the mass-spring analogy.

Low-g slosh is a very active area of study due to the prevalence of nonlinear phenomena in the determination of the fluid dynamics. The shape and movement of the fluid is determined by the capillary, convective and viscous forces rather than the gravitational force which is typically the dominant force [18]. The scope of this thesis is does not cover low g-sloshing and therefore only models where sloshing occurs during acceleration are considered.

3.2. Pendulum Analogy

Following the work of Cho et. al [20], for this analogy only the following assumptions are made:

- The spacecraft is a rigid body, the *base body*.
- The sloshing fluid is contained as an internal body.
- The fluid is incompressible and nonlinear effects are ignored.
- It is possible to derive internal dissipative forces using a Rayleigh dissipation function $\mathcal{R}$.
- The mass and inertia of the spacecraft (fuel and vehicle) remain constant.
- Gravitational effects are neglected.

The equations of motion are developed in terms of the spacecraft translational velocity vector, the angular velocity and the internal *shape* coordinate that represents the sloshing modes.

Using Cho's formulation we have that $\mathrm{v}, \omega, \eta \in \mathbb{R}^3$ where:

- v is the translational velocity vector in the body frame.
- ω is the angular velocity vector of the base body.
- η is the internal coordinate.

Using the Lagrangian formulation it is possible to obtain the equations of motion of the spacecraft. The Lagrangian in these coordinates is of the form:

$$\mathcal{L} = \mathcal{L}(\mathrm{v}, \omega, \eta, \dot{\eta}) \tag{36}$$

Because the Lagrangian does not depend on the position or attitude of the spacecraft, it is *SE(3)-invariant.* The Euler-Lagrange equations yield a set of second order differential equations in terms of the generalized forces and moments which consist of control inputs that can be placed into two distinct categories; external torques τ_t which are applied via thrusters or magnetorquers, and internal torques τ_r which are applied via momentum or torque wheels. The Euler-Lagrange equations:

$$\frac{\mathrm{d}}{\mathrm{d}t}\frac{\partial \mathcal{L}}{\partial \mathrm{v}} + \hat{\omega}\frac{\partial \mathcal{L}}{\partial \mathrm{v}} = \tau_t \qquad (37,38,39)$$

$$\frac{\mathrm{d}}{\mathrm{d}t}\frac{\partial \mathcal{L}}{\partial \omega} + \hat{\omega}\frac{\partial \mathcal{L}}{\partial \omega} + \hat{\mathrm{v}}\frac{\partial \mathcal{L}}{\partial \mathrm{v}} = \tau_r$$

$$\frac{\mathrm{d}}{\mathrm{d}t}\frac{\partial \mathcal{L}}{\partial \dot{\eta}} - \frac{\partial \mathcal{L}}{\partial \eta} + \frac{\partial \mathcal{R}}{\partial \dot{\eta}} = 0$$

It is evident from the equations that there is not force that directly controls the internal dynamics.

3.2.1. Derivation of the Planar Nonlinear Equations of Motion:

Although ACS thrusters cannot be throttled, let us assume we have a spacecraft which throttelable side thrusters. Then let v_x, v_z the transverse components of the center-of mass of the tank. θ is the angle of the spacecraft with respect to the longitudinal axis of the absolute frame of reference and the angle ψ the position of the pendulum with respect to it's equilibrium which is the spacecraft's longitudinal axis. Let

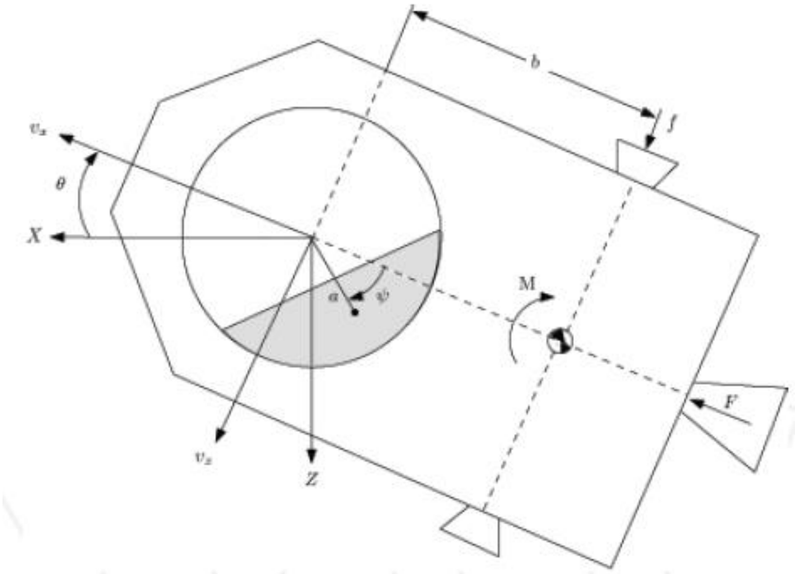

Figure 23 A single slosh pendulum model for a spacecraft

F be the thrust, a force acting on base body's longitudinal axis and f be a transverse force acting perpendicular to the perpendicular body representing the control inputs as well as a pitching moment M.

From figure 17, the distance b is the distance between the pendulum point of attachment and the center of mass of the spacecraft. The moment of inertia of the tank I_f and the mass of the fuel m_f as well as the length of the pendulum a depend on the shape of the fuel tank, which here is assumed to be a perfect sphere as well as the characteristics of the fuel and it's fill ratio. Finally, let $\hat{\imath}$ and $\hat{k}$ denote unit vectors along the reference frame situated along the longitudinal and transverse axes (x, z) respectively, within which the inertial position of the tank can be determined. The expression for the position vector of the center of mass of the vehicle is body fixed frame is:

$$\vec{r} = (x - b)\hat{\imath} + z\hat{k} \tag{40}$$

The derivative of () is the inertial velocity:

$$\dot{\vec{r}} = (\dot{x} - z\dot{\theta})\hat{\imath} + (\dot{z} - x\dot{\theta} + b\dot{\theta})\hat{k} \tag{41}$$

Using $(\dot{x} - z\dot{\theta}) = v_x$ and $(\dot{z} - x\dot{\theta}) = v_z$ we have:

$$\therefore \dot{\vec{r}} = v_x\hat{\imath} + (v_z + b\dot{\theta})\hat{k} \tag{42}$$

The velocity of the fuel mass is given by:

$$\dot{\vec{r}}_f = \left[\dot{x} + a\,\dot{\psi}\sin\psi + \dot{\theta}(z + a\sin\psi)\right]\hat{\imath} + \left[\dot{z} + a\,\dot{\psi}\cos\psi - \dot{\theta}(x - a\ \cos\psi)\right]\hat{k} \tag{43}$$

$$\therefore \dot{\vec{r}}_f = \left[v_x + a\,\left(\dot{\theta} + \dot{\psi}\right)\sin\psi\right]\hat{\imath} + \left[v_z + a\,\left(\dot{\theta} + \dot{\psi}\right)\cos\psi\right]\hat{k}$$

Since gravitational effects are neglected, the potential energy of the lumped system is zero and therefore the Lagrangian is equal to the expression for the kinetic energy $\mathcal{L} = T$, where:

$$T = \frac{1}{2}m\dot{\vec{r}}^2 + \frac{1}{2}m_f\dot{\vec{r}}_f^{\,2} + \frac{1}{2}I\dot{\theta}^2 + \frac{1}{2}I_f\left(\dot{\theta} + \dot{\psi}\right)^2 \tag{43}$$

Replacing $\dot{\vec{r}}$ and $\dot{\vec{r}}_f$ with their corresponding expressions we obtain:

$$T = \frac{1}{2}m\left[{v_x}^2 + \left(v_z + b\dot{\theta}\right)^2\right] + \frac{1}{2}m_f\left\{\left[v_x + a\,\left(\dot{\theta} + \dot{\psi}\right)\sin\psi\right]^2 + \left[v_z + a\,\left(\dot{\theta} + \dot{\psi}\right)\cos\psi\right]^2\right\} + \frac{1}{2}I\dot{\theta}^2 + \frac{1}{2}I_f\left(\dot{\theta} + \dot{\psi}\right)^2 \tag{44}$$

In order to apply the Euler-Lagrange equations to the Lagrangian we use:

- $\eta = \psi$
- $\mathcal{R} = \frac{1}{2}\epsilon\,\dot{\psi}^2$
- $\mathrm{v} = \begin{bmatrix} v_x \\ 0 \\ v_z \end{bmatrix}$
- $\omega = \begin{bmatrix} 0 \\ \dot{\theta} \\ 0 \end{bmatrix}$
- $\tau_t = \begin{bmatrix} F \\ 0 \\ f \end{bmatrix}$
- $\tau_r = \begin{bmatrix} 0 \\ M + fb \\ 0 \end{bmatrix}$

The equations of motion obtained are 4 coupled nonlinear second order differential equations:

$$\left(m + m_f\right)\left(\dot{v_x} + \dot{\theta}v_z\right) + m_f\ a\left(\ddot{\theta} + \ddot{\psi}\right)\sin\psi + mb\dot{\theta}^2 + m_f a\left(\dot{\theta} + \dot{\psi}\right)^2\cos\psi = F \tag{43}$$

$$\left(m + m_f\right)\left(\dot{v_z} + \dot{\theta}v_x\right) + m_f\ a\left(\ddot{\theta} + \ddot{\psi}\right)\cos\psi + mb\dot{\theta}^2 + m_f a\left(\dot{\theta} + \dot{\psi}\right)^2\sin\psi = f$$

$$(I + mb^2)\ddot{\theta} + mb\left(\dot{v_z} + \dot{\theta}v_x\right) - \epsilon\dot{\psi} = M + bf$$

$$\left(I_f + m_f a^2\right)\left(\ddot{\theta} + \ddot{\psi}\right) + m_f a\left[\left(\dot{v_z} + \dot{\theta}v_x\right)\sin\psi + \left(\dot{v_z} + \dot{\theta}v_x\right)\cos\psi\right] + \epsilon\dot{\psi} = 0$$

3.2.2. Mass-spring Analogy

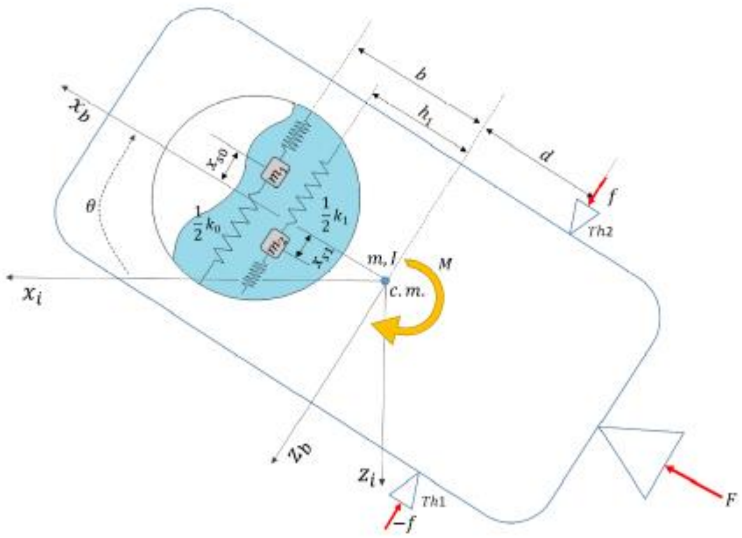

Figure 24 Mass-spring analogy for slosh in spacecraft [19]

While in the pendulum analogy model the system captured the lowest slosh frequency, in this model we can add two mass-spring systems with different stiffness constants k_1 and k_2 to obtain the first two slosh frequencies of the fluid. The model can have as many mass-spring systems as desired depending on the design requirements. Using the same coordinate system and convention as before, the main body frame will have the same position and velocity vectors as will the pendulum analogy. The model developed by Reyhanoglu & Hervas is used as reference [20]. We can further develop the expression (41) to obtain:

$$\ddot{\vec{r}} = \left(a_x + b\dot{\theta}^2\right)\hat{\imath} + \left(a_z + b\ddot{\theta}\right)\hat{k} \tag{44}$$

Where $a_x = \left(\dot{v}_x + v_z\dot{\theta}\right)$ and $a_z = \left(\dot{v}_z + v_x\dot{\theta}\right)$.

The equations for the fluid slosh consist in the dynamic equations for the spring-mass system. For two masses, we have two equations, the position of the first mass is given by:

$$\vec{r}_0 = (x + b)\hat{\imath} + z\hat{k} \tag{44,45}$$

$$\vec{r}_i = (x + h_i)\hat{\imath} + \left(z + x_{s,i}\right)\hat{k}$$

And for the second mass:

$$\vec{r}_i = (x + h_i)\hat{\imath} + \left(z + x_{s,i}\right)\hat{k}$$

The accelerations corresponding to each mass respectively can be obtained from the second derivative of each of the expressions:

$$\ddot{\vec{r}}_0 = \left(a_x - h_0\dot{\theta}^2 + \ddot{h}_0\right)\hat{\imath} + \left(a_z - 2h_0\dot{\theta} - \ddot{h}_0\ddot{\theta}\right)\hat{k} \tag{45,46}$$

$$\ddot{\vec{r}}_i = \left(a_x + h_i\dot{\theta}^2 + \ddot{h}_i + x_{s,i}\ddot{\theta} + \dot{x}_{s,i}\dot{\theta}\right)\hat{\imath} + \left(a_z - 2h_i\dot{\theta}^2 - h_i\ddot{\theta} + \ddot{x}_{s,i} + x_{s,i}\dot{\theta}^2\right)\hat{k}$$

Finally, let c_i be a constant for the dissipative effects due to the natural viscous effects on the fluid interfacing with the tank walls, we have that:

$$m_i\left(\ddot{x}_{s,i} + x_{s,i}\dot{\theta}^2 + a_z - 2h_i\dot{\theta}^2 - h_i\ddot{\theta}\right) = -c_i\dot{x}_{s,i} - k_i x_{s,i} \tag{47}$$

The equations of motion can be obtained using the Lagrangian formulation, which is of the form:

$$\mathcal{L} = \mathcal{L}(\theta, \omega, x_1, \dot{x}_1, x_2, \dot{x}_2)$$

As before, since we are not taking gravitational effects, we have that $\mathcal{L} = T$. Applying the Euler-Lagrange equations to $\mathcal{L}$ we obtain four equations of motion which are coupled and nonlinear:

$$\left(m + m_f\right)\left(\dot{v_x} + \dot{\theta}v_z\right) + m_0\ddot{h}_0 + \sum_{i=1}^{n} m_i\left(x_{s,i}\ddot{\theta} + 2\dot{x}_{s,i}\dot{\theta} + \ddot{h}_i\right) = F$$

$$\left(m + m_f\right)\left(\dot{v_z} + \dot{\theta}v_x\right) + mb\ddot{\theta} - 2m_0\dot{h}_0\dot{\theta} + \sum_{i=1}^{n} m_i\left(\ddot{x}_{s,i} - x_{s,i}\dot{\theta}^2 - 2\dot{h}_i\dot{\theta}\right) = f$$

$$\begin{aligned}\left(I + I_0 + mb^2 + m_0h_0^2 + \sum_{i=1}^{n}\{I_i + m_i(h_i^2 + s_i^2)\}\right)\ddot{\theta} \\ + \sum_{i=1}^{n} m_i\left\{x_{s,i}\left(\dot{v_x} + v_z\dot{\theta}\right) - h_i\ddot{x}_{s,i} + 2\left(x_{s,i}\dot{x}_{s,i} + h_i\dot{h}_i\right)\dot{\theta} + x_{s,i}\ddot{h}_i\right\} \\ + 2m_0h_0\dot{h}_0\dot{\theta}_0 + mb\left(\dot{v_z} + \dot{\theta}v_x\right) = f(b + d)\end{aligned}$$

$$m_i\left(\ddot{x}_{s,i} + x_{s,i}\dot{\theta}^2 + a_z - 2h_i\dot{\theta}^2 - h_i\ddot{\theta}\right) + c_i\dot{x}_{s,i} + k_i x_{s,i} = 0 \tag{48}$$

By removing the coupled terms and simplifying the equation yields a linear system of two second order differential equations as found in [19]. The following is a simulation of the linear system, where the state space is derived from the linear equations. Subsequently, an optimal controller is implemented to stabilize the spacecraft and reject the slosh disturbance from a set of non-zero initial conditions.

3.2.2.1. Mathematica Mass-Spring Analogy Simulation

State space model matrices for linearized model of the spacecraft dynamics with two slosh modes modeled after a pair of spring mass systems:

In[ ]:= $$\mathcal{A} = \begin{pmatrix} 0 & 1 & 0 & 0 & 0 & 0 \\ 0 & 0 & \frac{-b\,k_1}{\mathcal{I}} & \frac{-b\,c_1}{\mathcal{I}} & \frac{-b\,k_2}{\mathcal{I}} & \frac{-b\,c_2}{\mathcal{I}} \\ 0 & 0 & 0 & 1 & 0 & 0 \\ 0 & 0 & \frac{-k_1\,c}{m\,m_{f_1}\,\mathcal{I}} & \frac{-c_1\,c}{m\,m_{f_1}\,\mathcal{I}} & \frac{-k_2\,b}{\mathcal{I}} & \frac{-c_2\,b}{m\,\mathcal{I}} \\ 0 & 0 & 0 & 0 & 0 & 1 \\ 0 & 0 & \frac{-k_1\,b}{m\,\mathcal{I}} & \frac{-c_1\,b}{m\,\mathcal{I}} & \frac{-k_2\,d}{m\,m_{f_2}\,\mathcal{I}} & \frac{-c_2\,d}{m\,m_{f_2}\,\mathcal{I}} \end{pmatrix} \;/.\; \mathcal{I} \to \mathcal{I}_1 + \mathcal{I}_2;$$

In[ ]:= $$\mathcal{B} = \begin{pmatrix} 0 & 0 \\ \frac{d}{\mathcal{I}} & \frac{1}{\mathcal{I}} \\ 0 & 0 \\ \frac{\mathcal{I}-b\,d\,m}{\mathcal{I}} & \frac{b}{\mathcal{I}} \\ 0 & 0 \\ \frac{\mathcal{I}-b\,d\,m}{\mathcal{I}} & \frac{b}{\mathcal{I}} \end{pmatrix};$$

In[ ]:= $$\mathcal{C} = \begin{pmatrix} 1 & 0 & 0 & 0 & 0 & 0 \\ 0 & 0 & 1 & 0 & 0 & 0 \\ 0 & 0 & 0 & 0 & 1 & 0 \end{pmatrix};$$

The parameters of the spacecraft model:

In[ ]:= pars = $\{m \to 2523,\ m_{f_1} \to 776.9,\ m_{f_2} \to 21.6,\ \mathcal{I} \to 4200,\ \mathcal{I}_1 \to 82,$
$\mathcal{I}_2 \to 8,\ F \to 485,\ b \to 2,\ d \to 2,\ h_1 \to 0.6,\ h_2 \to 0.055,\ \rho \to 1020,\ \mathcal{R}_0 \to 0.72,$
$\sigma_{prop} \to 66.7,\ c_1 \to -0.2295,\ c_2 \to -0.0135,\ k_1 \to -3.1455,\ k_2 \to -0.63\};$

Compute the state space model using the matrices and parameters above:

In[ ]:= ssm = StateSpaceModel[$\{\mathcal{A}, \mathcal{B}, \mathcal{C}\}$,
SystemsModelLabels $\to \{\{\mathcal{T}_1, \mathcal{T}_2\}, \{\theta, x_1, x_2\}, \{\theta, \theta', x_1, x_1', x_2, x_2'\}\}$] /.
$\{b \to m\,b^2 + \mathcal{I},\ c \to m\,m_{f_1}\,b^2 + a,\ d \to m\,m_{f_2}\,b^2 + e\}$ /. $\{a \to \mathcal{I}\,(m + m_{f_1}),\ e \to \mathcal{I}\,(m + m_{f_2})\}$ /. pars;
ssm // N

Out[ ]=

							$\mathcal{T}_1$	$\mathcal{T}_2$
θ	0.	1.	0.	0.	0.	0.	0.	0.
θ'	0.	0.	0.0699	0.0051	0.014	0.0003	0.00047619	0.000238095
x_1	0.	0.	0.	1.	0.	0.	0.	0.
x_1'	0.	0.	0.386924	0.0282305	100.044	0.000849703	-1.40286	0.00047619
x_2	0.	0.	0.	0.	0.	1.	0.	0.
x_2'	0.	0.	0.197981	0.0144449	1.40076	0.0300164	-1.40286	0.00047619
θ	1.	0.	0.	0.	0.	0.	0	0
x_1	0.	0.	1.	0.	0.	0.	0	0
x_2	0.	0.	0.	0.	1.	0.	0	0

S

The open-loop response is totally unstable:

In[ ]:=
```
or = OutputResponse[{ssm, {0, 0, 0, 0, 0.2, 0}}, {0, 0}, {t, 0, 10}];
Plot[#[[1]], {t, 0, 10}, PlotRange → All, PlotLabel → #[[2]]] & /@ Thread[{or, {θ, x₁, x₂}}]
```

Out[ ]=

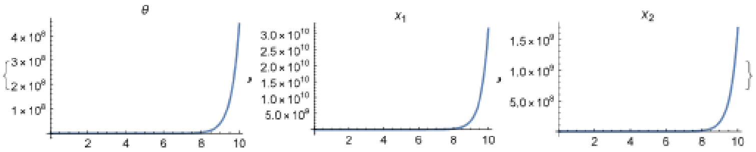

Controlling the model using an optimal controller requires the definition of the weighting and cost matrices for the states and control inputs respectively:

In[247]:=
```
{q, r} = {DiagonalMatrix[{10, 1, 100, 10, 100, 10}], 0.1 DiagonalMatrix[{1, 1}]};
Grid[{MatrixForm /@ {q, r}}, Frame → All, FrameStyle → Gray]
```

Out[248]=

$$\begin{pmatrix} 10 & 0 & 0 & 0 & 0 & 0 \\ 0 & 1 & 0 & 0 & 0 & 0 \\ 0 & 0 & 100 & 0 & 0 & 0 \\ 0 & 0 & 0 & 10 & 0 & 0 \\ 0 & 0 & 0 & 0 & 100 & 0 \\ 0 & 0 & 0 & 0 & 0 & 10 \end{pmatrix} \quad \begin{pmatrix} 0.1 & 0. \\ 0. & 0.1 \end{pmatrix}$$

Compute the Linear Quadratic Controller (LQR) controller data object:

In[ ]:=
```
cd = LQRegulatorGains[ssm, {q, r}, "Data"]
```

Out[ ]= SystemsModelControllerData[Design: linear quadratic regulator » Feedback inputs count: 2]

From the data object, it is possible to obtain the feedback gains of the LQR and the closed-loop system with the controller in the feedback path:

In[249]:=
```
{κ, csys} = {cd["FeedbackGains"], cd["ClosedLoopSystem"]};
Grid[{{MatrixForm@%[[1]], csys}}ᵀ, Frame → All, FrameStyle → Gray]
```

Out[250]=

$$\begin{pmatrix} -9.93237 & -98.01 & -34.6523 & -14.8953 & -174.204 & -7.48969 \\ 1.16104 & 11.0383 & 0.298761 & 0.0442733 & 0.233122 & -0.0162935 \end{pmatrix}$$

	0.	1.	0.	0.	0.	0.	0.	0.
	0.00445326	0.0440433	0.08633	0.0121825	0.0968989	0.0038704	0.00047619	0.000238095
	0.	0.	0.	1.	0.	0.	0.	0.
	-13.9343	-137.499	-48.2255	-20.8678	-144.34	-10.5061	-1.40286	0.00047619
	0.	0.	0.	0.	0.	1.	0.	0.
	-13.9343	-137.499	-48.4144	-20.8816	-242.983	-10.4769	-1.40286	0.00047619
θ	1.	0.	0.	0.	0.	0.	0.	0.
x_1	0.	0.	1.	0.	0.	0.	0.	0.
x_2	0.	0.	0.	0.	1.	0.	0.	0.

The simulation of the closed-loop response to a disturbance in the mass positions yields a stable response:

In[ ]:=
```
OutputResponse[{csys, {0, 0, 0.1, 0, 0.2, 0}}, {0, 0}, {t, 0, 10}];
Plot[%, {t, 0, 10}, PlotRange → All, PlotLegends → {"θ", "x1", "x2"}]
```

Out[ ]=

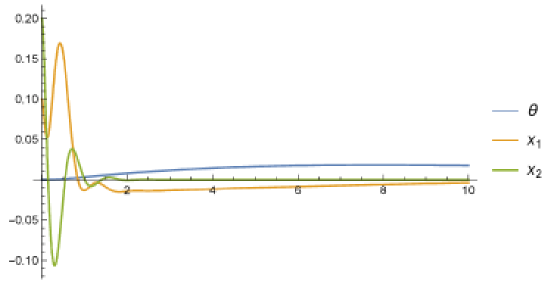

4. Ballbot-Inspired Satellite

Figure 25 The Rezero ballbot developed at ETH Zurich [7]

4.1. Conceptualization of Design

In this chapter, a novel design concept for a satellite is presented aimed at improving the attitude control system design and performance for a fuel depot satellite. Initially a cylindrical tank was proposed in order to maximize launcher fairing volume occupation as shown in the figure 20.

Figure 26 Initial satellite design

This design would include a satellite bus containing *housekeeping* subsystems as well as communications and power subsystems. The model of the satellite, dynamically, would resemble an inverted spherical pendulum. The inverted spherical pendulum is highly nonlinear and unstable system that would be difficult especially considering the complex fluid dynamics involved in storing fluids.

After going through different types of robotics systems in order to obtain a reference model for a satellite that has a large fuel tank as part of its structure which was to be contained on the exterior of the satellite, the model of the ballbot robot stood out due to its particular shape and dynamics. Using a single ball as its propulsion system, it can spontaneously tilt in any direction whilst rotating about its own axis. One of the key aspects that make the ballbot interesting is that it does not need to yaw in order to change direction, this means that the complexity of it's reorientation is reduced compared to a multi-wheeled robot. The typical ballbot consists of three main parts: the body, which contains the control and power systems, the propulsion system which depending on the design consist of three omni-wheels placed at $120°$ or four omni-wheels at $90°$ angles which actuate the final part which is the ball. In space, the gravitational effects on a ballbot can be neglected and therefore it will remain stable about any position it is inserted in. In principle then, the system is free to reorient the wheel in any direction. It follows that if the mass of the wheel is much larger than the

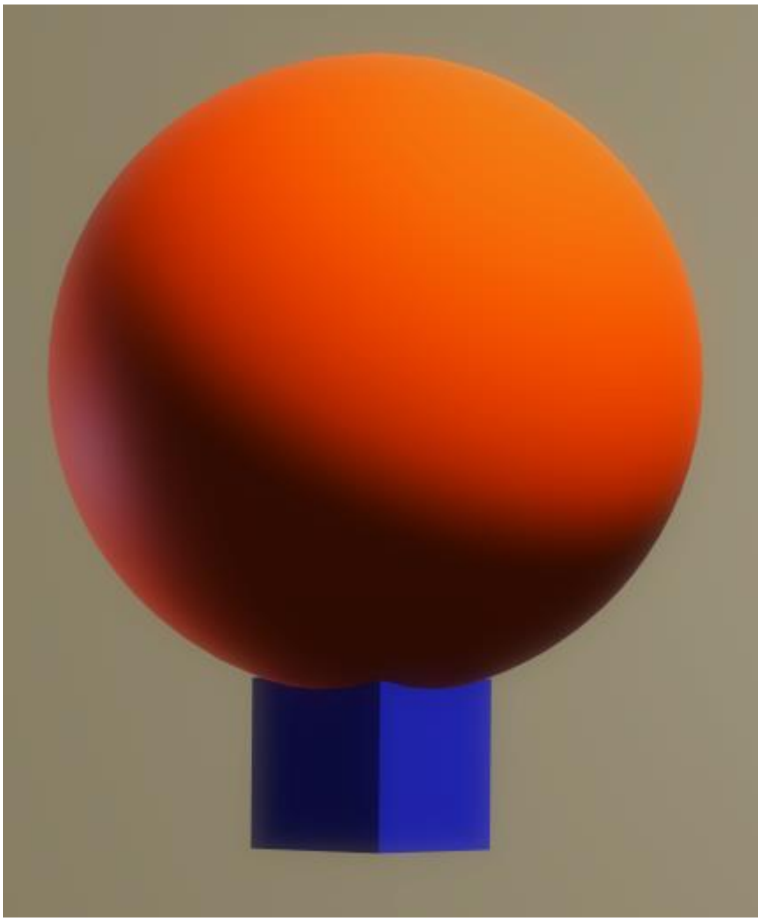

Figure 27 Ballbot satellite 3D shape

mass of the body, the actuation will reorient the body rather than the wheel. Therefore, inverting the relationship between the ballbot's and the ballbot's body resulted in a satellite with a spherical tank and cuboid bus which moves on the surface of the satellite as shown in the figure 21.

This satellite design has several advantages, foremost, that it can reorient itself to any direction without investing as much energy and without inducing fuel slosh that would follow from the reorientation maneuver. The main operating mode will have the satellite in a sun-pointing attitude. This is because, in case cryogenic fuels are used, thermal leakage and boiloff become major concerns [18] and to avoid this it has been contemplated that the design includes deployable sunshields which are deployed from the satellite bus subsequent to insertion into orbit as shown in figure 22. For this instance, the satellite is considered to carry a non-cryogenic fuel, in this case Hydrazine N_2H_4, which was chosen due to its similar density to water and ubiquitous use in the industry.

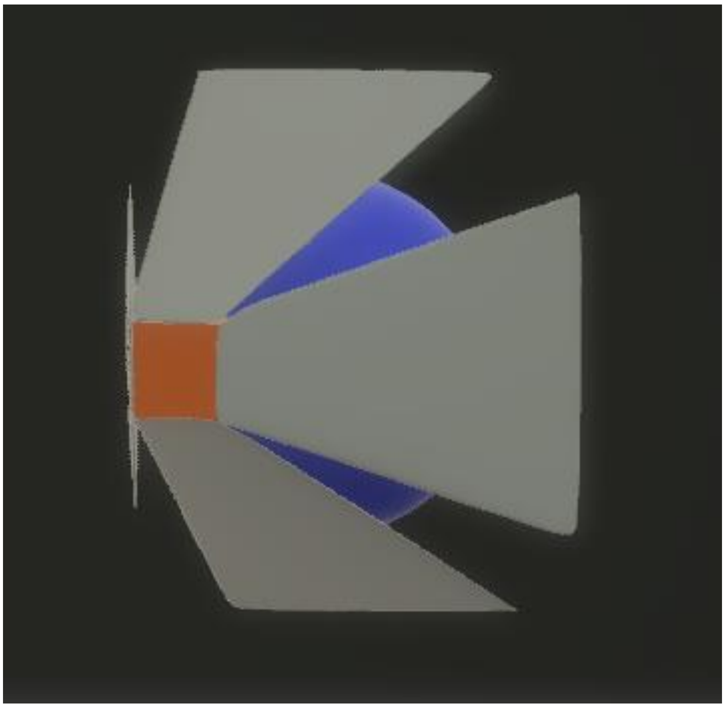

Figure 28 Ballbot satellite with sunshields deployed

4.2. Design Parameters and Simulation

The approach taken for finding the design parameters was taken after considering the possible launchers for the satellite. The Arianne 5 with roughly $5.4\ \mathrm{m}$ wide fairing was deemed sufficient. The model used to simulate the slosh dynamics is the pendulum analogy with two decoupled pendulums each affected by a lateral component of the torque vector affecting the satellite, $T_{cx} + T_{dx}, T_{cy} + T_{dy}$ respectively.

Table 7 Satellite dimensions & parameters

Parameter	Value
Total Mass	6000 kg
Mass of bus	375 kg
Mass of Tank	5625 kg
Filled fuel weight	4726 kg
Fuel density ρ	1.0036 g/cu cm
Fuel fill (for simulation)	85%
Length along longitudinal axis	6 m
Length along horizontal axis	5 m
Diameter of tank	5 m
Side length of bus	1 m

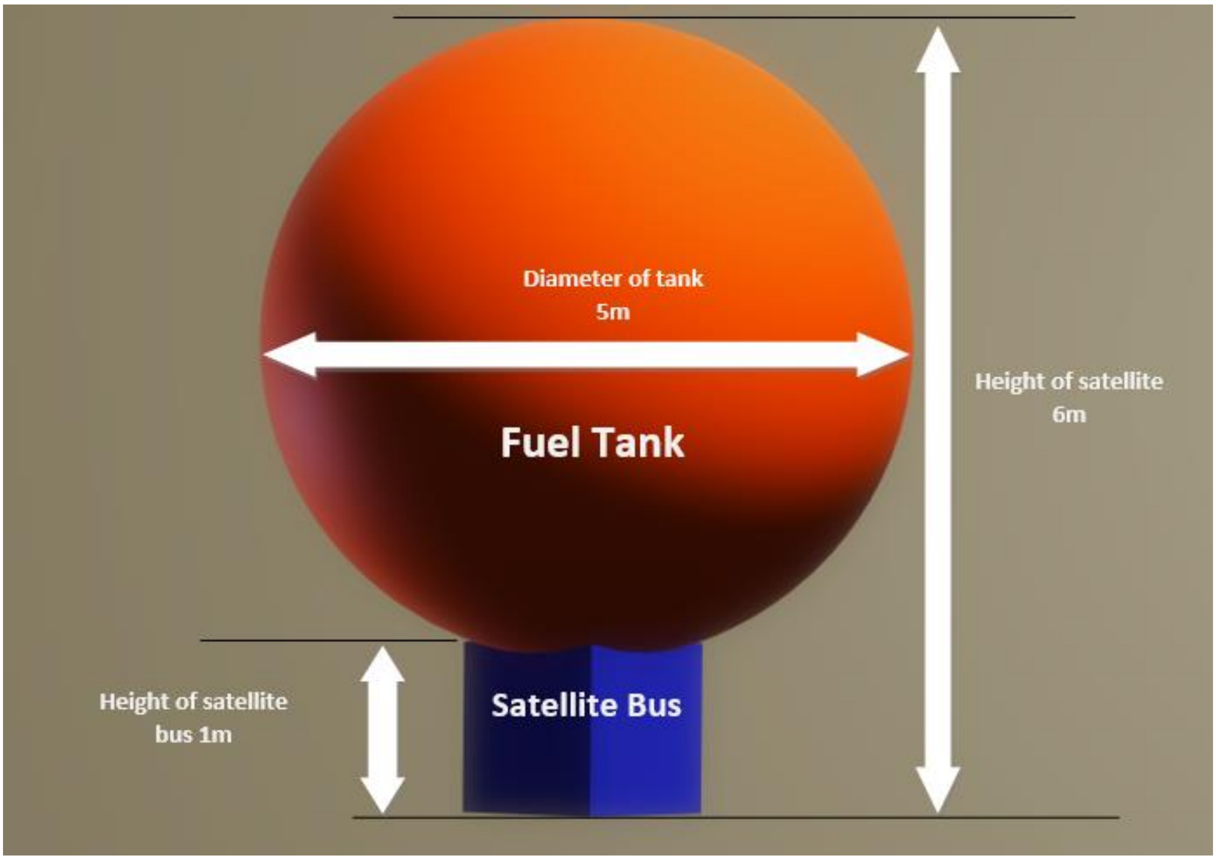

Figure 29 Satellite dimensions

4.2.1. Moment of Inertia Calculation

In order to simulate the satellite in orbit it is crucial to have a moment of inertia figure. The filled mass of $6000\ \mathrm{kg}$, was determined according to the launcher's performance figures for GEO orbit insertion. Considering that the tank will be roughly 15 times more massive than the satellite bus we have:

- The mass of the tank, $m_t = 5625\ \mathrm{kg}$
- The mass of the cuboid bus, $m_c = 375\ \mathrm{kg}$

The moment of inertia tensor is obtained using the parallel axis theorem after obtaining the moment of inertia of the cube and the sphere separately. For the tank, we can use the equation for the moment of inertia of the sphere:

$$I_s = \frac{2}{5} m_s r^2$$

$$\therefore I_s = 14062.5$$

Where r is the radius, $2.5\ \mathrm{m}$.

For the satellite bus, the moment of inertia is given by:

$$I_c = \frac{1}{6} m_c l^2$$

$$\therefore I_c = 15.625$$

Where l is the side length of the cube, $1\ \mathrm{m}$.

Finally, to apply the parallel axis theorem, the combined center of mass is required. The center of mass of the cube is at $0.5\ \mathrm{m}$, the center of mass of the sphere is at $2.5\ \mathrm{m}$. The combined center of mass is given by:

$$cm_t = \frac{cm_c\, m_c + cm_s\, m_s}{m_t}$$

$$\therefore cm = \frac{0.5 \times 375 + 2.5 \times 5625}{6000} = 200.671$$

The resulting inertia tensor $\mathcal{J}$:

$$\begin{bmatrix} 200.671 & 0 & 0 \\ 0 & 200.671 & 0 \\ 0 & 0 & 200.671 \end{bmatrix}$$

The moment of inertia for the fluid in the satellite tank is the moment of inertia of a pendulum (due to the model used) and is given by:

$$I_p = m_f L^2 = 564$$

Where m_f is the mass of the fluid and L is the length of the pendulum arm.

4.2.2. Orbit Parameters

The decision diving the determination of the selection of the orbit was the compromise between the space environment and disturbances with the proximity to the Earth so that it is accessible to the largest quantity of the potential users. It was found that an altitude of $500\ \mathrm{km}$ was sufficient to avoid significant atmospheric drag effects whilst being available to large number of missions that might make use of a fuel depot. The following table lays out the parameters for the orbit that was used to simulate the satellite.

Table 8 Orbital Parameters

Parameter	**Value**
Semi-Major Axis (m)	6791000
Eccentricity (e)	0.00058568
Inclination (deg)	51.644
RAAN (deg)	244
Argument of Periapsis (deg)	28
True Anomaly (deg)	203

4.3. Simulation of Model

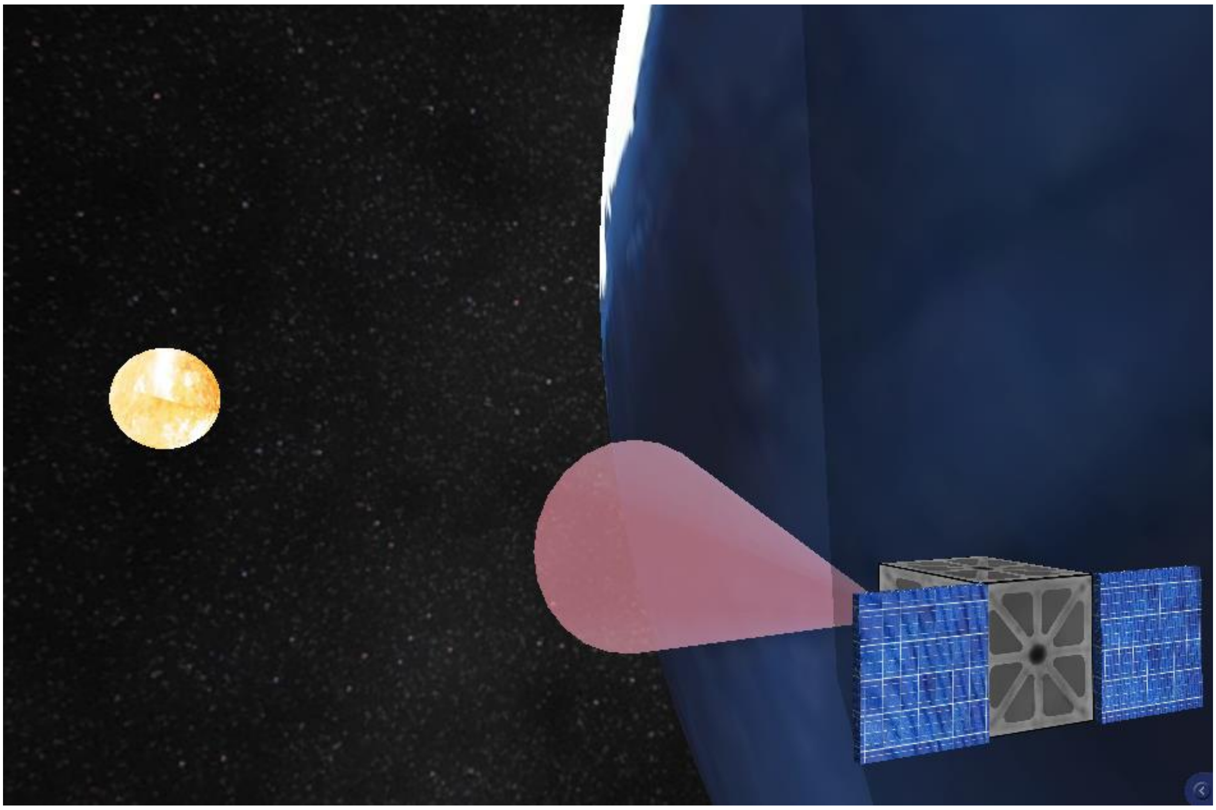

Figure 30 Satellite in sun-pointing mode

The model of the satellite with parameters provided in section 4.2 is carried out using MATLAB Simulink, using the Aerospace toolbox, Control Systems toolbox, and 3D-Animation toolbox.

Figure 31 Simulink Satellite Simulation Setup

The setup is divided into 3 main sections, the *Flight Control* section, in it the *Attitude Profile* block receives the feedback signal from the output and computes the minimum rotation quaternion or *reference quaternion* $\bar{q}_{ref}$, which is fed into the attitude controller block. The attitude profile can be selected from the *Attitude Profile* block. The primary alignment vector is $[0\ 0\ 1]$ in the body frame and the secondary is $[1\ 0\ 0]$. The attitude controller block houses the attitude controller script block as well as the slosh filter, a notch-filter attached to the controller.

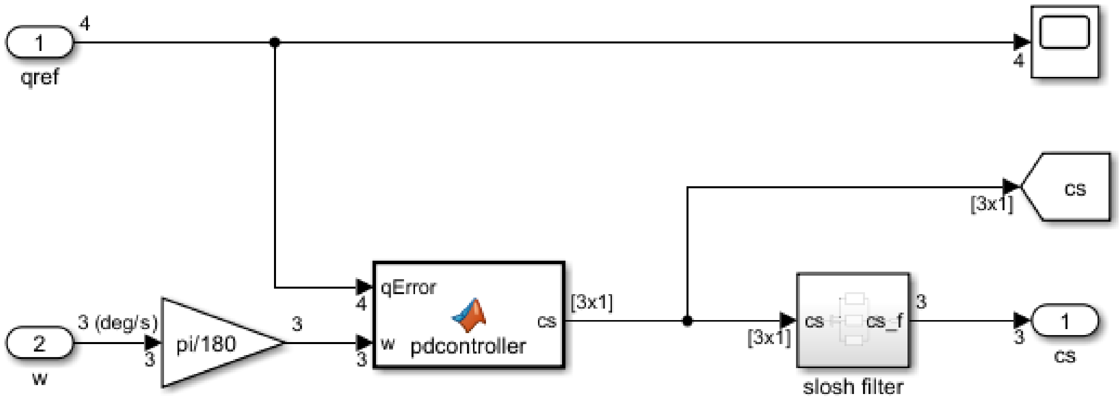

Figure 32 The Attitude Controller Block

The body rates are also fed in the *Attitude Controller* block to the attitude controller script-block. The script for the attitude control follows from the expressions found in section 2.5.3.

Figure 33 The control law is applied to the error quaternion

The gains, k_p and k_d where found experimentally so that the satellite is stabilized, as no design requirements have been imposed.

The output is passed through the *Slosh Filter* block Inside, the signal is split using a demux into it’s three torque components and input into the transfer function blocks. The tuning of this filter is explained in section 4.3.1.

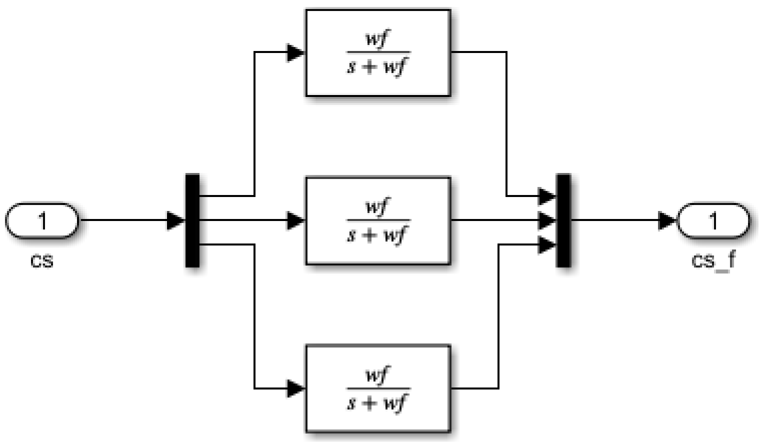

Figure 34 The slosh filter of the attitude controller

The next section in the Spacecraft Dynamics Model is the *Spacecraft Plant.* Here, a model of the spacecraft dynamics is contained, along with the tank with the slosh. The The signal from the *Flight Control* block enters a demux block where the signals control signals are indexed in an adequate way to be vector-added to the torques from the slosh tank. The *Tank Slosh* block contains the tank slosh model which received a feedback input from the angular acceleration output. It is fed into a demux which bundles the lateral components together and separates them from the vertical torque component. The lateral torque signal is fed into the *Tank Sloshing* block which contains a script with the equations for the pendulums.

Figure 35 Script for tank sloshing using pendulum model

The output of the block is a signal with 4 components, the accelerations and the rates of the pendulums. The signal is integrated and fedback into the block while another branch is fed into the *storque* which converts the *Tank Sloshing* block output into torque by multiplying them with the moment of inertia computed in section 4.2.2. The output of the *Tank Slosh* block is fed into the control signal *cs* block where the control signal is added to the slosh torque and bundled together with the third output of the controller. Finally, this signal is fed into the Spacecraft Dynamics block which contains the 6-DoF model of the spacecraft. In this block the mass, moment of inertia tensor, orbit and initial conditions are all specified. The outputs are fed into final sections which are the *Outputs* and *Observation* sections which contain the scopes for observing the behaviour of the satellite as well as the animation block which displays an animation of the satellite in orbit according to the simulation.

Note: The simulation uses the spherical harmonics gravitational potential model *EGM2008*.

4.3.1. Simulation of Slosh Model

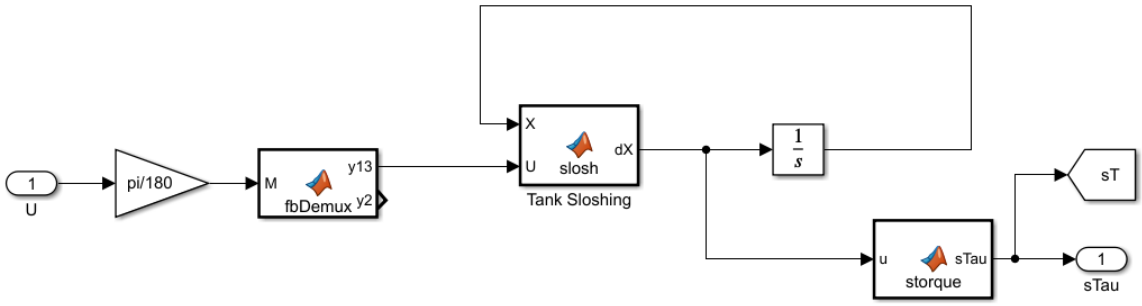

Figure 36 *Tank Slosh* block interior

The slosh model was developed using the concepts from section 3.2. Essentially, a model is created by bundling two pendulums into a single system. The Equation of the pendulum is:

$$\ddot{\theta} = T - \frac{g}{L}\sin\theta$$

As shown in figure 34, the function for the system returns a signal with 4 components. Since the tank has a fill ratio of 85%, the pendulum length L is assumed to be equal to the distance between the tank wall and the liquid surface which is 15% of the radius. And the mass is 85% of the maximum fill capacity. The simulation with the initial conditions consisting of 0.1 radians for the first pendulum position and 0.2 radians for the second pendulum position. The results are as follows:

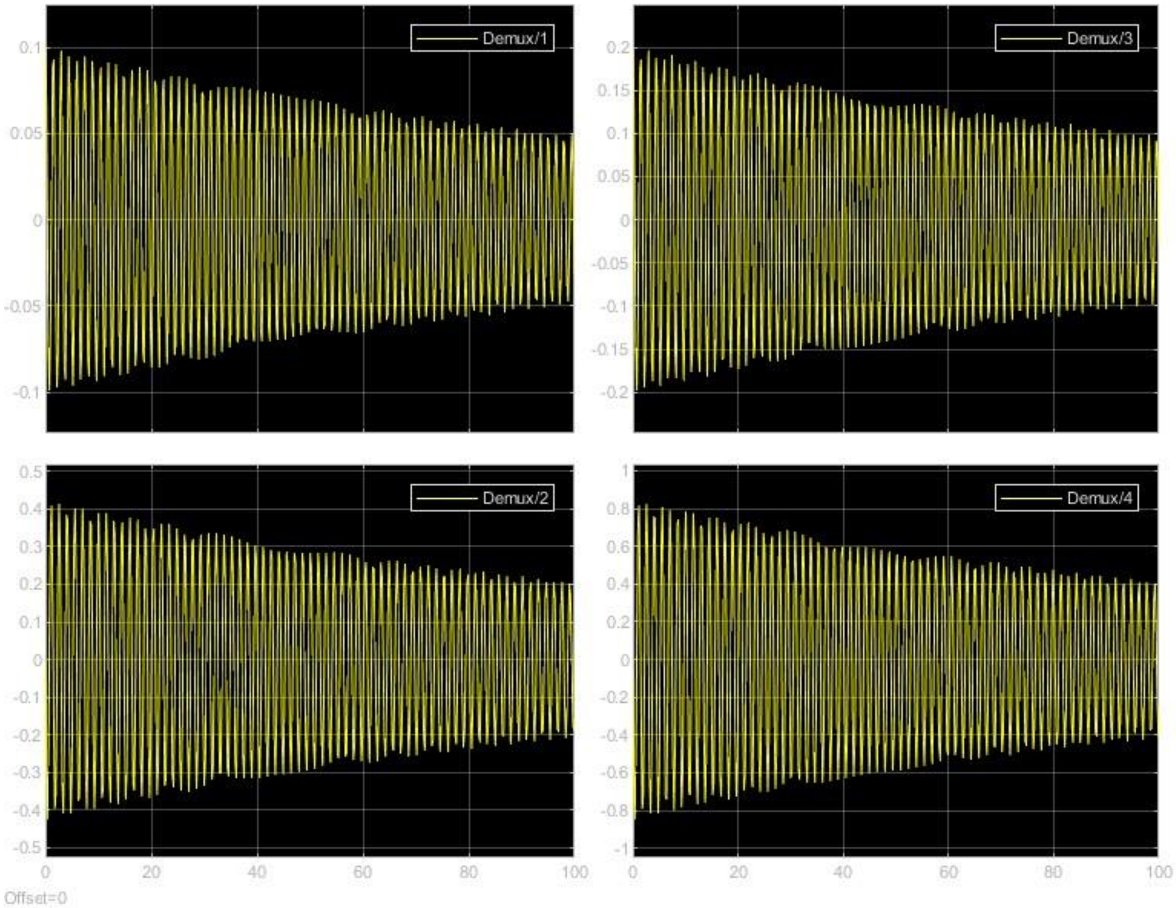

Figure 37 Pendulum mass position as a function of time where (from left to right, and to top to bottom): Pendulum 1 position, pendulum 1 velocity, pendulum 2 position, pendulum 2 velocity.

- Figure 35 is the damped oscillatory motion of the mass as predicted by the equations.
- Figure 36 is the Bode plot of the pendulum system which reveals a peak in the frequency response ($4.19\ \mathrm{rad/s}$) at which the phase margin is reached, and the system becomes unstable as shown.

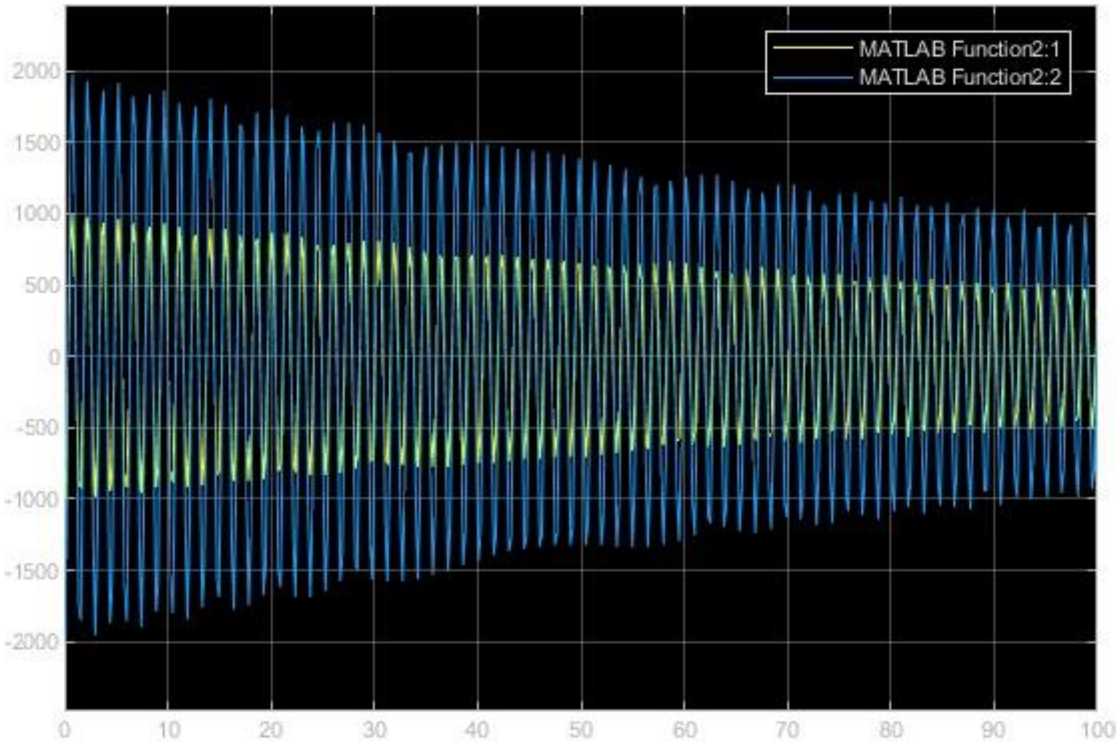

Figure 38 The torques from the pendulums are the output signal of the block

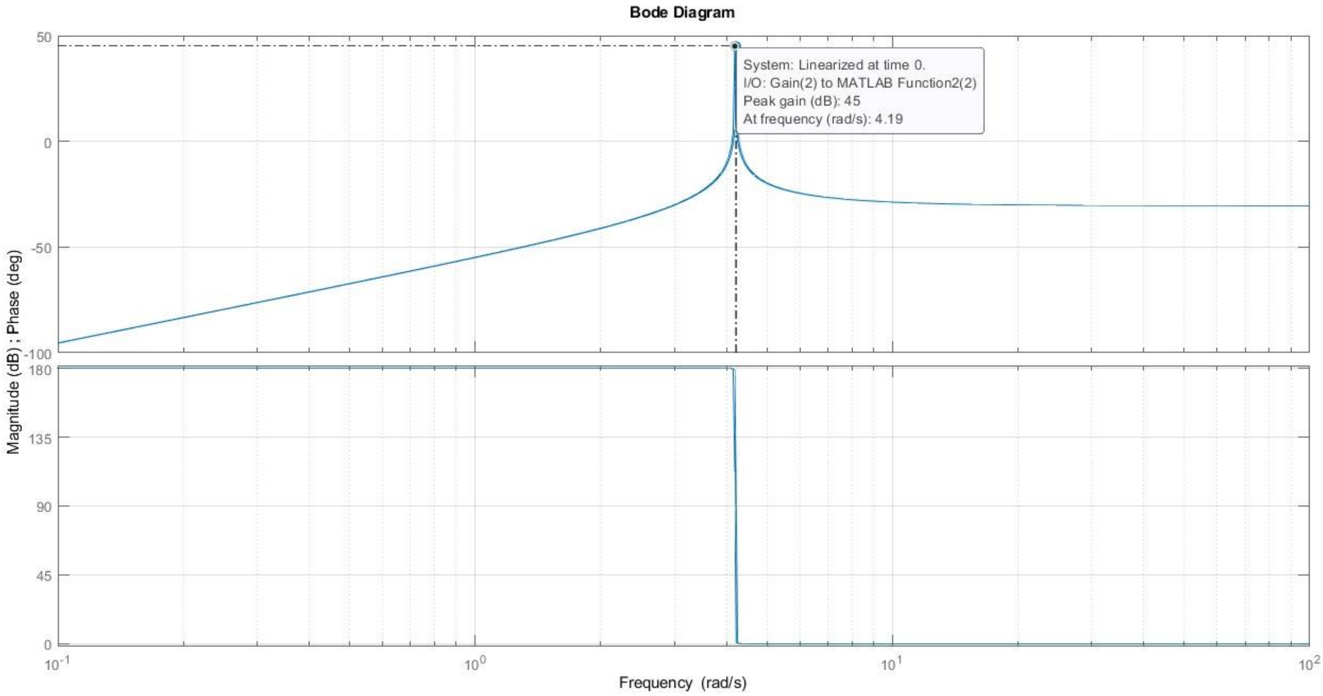

Figure 39 The frequency response plot

4.3.2. Simulation of Model Without Slosh

Assuming the liquid does not slosh within the tank, but the mass is the same, we simulate the satellite in the sun-tracking mode with an initial quaternion vector of $[0\ 1\ 0\ 0]$. The simulation reveals the following:

- The satellite is capable of reorienting itself to point at the sun during the entire orbit.
- The satellite is stable and maintains its orientation on all three-axes.
- The satellite does not require a notch filter to be stable.

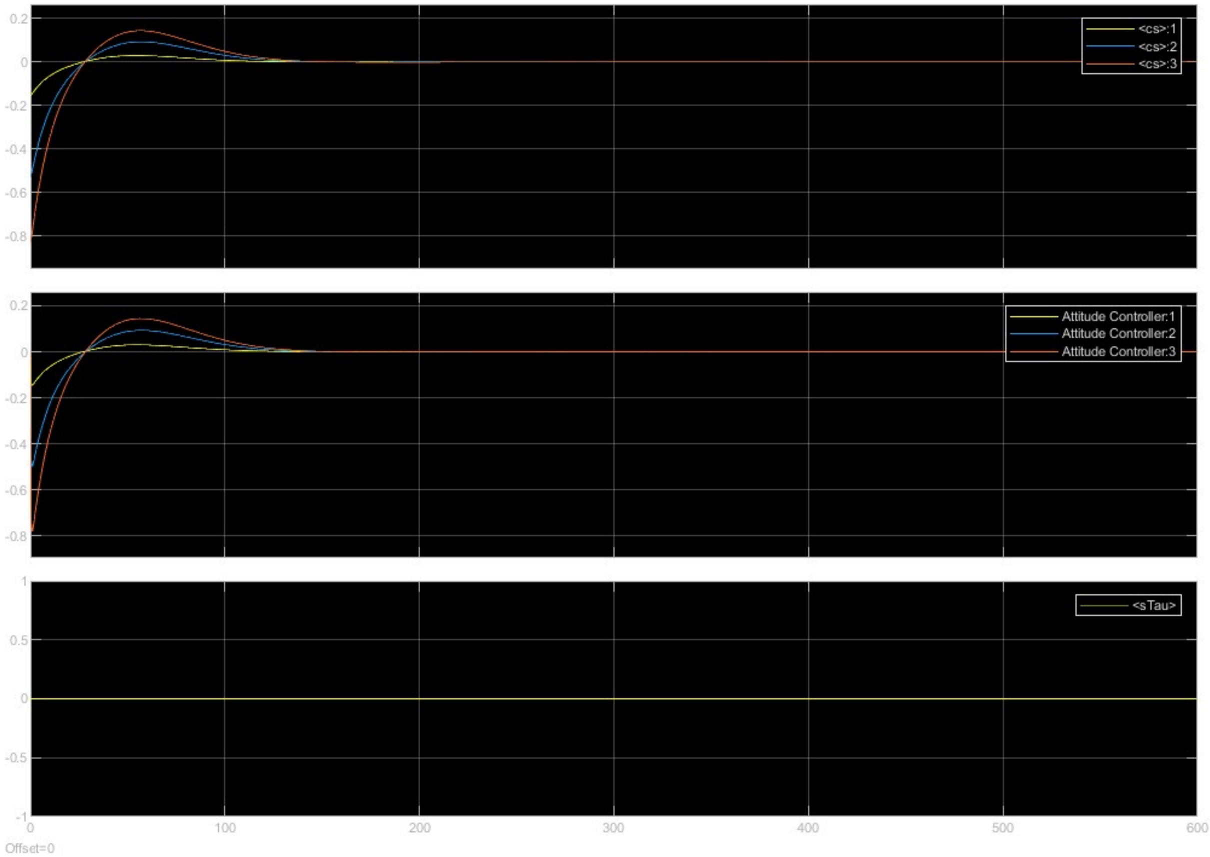

Figure 41 From top to bottom: 1) The control signal, 2) The control signal with slosh torque, 3) Slosh torque

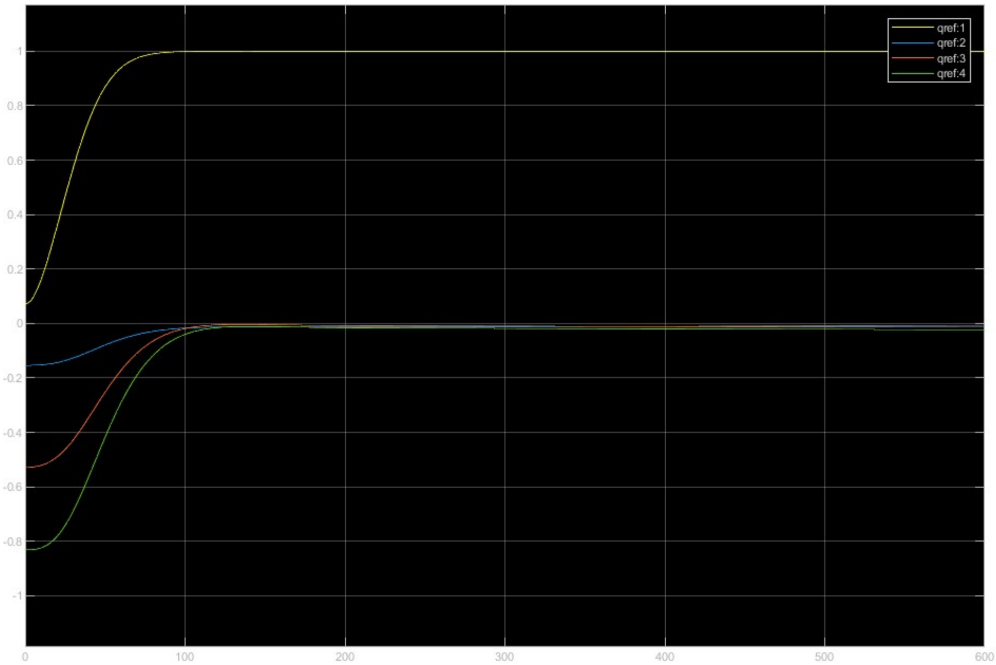

Figure 40 The reference quaternion plot

4.3.3. Simulation of Model with Slosh

Using the same initial conditions as with the simulation with no slosh, the simulation is run in two modes which the satellite will likely find itself being used: Nadir pointing and Sun pointing.

4.3.3.1. Simulation of Model with Slosh in Nadir Pointing Mode

The simulation with tank sloshing in nadir pointing mode reveals the following:

- It is necessary to use a slosh-filter in order to stabilize the satellite. The effect of the notch filter can be assessed using a bode plot with linear analysis points in the *Attitude Controller* block. The Bode reveals that the frequency response peak has been removed and the system is stable for high gains as shown in figure 46.
- With the slosh-filter, the satellite successfully performs a reorientation maneuver to point at nadir.
- Once pointing at nadir, the satellite is stable on all three axes.

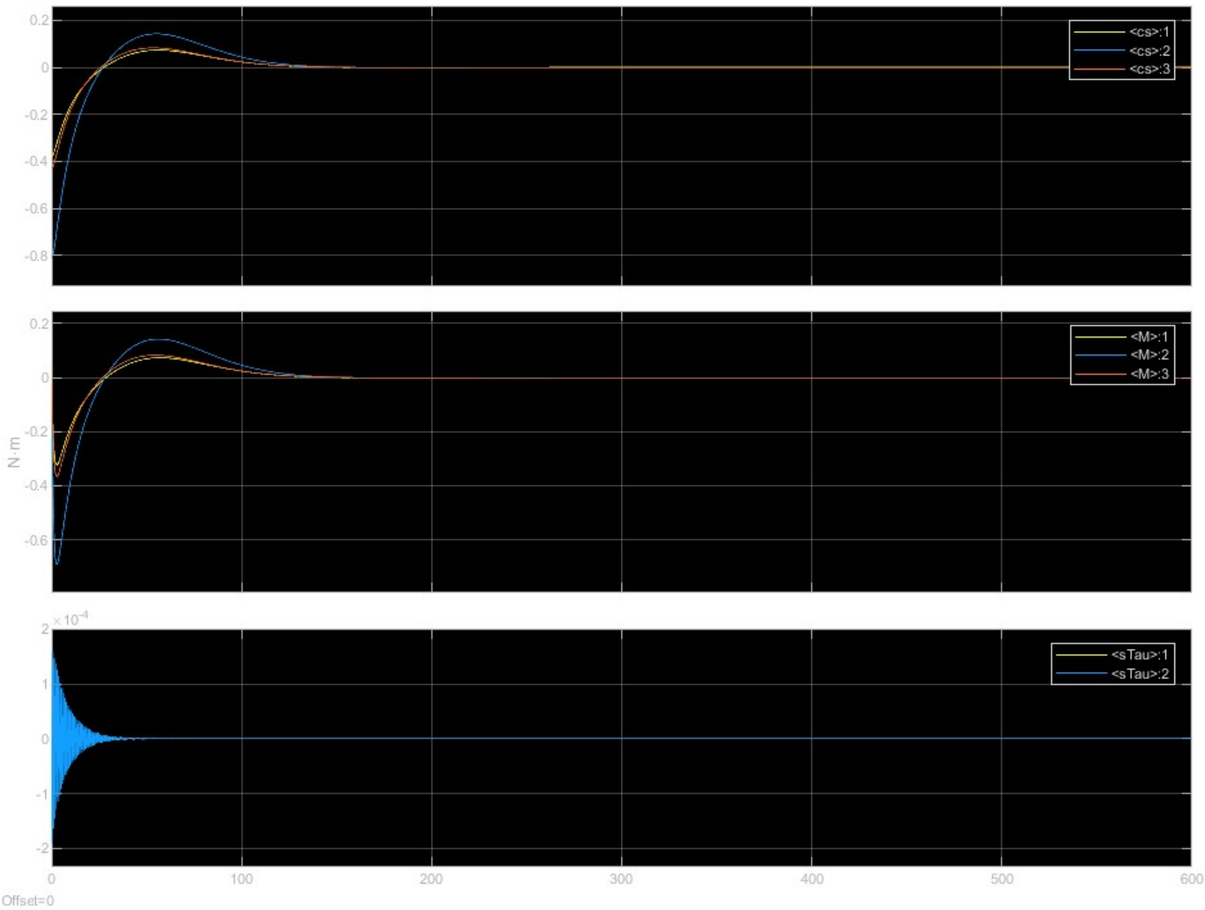

Figure 42 From top to bottom: 1) The control signal, 2) The control signal with slosh torque, 3) Slosh torque

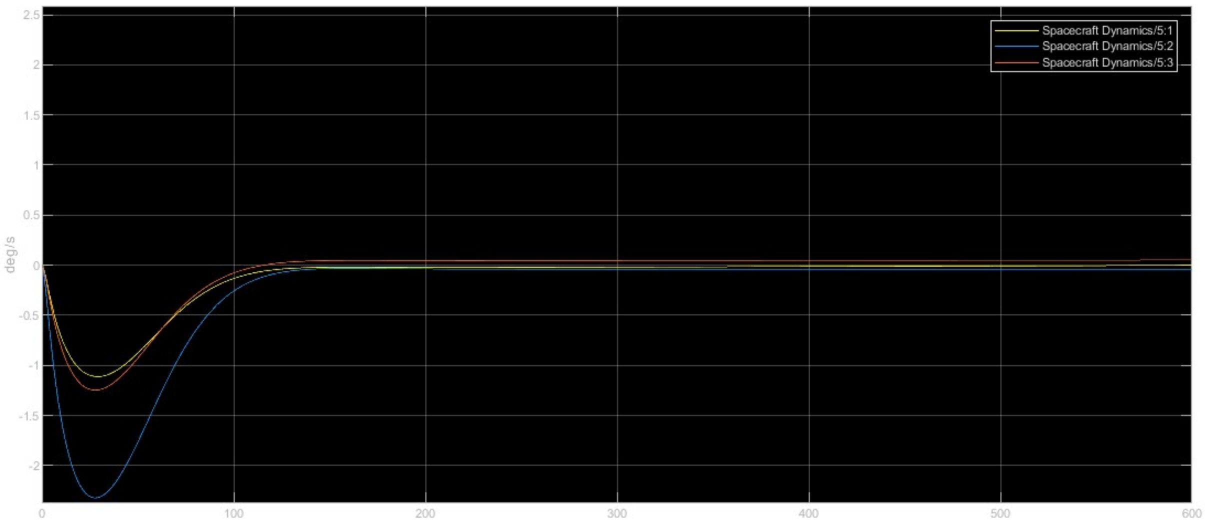

Figure 43 Angular rates of nadir pointing mode

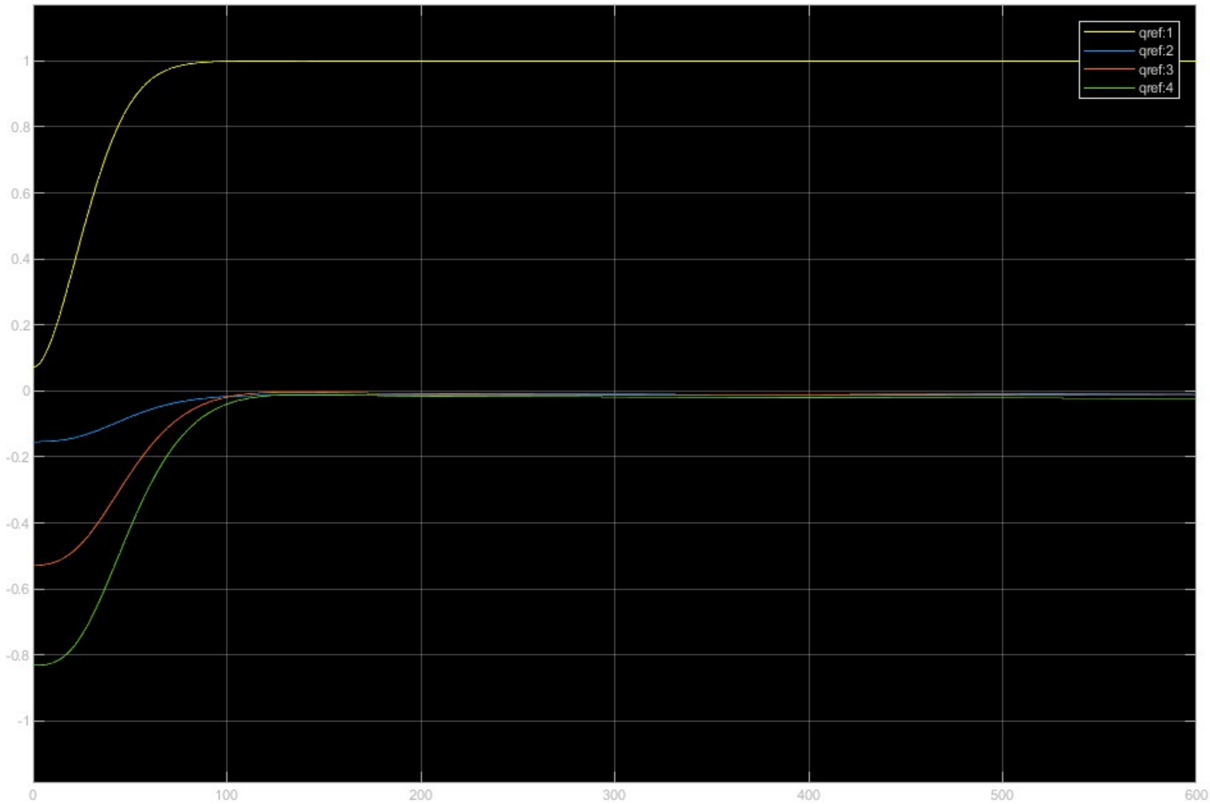

Figure 44 Reference quaternion with sloshing in nadir pointing mode

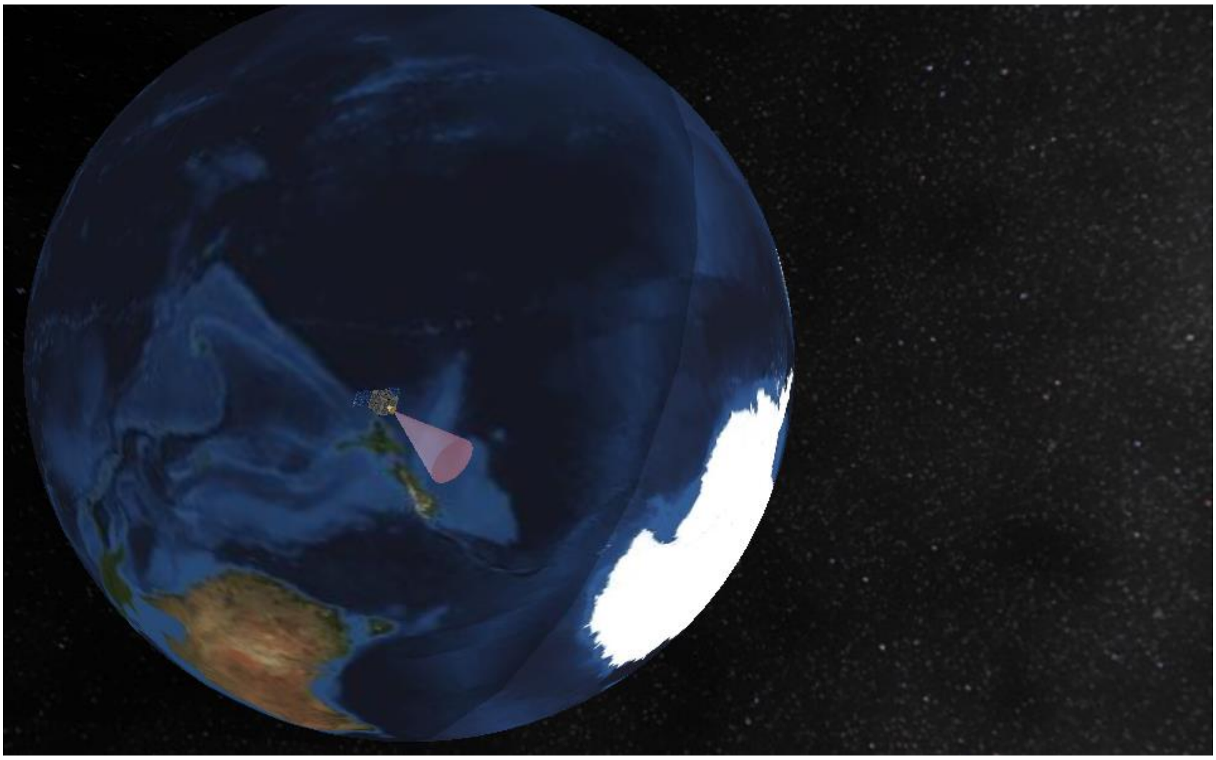

Figure 45 Nadir pointing Satellite a t = 10s

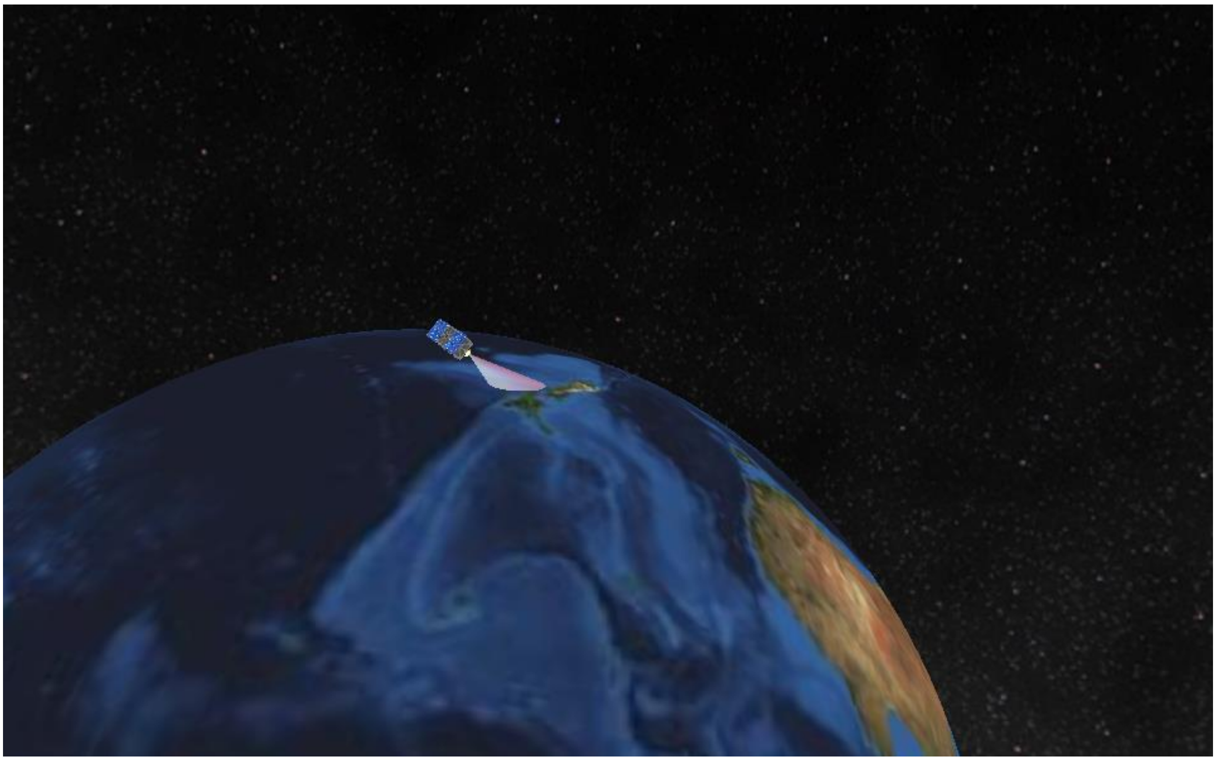

Figure 46 Nadir pointing satellite at t = 45s

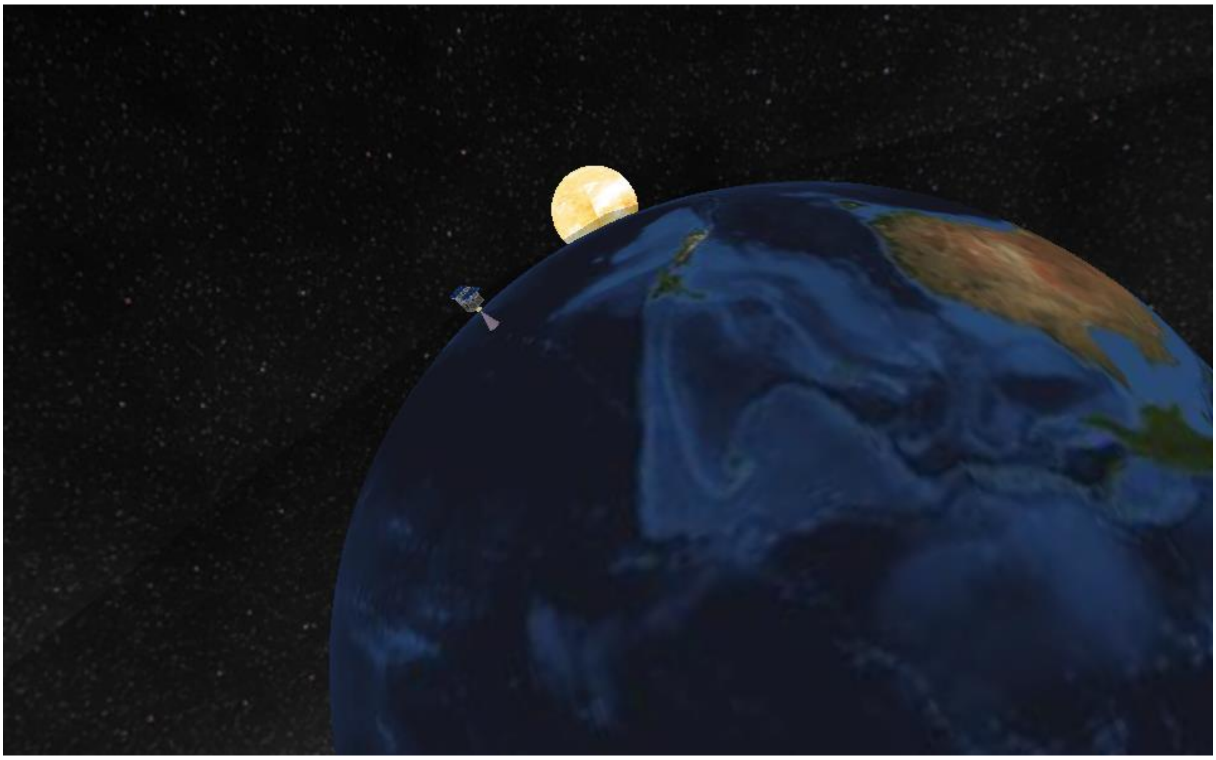

Figure 47 Nadir pointing satellite at t = 300s

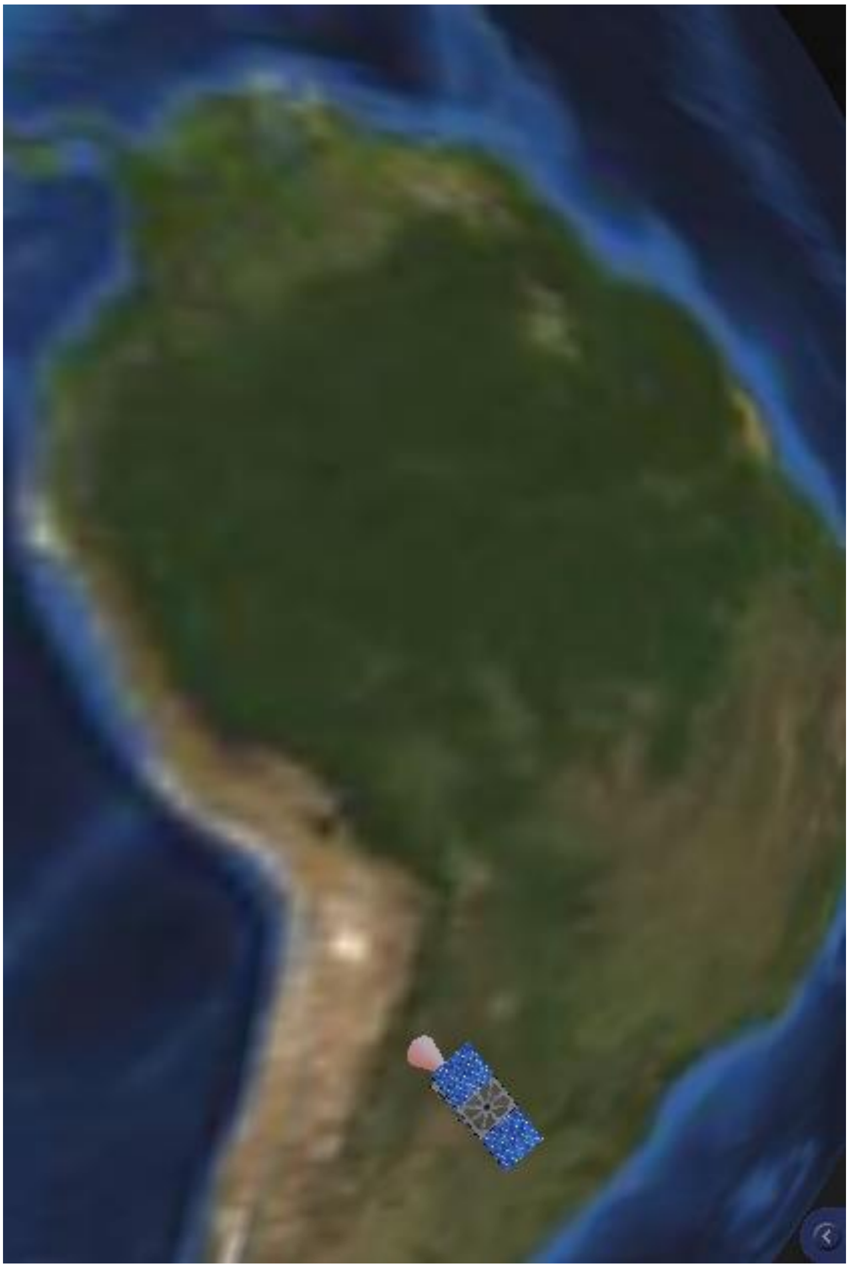

Figure 48 Satellite in nadir pointing mode at t = 3600s

4.3.3.2. Simulation of Model with Slosh in Sun Pointing Mode

Similarly, in sun-pointing mode the simulation with tank sloshing reveals the following:

- It is necessary to use a slosh-filter in order to stabilize the satellite.
- With the slosh-filter, the satellite successfully performs a reorientation maneuver to point at the sun.
- Once pointing at sun, the satellite is stable on all three axes and tracks the sun for the duration of the orbit.

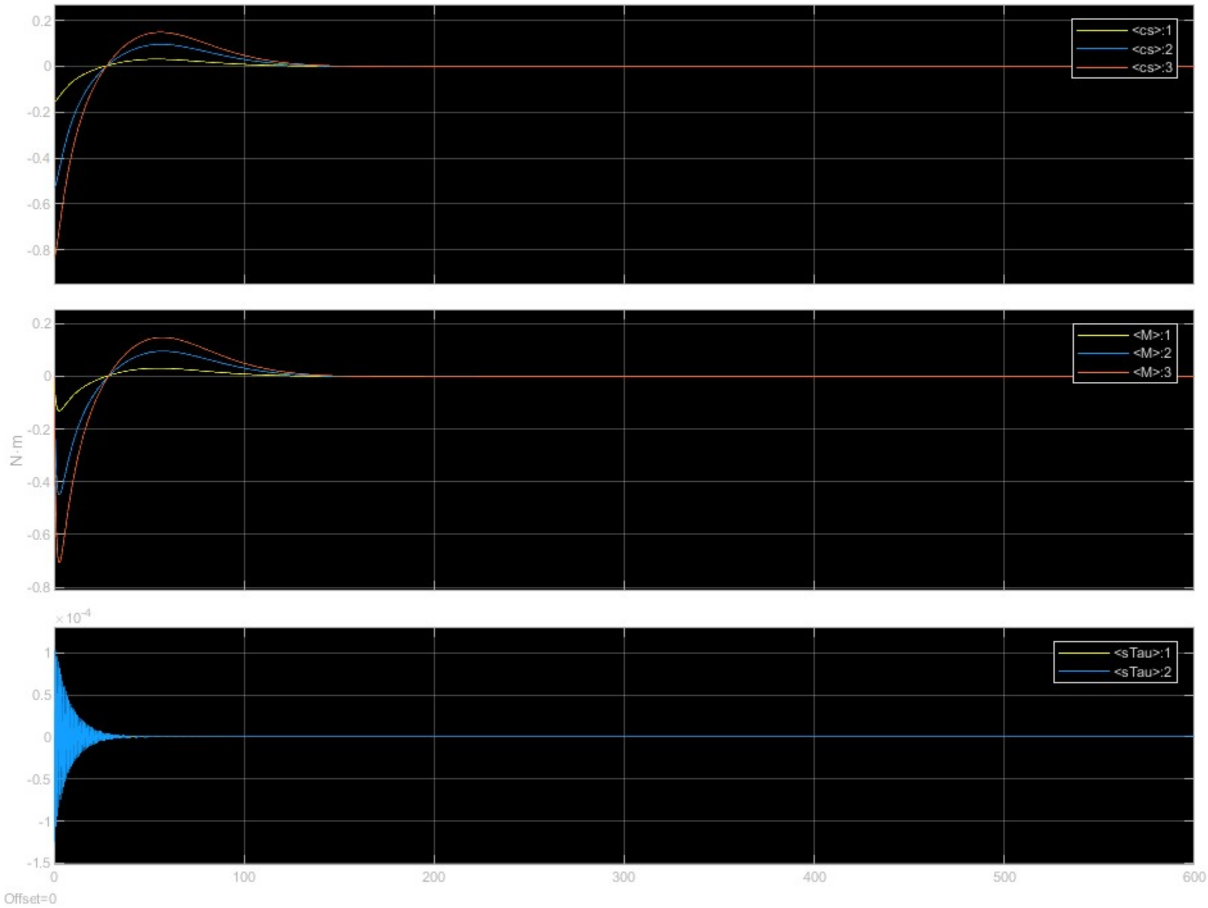

Figure 49 From top to bottom: 1) The control signal, 2) The control signal with slosh torque, 3) Slosh torque

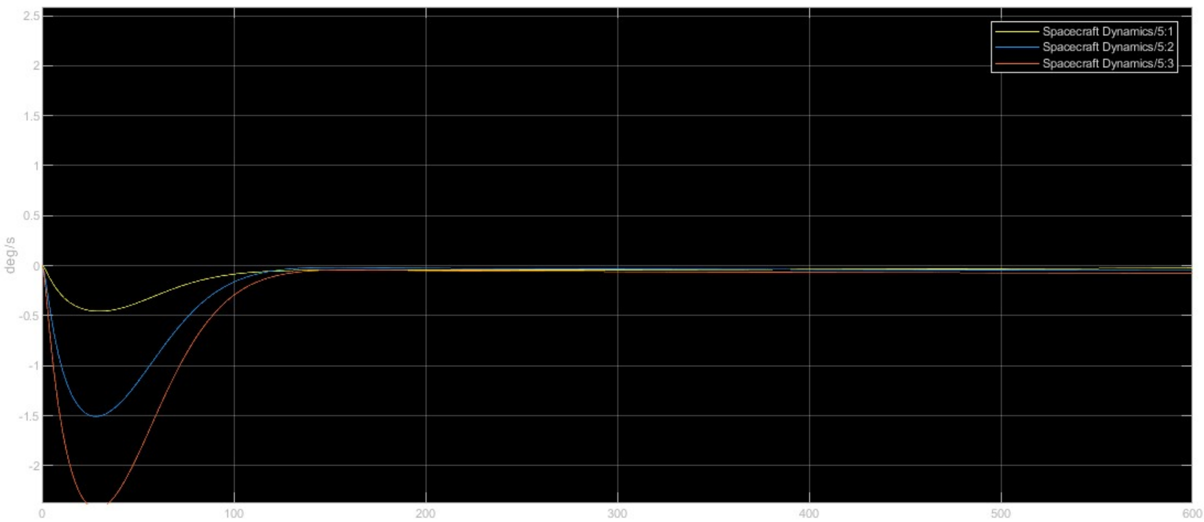

Figure 50 Angular rates for sun pointing mode with sloshing

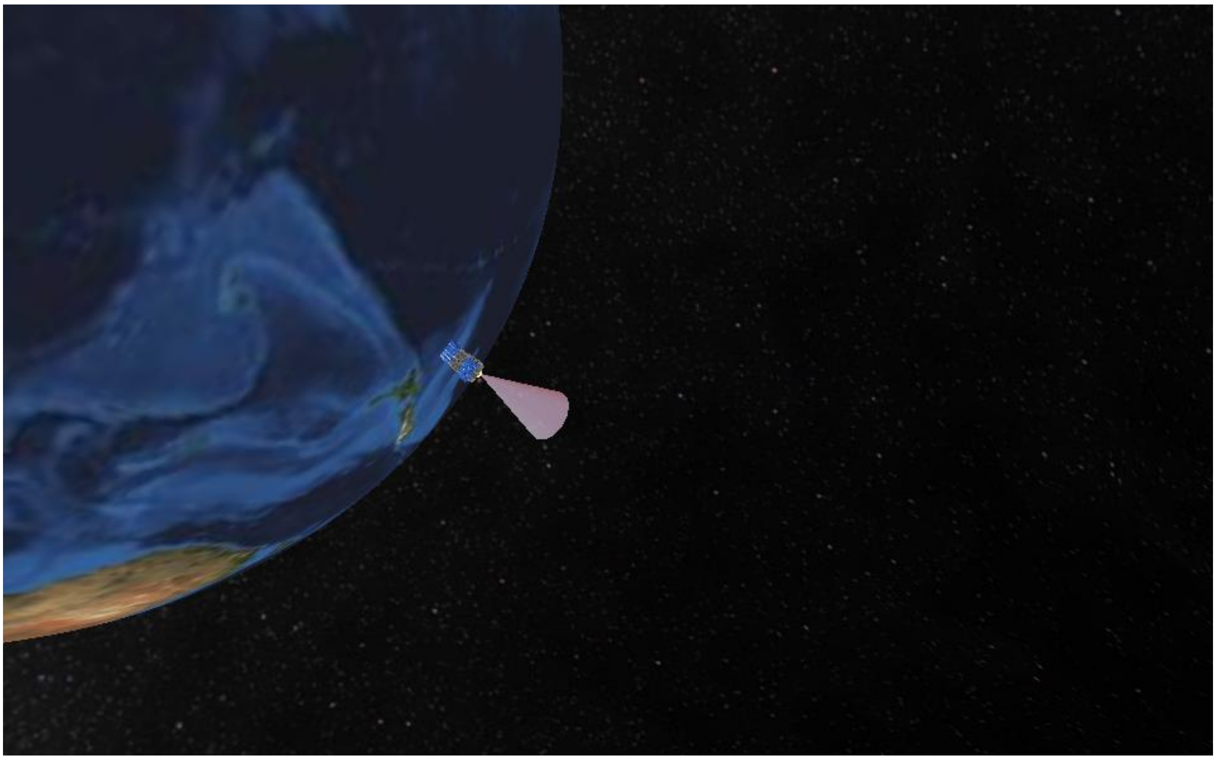

Figure 51 Sun-pointing satellite at T=10s

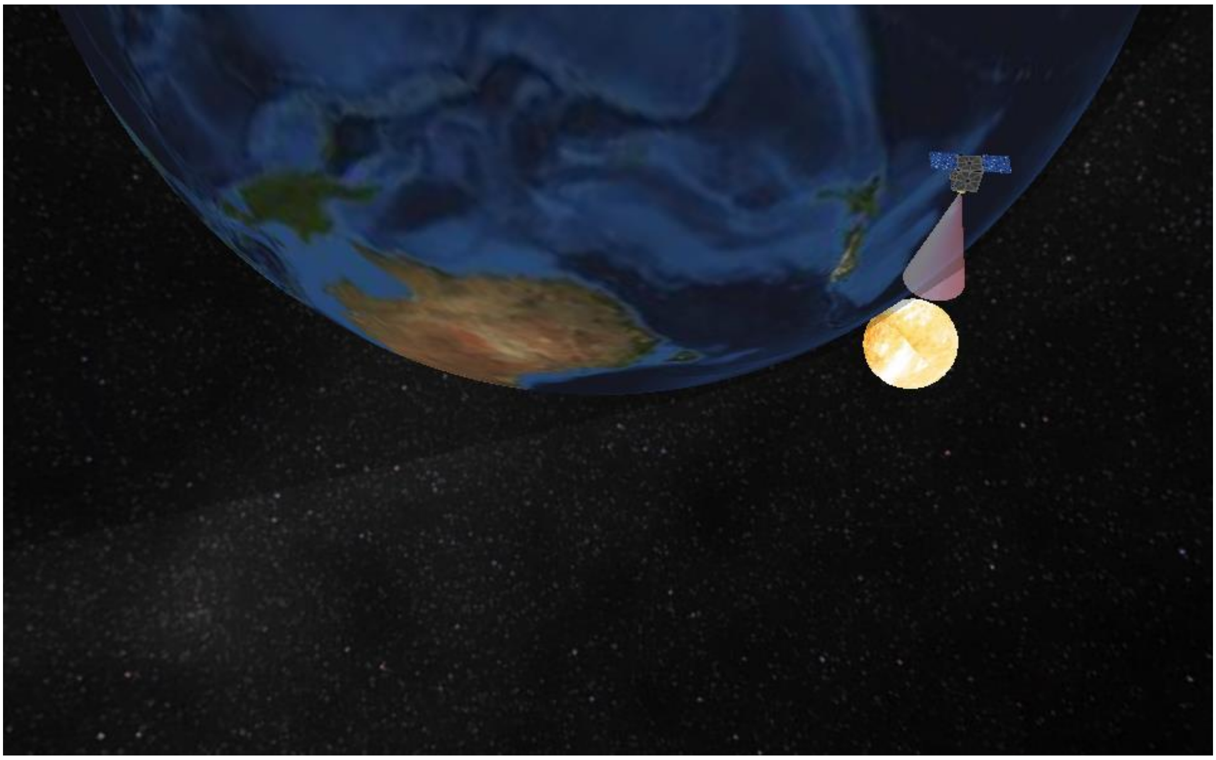

Figure 52 Sun-pointing satellite at T = 45s

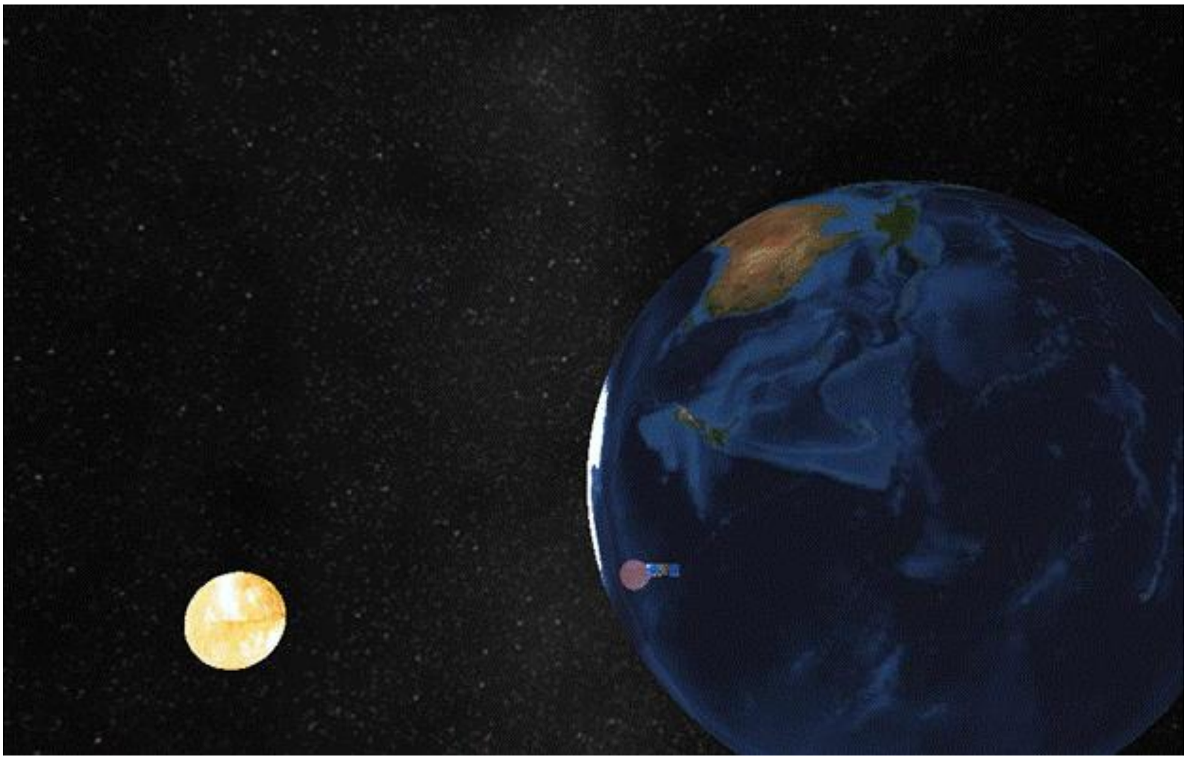

Figure 53 Sun-pointing satellite at t = 300s

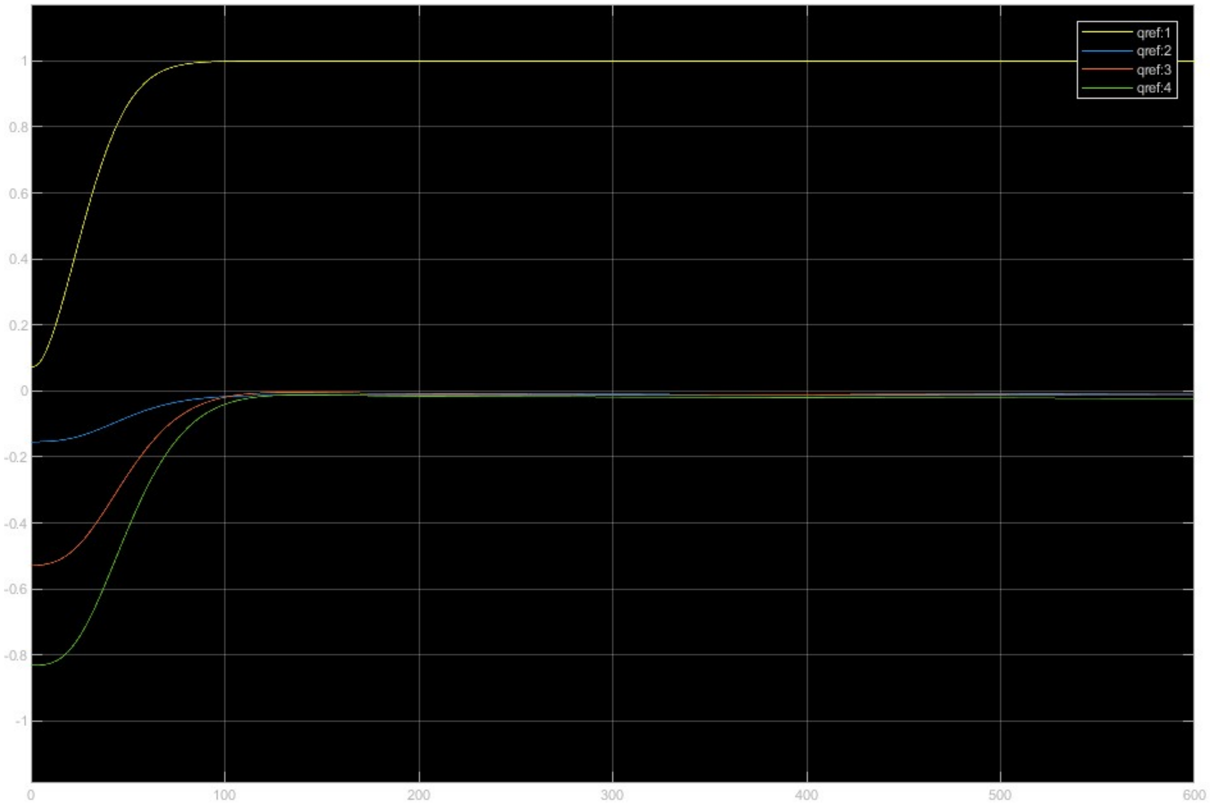

Figure 54 The reference quaternion in sun pointing mode with sloshing

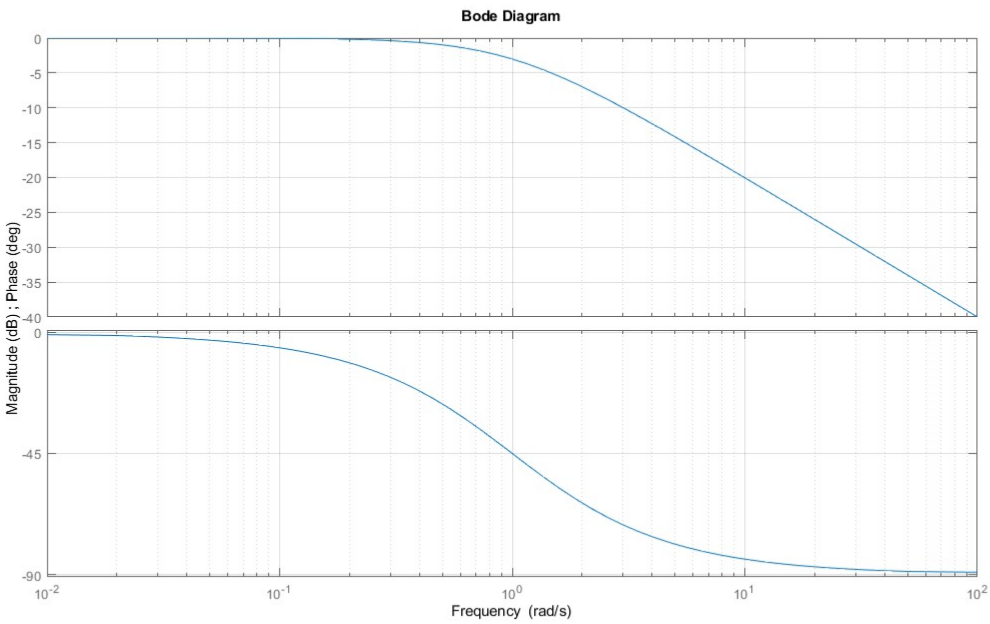

Figure 55 Frequency response with slosh filter implemented

4.3.4. Sun-Tracking Using the Ballbot-Dynamics

In this section, the dynamics of tracking system is laid out using the ballbot dynamics as a reference model. The derivation of the equations is carried out and a simulation in Mathematica demonstrates how the model can be used to track a target.

4.3.4.1. Ballbot Dynamics Overview

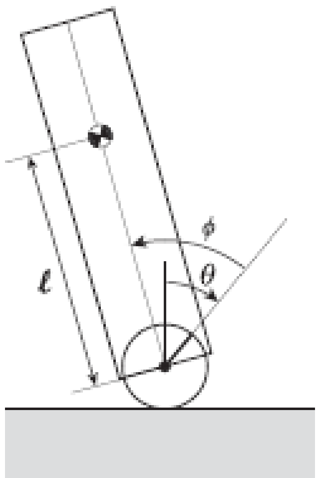

Figure 56 Ballbot showing angles and coordinates

A planar model is developed for the ballbot in the xy plane formulation which is identical to the yz plane using the Lagrangian formulation, where θ is the angular position of the ball from the reference vector which lies on the vertical axis. ψ is the angular position of the body with respect to the ball's heading. Also, the following assumptions are made:

- No slippage: there is no slippage between the ball and the ground or between the ball and the torque wheels (actuators). Additionally, it is assumed that the torque applied is within a range where slippage will not occur.
- No deformation: it is assumed that the ball and actuators do not deform during the operation of the robot.
- Rapid motor dynamics: the responses of the motor are assumed to be much faster than the controller dynamics and therefore the motor torques can be assumed to be the inputs of the system.
- Ball movement constraints: it is assumed that the ball can only move on the horizontal plane. It cannot move vertically. Additionally, the robot will not traverse terrain with steep inclines.

Due to the size and complexity of the equations, Mathematica was used to obtain the differential equations which are implemented in the simulation.

4.3.4.2. Sun-Tracking Simulation

The simulation for sun-tracking is done using Mathematica. It is implemented on the planar model and the signal is tracked for a fixed angular position with respect to the satellite using an optimal controller (LQR).

Sun-Tracking Using Ballbot Dynamics

The parameters for the system:

In[1]:=
```
pars = {m_B → 625, m_b → 5375, r_b → 2.5, 𝓘_b → 22187.5, 𝓘_B → 312.5, 𝓘_Bxy → 0.092, ℓ → 3, g → 0};
```

The equations of motion used for computing the state space:

In[5]:=
```
eqns = {-g ℓ Sin[θ[t] + ϕ[t]] m_B + ℓ Sin[θ[t] + ϕ[t]] m_B r_b (θ′[t]^2 + θ′[t] ϕ′[t]) +
     (1 / 2) (2 m_b r_b^2 θ″[t] + 2 𝓘_b θ″[t]) + 𝓘_B (θ″[t] + ϕ″[t]) +
     (1 / 2) m_B (-2 ℓ Sin[θ[t] + ϕ[t]] r_b (θ′[t] + ϕ′[t]) (2 θ′[t] + ϕ′[t]) +
        8 ℓ^2 θ″[t] + 2 r_b^2 θ″[t] + 2 ℓ Cos[θ[t] + ϕ[t]] r_b (2 θ″[t] + ϕ″[t])) == 𝒯_1[t],
   -g ℓ Sin[θ[t] + ϕ[t]] m_B - ℓ Sin[θ[t] + ϕ[t]] m_B r_b θ′[t] (θ′[t] + ϕ′[t]) +
     ℓ Sin[θ[t] + ϕ[t]] m_B r_b (θ′[t]^2 + θ′[t] ϕ′[t]) +
     ℓ Cos[θ[t] + ϕ[t]] m_B r_b θ″[t] + 𝓘_B (θ″[t] + ϕ″[t]) == 𝒯_2[t]};
```

Since the equations are not linear, a nonlinear state space is computed:

In[6]:=
```
satb = NonlinearStateSpaceModel[eqns, {θ[t], θ'[t], ϕ[t], ϕ'[t]},
     {𝒯_1[t], 𝒯_2[t]}, {θ[t], ϕ[t]}, t, SystemsModelLabels →
      {Automatic, {"θ", "ϕ"}, {"θ", "θ'", "ϕ", "ϕ'"}}] /. pars // Simplify;
satb = NonlinearStateSpaceModel[satb, Automatic, Automatic, Automatic, None]
```

Out[7]=

θ	θ	x_1
θ′	x_1	$\left(-0.0666667\,\mathrm{Sin}[\theta+\phi]\,x_1^2 - 0.133333\,\mathrm{Sin}[\theta+\phi]\,x_1 x_2 - 0.0666667\,\mathrm{Sin}[\theta+\phi]\,x_2^2 - 0.0000142222\,\mathcal{T}_1 + 0.0000142222\,\mathcal{T}_2 + 0.000213333\,\mathrm{Cos}[\theta+\phi]\,\mathcal{T}_2\right) / \left(-1.16889 + 1.\,\mathrm{Cos}[\theta+\phi]^2\right)$
ϕ	ϕ	x_2
ϕ′	x_2	$\left((312.5 + 4687.5\,\mathrm{Cos}[\theta+\phi])\left(4687.5\,\mathrm{Sin}[\theta+\phi]\,x_1^2 + 9375.\,\mathrm{Sin}[\theta+\phi]\,x_1 x_2 + 4687.5\,\mathrm{Sin}[\theta+\phi]\,x_2^2 + \mathcal{T}_1\right) + (-82500. - 9375.\,\mathrm{Cos}[\theta+\phi])\,\mathcal{T}_2\right) / \left(-2.56836\times10^7 + 2.19727\times10^7\,\mathrm{Cos}[\theta+\phi]^2\right)$
θ		θ
ϕ		ϕ

A linearized state space around zero:

In[ ]:=
```
StateSpaceModel[eqns, {θ[t], θ'[t], ϕ[t], ϕ'[t]}, {𝒯_1[t], 𝒯_2[t]}, {θ[t], ϕ[t]},
  t, SystemsModelLabels → {{𝒯_1, 𝒯_2}, {"θ", "ϕ"}, {"θ", "θ'", "ϕ", "ϕ'"}}] /. pars
```

Out[ ]=

					$\mathcal{T}_1$	$\mathcal{T}_2$
θ	0	1	0	0	0	0
θ′	0.	0	0.	0	0.0000842105	-0.00134737
ϕ	0	0	0	1	0	0
ϕ′	0.	0	0.	0	-0.00134737	0.0247579
θ	1	0	0	0	0	0
ϕ	0	0	1	0	0	0

The slosh modeled as a decaying sinusoid:

In[8]:= slosh[t_] = $e^{-0.05\,t}$ Sin[t];

In[9]:= Plot[slosh[t], {t, 0, 100}, PlotRange → All]

Out[9]=
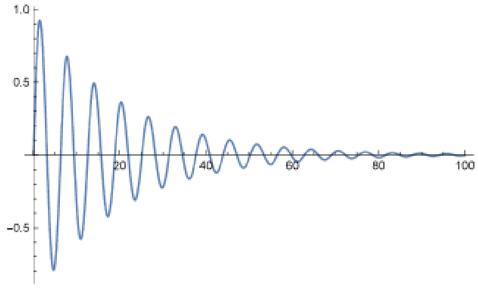

The open-loop simulation reveals an unstable response:

In[116]:=
```
OutputResponse[{satb, {0.1, 0, 0.2, 0}}, {slosh[t], 0, 0, 0}, {t, 0, 100000}];
Plot[#[[1]], {t, 0, 100000}, PlotRange → All, PlotLabel → #[[2]],
   AxesLabel → {"s", "rad"}, ImageSize → Medium] & /@ Thread[{%, {"θ", "ϕ"}}]
```

Out[117]=

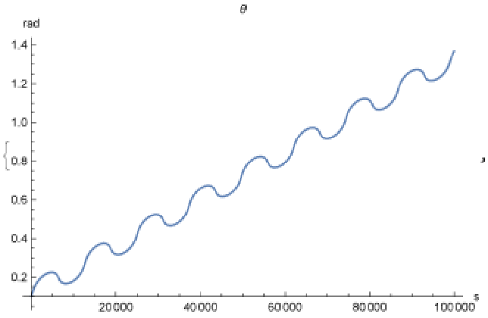

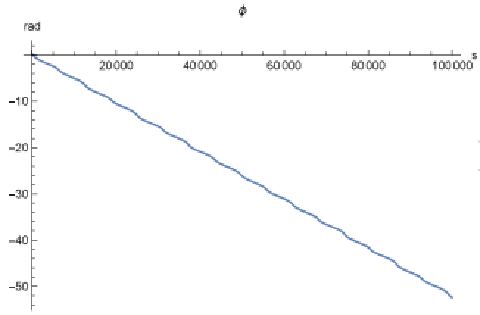

Since the position of the tank is not controlled, we need to specify the feedback input which is also the tracked output state:

```
sspec = <|"InputModel" → satb, "FeedbackInputs" → 2, "TrackedOutputs" → 2|>;
```

The design of an LQR involves the determination of the values for the cost and weighting matrices q & r respectively.

```
{q, r} = {DiagonalMatrix[{10000, 1, 50000, 1, 1}], {{0.001}}};
MatrixForm /@ %
```

The gains of the LQR and the closed-loop system with the optimal controller in the feedback path:

```
{κ, csys} = LQRegulatorGains[sspec, {q, r}, {"FeedbackGains", "ClosedLoopSystem"}];
{κ // MatrixForm, csys}
```

Out[113]= {(-32.0546 3231.54 7074.8 932.611 -31.6212), (state-space object with states θ, x_1, ϕ, x_2, x_3; outputs θ, ϕ) }

For the simulation, let the sun be at 1 radian from the satellite bus's orientation. This means that the reference signal must be set at 1:

```
In[122]:= ref = 1;
```

The output response shows the satellite bus tracks the sun independent from the ball's position:

```
In[123]:= or = OutputResponse[csys, {slosh[t], ref}, {t, 0, 100000}]
```

Out[123]= {InterpolatingFunction[Domain: {{0., 1.00 × 10^5}} Output: scalar][t],

InterpolatingFunction[Domain: {{0., 1.00 × 10^5}} Output: scalar][t]}

In[124]:=
```
Plot[#[[1]], {t, 0, 2000}, PlotRange → All, PlotLabel → #[[2]],
  AxesLabel → {"s", "rad"}, ImageSize → Medium] & /@ Thread[{or, {"θ", "ϕ"}}]
```

Out[124]=

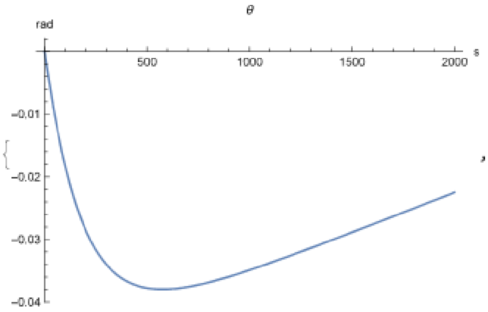

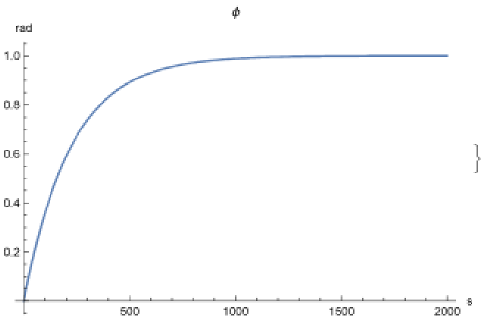

5. Conclusions & Further Research

The motivation of this project was to assess the viability of a modular, articulated satellite design for the role of a fuel depot in space considering the requirements of future space missions which will necessitate the development of a relay-based infrastructure not only for communications but for fuel supply. The main challenge of storing fuel in space are the severe temperature variations which, particularly in the case of cryogenic fuels is presents a considerable challenge along with multiphase flow [18]. Another engineering challenge that can be added to the slew of engineering and logistical challenges involved in the development of an orbital fuel depot is the low-g slosh and high-amplitude slosh. As shown, a conventional control system may be insufficient for controlling a system with slosh dynamics.

A theoretical framework was laid out for the spacecraft dynamics which involved describing different coordinate systems as well as the subsystems involved in determining, computing and applying attitude control on a modern spacecraft as well as the process to design and implement an attitude control system taking into account the different drivers for the system architecture in order to justify the design and simulation of the proposed system, the ballbot-inspired orbital fuel depot satellite. It has been demonstrated that the presented satellite's design is capable of carrying out its mission a single rigid lumped body using a combination of a PD controller and a notch filter as well as a flexibly coupled ball-and-bus structure combination which requires a smaller control effort and has higher precision with the added benefit of not exciting unstable slosh modes.

As stated, one of the key motivations has not only been to present the satellite but also provide a basis for developing its design more rigorously as well as obtaining a better understanding of fluid slosh and mechanically coupled structures in space. The following directions in which further research based on this project can take place:

- A more sophisticated fluid slosh model, the actual model used has been a simplified model using two pendulums. More slosh modes, or a finite element computational simulation could be implemented to obtain a more accurate simulation of the satellite's behavior in space.
- The fuel considered for this research was not cryogenic, however, cryogenic fuels are one of the main fuels considered for interplanetary travel due to the potential to extract them in-situ.
- Low-g sloshing was not considered. However, low-g sloshing could be pivotal in determining the viability of the design and the architecture of the satellite's ACS.
- The coupling mechanism was not conceived or developed in this project, it can be developed and tested in further research which would involve not only the mechanical interface but the electronics and sensor suite.
- Further assessment of the design geometry is required to meet power and thermal constraints for a satellite LEO orbit. A different geometry might be

considered for a satellite placed in a different orbit such as a Lunar orbit or a Lagrange Point.

6. Bibliography

[1] J. Dewar, "To the End of The Solar System: The Story Of The Nuclear Rocket, Apogee, 2003.

[2] United Launch Alliance, «Successful Flight Demonstration Conducted by the Air Force and United Launch Alliance Will Enhance Space Transportation,» The Wayback Machine, 2009.

[3] B. Kutter, «Propellant Depots Made Simple,» 2011.

[4] D. R. Adamo, «Potential Propellant Depot Locations Supporting Beyond-LEO Human Exploration,» 2012.

[5] D. Beinhoff, «Top 10 Technologies for Reusable Cislunar Transportation,» 2011.

[6] C. Bergin, «NASA interest in an interplanetary highway supported by Propellant Depots,» 2011.

[7] F. Zegler i K. Bernard, «Evolving to a Depot-Based Space Transportation Architecture,» de *American Institute of Aeronautics and Astronautics SPACE*, 2010.

[8] F. J. Morring, «NASA to Study Cryo Storage in Space,» *Aviation Week,* 2011.

[9] J. Foust, 16 4 2021. [En línia]. Available: https://spacenews.com/nasa-selects-spacex-to-develop-crewed-lunar-lander/.

[10] StrategyPage, «StrategyPage,» 6 6 2016. [En línia]. Available: https://strategypage.com/htmw/htspace/20160706.aspx.

[11] S. R. Starin, «Attitude Determination and Control Systems,» 2011.

[12] Jena-Optronik GmbH, «Astro APS,» Jena-Optronik GmbH, [En línia]. Available: https://satsearch.co/products/jena-optronik-astro-aps. [Últim accés: 6 2022].

[13] AAC Clyde Space, «MAG-3 Satellite Magnetometer,» AAC Clyde Space, [En línia]. Available: https://satsearch.co/products/aac-clyde-mag-3-satellite-magnetometer. [Últim accés: 6 2022].

[14] T. Rogoway, «This Rare Photo Shows The Most Sensitive Part Of A Combat Aircraft,» Jalopnic, 28 8 2014. [En línia]. Available: https://jalopnik.com/this-rare-photo-shows-the-most-sensitive-part-of-a-comb-1627339307. [Últim accés: 3 6 2022].

[15] M. Reyhanoglu, «Modeling and Control of Space Vehicles with Fuel Slosh Dynamics,» 2011.

[16] Y. Yang, Spacecraft Modeling, Attitude Determination and Control, CRC Press, 2021.

[17] M. J. Sidi, Spacecraft Dynamics and Control A Practical Engineering Approach, New York: Cambridge University Press, 1997.

[18] C. B. Muratov, «Issues of Long-Term Cryogenic Propellant Storage in Microgravity,» NASA, Moffett Field, 2011.

[19] S. Cho i N. H. McClamroch, «Dynamics of Multibody Vehicles and Their Formulation as Nonlinear Control Systems,» de *Proceedings of America Control Conference*, 2000.

[20] N. Coulter, «Design of an Attitude Control System for a Spacecraft with Propellant Slosh Dynamics,» Embry-Riddle Aeronautical University Scholarly Commons, Daytona Beach, 2018.

[21] Reyhanoglu i Hervas, «Nonlinear Control of Space Vehicles With Multi-Mass Fuel Slosh Dynamics,» *IEEE,* pp. 248-252, 2011.

[22] B. Vaidya, M. Shomin, R. Hollis i G. Kantor, «Operation of the Ballbot on Slopes and with Center-of-Mass Offsets,» 2015.

[23] P. A. Savella, «Maneuvering Control of a Spacecraft with Propellant Sloshing,» 2011.

[24] C. Mcnally, D. Miller, T. Nielsen, I. Olson, H. Shelar, R. Shu, J. Weiss i S. Wetherhold, «Commercial Heavy-lift Orbital Refueling Depot CHORD Aerosp 483 Space Systems Design Final Report,» 2013.

[25] . Institute of Electrical and Electronics Engineers, Proceedings of 2018 International Conference on Information Systems and Computer Aided Education : ICISCAE 2018 : July 6-8, 2018, Changchun, China.

[26] R. Institute of Control i . Institute of Electrical and Electronics Engineers, ICCAS 2018 : 2018 18th International Conference on Control, Automation and Systems : proceedings : October 17 (Wed)-20 (Sat), 2018, YongPyong Resort, PyeongChang, Korea..

[27] J. R. Clark, J. M. Horack, M. Zhuang i M. Kumar, «On-Orbit Cryogenic Refueling: Potential Mission Benefits, Associated Orbital Mechanics, and Fuel Transfer Thermodynamic Modeling Efforts».

[28] S. bhushan Sankhyan, «Design, Mathematical modeling of a Ball Balancing Robot,» 2015.

[32] J. R. Wertz, Spacecraft Alltitude Determination and Control, Astrophysics and Science Library, 1978.

[33] C. Richter, B. Teichert i K. Pavelka, «Astronomical Investigation to Verify the Calendar Theory of the Nasca Lines,» 2 2021. [En línia]. Available: https://www.mdpi.com/2076-3417/11/4/1637/htm.

[34] L. Brits, Artist, *Euler angles.* [Art].

[35] F. A. Administration, Artist, *Earth Centered Inertial Coordinate System.* [Art]. Federal Aviation Administration.

[36] P. Tslotras, H. Shen i C. Hall, «Satellite Attitude Control and Power Tracking with Energy Momentum / Momentum Wheels,» *Journal of Guidance Control and Dynamics,* 2001.

[37] NASA, «Reaction/Momentum Wheel,» 1997. [En línia]. Available: https://spinoff.nasa.gov/spinoff1997/t3.html. [Últim accés: June 2022].

[38] Hur-Diaz, S. Wirzburger i J. Smith, «Three Axis Control of the Hubble Space Telescope Using Two Reaction Wheels and Magnetic Torquer Bars for Science Observations,» de *Markley Astronautics Symposium*, Cambridge, MD, 2008.

[39] P. Fortescue, G. Swinerd i J. Stark, Spacecraft Systems Engineering, Wiley, 2011.

[40] Solar MEMS Technology , «Space Equipment Products,» Solar Mems Technology S.L, 2017. [En línia]. Available: http://www.solar-mems.com/space-equipment/.

[41] L. D. Peterson, E. F. Crowley i R. J. Hansman, «Nonlinear Fluid Slosh Coupled to the Dynamics of Spacecraft,» *American Institute for Aeronautics and Astronautics,* vol. 27, núm. 9, 2012.

[42] K. Schlee i A. Corporation, «Modeling Spacecraft Fuel Slosh at Embry-Riddle Aeronautical University,» Mathworks Inc., 2007. [En línia]. Available: https://www.mathworks.com/company/newsletters/articles/modeling-spacecraft-fuel-slosh-at-embry-riddle-aeronautical-university.html. [Últim accés: 6 2022].

[43] P. Fankhauser i C. Gwerder, «Modeling and Control of a Ballbot,» ETH Zurich, Zurich, 2010.